UiT
THE ARCTIC
UNIVERSITY
OF NORWAY

Faculty of Science and Technology
Department of Physics and Technology

Analysis of Oil Spill and Sea Ice Measurements Using Full-Polarimetric and Hybrid-Polarity Synthetic Aperture Radar data

—

Martine M. Espeseth
A dissertation of the degree of Philosophiae Doctor – September 2019

"Physics isn't the most important thing. Love is." — Richard P. Feynman

Abstract

Synthetic Aperture Radar (SAR) data has been used for decades to detect oil slicks and monitoring sea ice. With increased oil and gas exploration in the Arctic follows higher risk for oil spills. Knowledge of the sea ice and oil spills is important for making clever and efficient decisions in a hectic and also non-hectic operational situation, e.g., oil recovery operations or during nautical navigation procedures. The first aim of this thesis is to understand the potential and limitations of multipolarization SAR data for detecting and characterizing marine oil spills. The second aim of this thesis involves investigating the use of real and simulated hybrid-polarity (HP) SAR data for separating different types of sea ice. The analyses are performed on unique data sets acquired during oil spill exercises in the North Sea and on sea ice in-situ data collected in Fram Strait. The potential and limitations of HP mode for oil spill and sea ice applications are evaluated, and results show that the HP mode is almost as good as the full-polarimetric (FP) SAR mode. This thesis also recommends FP and HP features suitable for oil slick detection. These are identified to have a strong connection to oil damping of the small-scale ocean surface roughness in two-scale Bragg models. Separability of various Arctic sea ice is evaluated, and results based on both real- and simulated HP data are compared. Overall, the results indicate a similar separability performance using real- and simulated HP data. The backscattered signal from oil slicks might be contaminated by various system noise sources, especially for spaceborne instruments. This will limit the ability to use the data for any scattering analysis or information extraction of physical oil properties. A set of well known polarimetric features are shown to be highly influenced by system noise, both additive and multiplicative. It is demonstrated that including several multiplicative system noise factors reduces the signal-to-noise ratio. The reasons for what has often been assumed a different scattering mechanism within oil slicks, frequently termed non-Bragg in the literature, is concluded to mainly be result of system noise. This thesis also explores methods that provide complementary information products that could be valuable in the oil spill recovery process. The methodologies are aimed at creating maps that combine several SAR images to make products that quantify and visually depict the temporal evolution of the slick in an easily understandable representation. The work presented in this thesis adds to the on-going discussion on the use of multipolarization and HP data for oil spill detection/characterization and sea ice monitoring, including the effect of varying sensor parameters, with a special focus on additive and multiplicative system noise sources.

Acknowledgements

Contents

List of Figures

List of Tables

List of Abbreviations

BAQ Block Adaptive Quantization

CIRFA Centre for Integrated Remote Sensing and Forecasting for Arctic Operations

CP Compact-Polarimetry

DCP Dual-Circular Polarization

DLR German Aerospace Center

DP Dual-polarimetric

ESA European Space Agency

EM Electromagnetic

FP Full-Polarimetric

HP Hybrid-Polarity

IR Infrared

ISLR Integrated Sidelobe Ratio

JM Jeffries-Matusita

JPL Jet Propulsion Laboratory

KS Kolmogorov–Smirnov

KSAT Kongsberg Satellite Services

MNR Multiplicative-Noise-Ratio

NASA National Aeronautics and Space Administration

NESZ Noise-Equivalent-Sigma-Zero

NOFO Norwegian Clean Seas Association for Operating Companies

PRF Pulse Repetition Frequency

PSLR Peak-to-Sidelobe Ratio

QP Quad-Polarimetric

RAR Real Aperture Radar

RCM Radarsat Constellation Mission

RCS Radar Cross-Section

SAR Synthetic Aperture Radar

SFI Centre for Research-based Innovation

SLAR Side-Looking Airborne Radar

SNR Signal-to-Noise Ratio

SP Single-Polarimetric

SPM Small Perturbation Model

UAVSAR Uninhabited Aerial Vehicle Synthetic Aperture Radar

WMS Web Map Service

Nomenclature

B_r Bandwidth of transmitted pulse

C Covariance matrix

c Speed of light

D_A Antenna length

D_R Antenna width

DR Damping ratio

DoP Degree of Polarization

d Bhattacharyya distance

d_R Difference between ranked pairs

E^{sc} Scattered electric field vector

E^{tr} Transmitted electric field vector

$F_X(x)$ Cumulative distribution function

f Frequency

$f(x)$ Probability density function

H   Horizontal polarization

h Height between sensor and surface

k Wavenumber

$\boldsymbol{k}_{HP}$ Target vector for a hybrid-polarity system

$\boldsymbol{k}_{GH,GV}$ Target vector for general transmit and linear receive

k_s Calibration and processing scaling factor

L Synthetic aperture length

$\boldsymbol{M}$ Measured Sinclair matrix

$\boldsymbol{m}$ Mean of a class

$\boldsymbol{N}$ Complex additive noise matrix

n_{pq} Complex additive noise coefficient at p and q polarizations

$\boldsymbol{q}$ Stokes vector

R_{pq} Bragg scattering coefficients at p and q polarizations

$\boldsymbol{R}_s$ Cross-talk and channel imbalance in the receiving system

$\boldsymbol{S}$ Sinclair matrix

s_h Standard deviation of the surface height

$\boldsymbol{s}_L$ Target vector in lexicographic basis

$\boldsymbol{s}_P$ Target vector in Pauli basis

$\boldsymbol{T}$ Coherency matrix

$\boldsymbol{T}_s$ Cross-talk and channel imbalance in the transmitting system

V	Vertical polarization
W	Wave number spectral density of the surface roughness
χ	Ellipticity angle
δ_A	Azimuth resolution
δ_{CI}	Channel imbalance
δ_p	Penetration depth
δ_{R_g}	Ground range resolution
δ_1/δ_2	Cross-talk values
ϵ_r	Relative dielectric constant
λ	Wavelength
λ_B	Wavelength of Bragg waves
ψ_{ti}	Tilt angle: angle between the normal to the surface and the normal of a facet in the plane of incidence
ψ	Orientation angle
ϕ	Rotation angle of tilted facet
ρ_S	Spearman's correlation coefficient
Σ	Covariance of two classes
σ_{pq}^n	Additive noise power at p and q polarizations
σ_{pq}^0	Radar backscatter coefficient at p and q polarizations
θ	Incidence angle
θ_i	Local incidence angle
ζ_{ti}	Tilt angle: angle between the normal to the surface and the normal of a facet in the plane perpendicular to the plane of incidence

/1

Introduction

This thesis explores the potential of using Synthetic Aperture Radar (SAR) polarimetry for observing oil spills and sea ice. The upcoming sections outline the objectives and motivation of the studies presented in the thesis.

1.1 Motivation

The work presented in this thesis is funded by a Centre for Research-based Innovation (SFI), the Centre for Integrated Remote Sensing and Forecasting for Arctic Operations (CIRFA). The focus of CIRFA is integrating remote sensing and forecasting, understood as the process of combining remote sensing data from various sensors, in-situ information and numerical models, for predictions of oceans and sea ice. Since the Arctic is remote, often cloud-covered, and dark for several months of the year, remote sensing instruments are key tools for extracting information from these areas. There are currently several satellites that can be used, and the large amount of available data has created a need for new and efficient methods capable of extracting useful information. CIRFA focuses on the remote sensing of sea ice, oil spills, and the ocean itself. Due to commercial interests, both shipping vessels and petroleum rigs have an increasing presence in the Arctic, and remote sensing instruments are a valuable resource capable of improving operations and monitoring for potential environmental damage. For example, oil spills at sea have been a serious problem for a long time and can cause great harm to the environment. Both active and passive remote sensing systems have proven useful for detecting and also characterizing oil spills. It is well known that SAR can detect oil spills, but recent studies have investigated

the possibility of characterizing the oil in terms of its composition (oil type), thickness, and/or the oil fraction in the oil/water mixture. In-situ measurements are necessary to understand and develop algorithms from remote sensing data. Therefore, participation in various field campaigns and experiments in collaboration with other institutes like the Norwegian Polar Institute, Norwegian Clean Seas Association for Operating Companies (NOFO), Jet Propulsion Laboratory (JPL), and German Aerospace Center (DLR) has been a priority. The work presented in this thesis focuses on remote sensing using SAR.

Operational sea ice and oil spill services use SAR as their main source when producing sea ice maps, oil spill detection reports, and other products. Operationally, the single-polarimetric (SP) and the conventional dual-polarimetric (DP) modes are used due to their large spatial coverage. The conventional DP mode is referred to as having one co- and one cross-polarization channel. However, these conventional polarization modes do not offer the high polarimetric information of a quad-polarimetric (QP) (also known as the full-polarimetric (FP)) system. In the last decade researchers have demonstrated that QP modes can yield better separation of different sea ice types compared to the conventional SP and DP modes. The potential of QP modes for distinguishing various types of oils has also been studied, but this must yet be proven for various oil types under different environmental conditions. Low backscattering targets, such as oil slicks and some sea ice types, can be dominated by system noise in remote sensing data. Much research has ignored the large impact of system noise on the measured signal from these low backscattering areas. Ignoring system noise can lead to misinterpretation and miscalculation of scattering properties and information extracted from these targets. More research on separating system noise from the backscattered signal could therefore be beneficial.

Large spatial coverage, fine resolution, high polarimetric information, and minimal radar noise are "dream" properties of an imaging mode. Unfortunately, there will always be a trade-off between these properties. The hybrid-polarity (HP) SAR mode was introduced to improve this trade-off, and has the following advantages: (1) the doubling of the swath width compared to the QP SAR mode; (2) higher polarimetric information than the conventional DP SAR mode; (3) two polarization channels with better signal-to-noise ratios than cross-polarization channels for ocean applications [Raney, 2007]. The HP SAR transmits a circular polarized wave and receives in linear horizontal and vertical polarization channels. The HP mode lies within the group of compact-polarimetry [Souyris et al., 2005]. Currently, the Radarsat Constellation Mission (RCM) (launched June 12, 2019) and ALOS-2 (launched 2014) carries the HP SAR mode. RISAT-1 also offered the HP SAR mode, but this instrument is no longer active. Several research communities have investigated the potential of the HP mode within the fields of sea ice, oil spill detection and classification, crop monitoring, etc., and the majority have concluded that the HP mode is almost "as good" as QP SAR [Atteia and Collins, 2013, Souyris et al., 2005, Li and Perrie, 2016, Collins et al., 2013, Espeseth et al., 2017, Panigraphi and Mishra, 2012]. Most of the published research around the HP mode do not have real HP SAR data available, and thus have to simulate the HP from FP SAR data. It still remains to be tested whether real HP data is as "good" as the FP data.

Several core topics are explored in this thesis. Figure 1.1 shows which topics are covered by each paper (Papers I-IV). The four papers are:

Paper I: M. M. Espeseth, S. Skrunes, C. E. Jones, C. Brekke, B. Holt, and A. P. Doulgeris. "**Analysis of Evolving Oil Spills in Full-Polarimetric and Hybrid-Polarity SAR**", IEEE Transactions on Geoscience and Remote Sensing, vol. 55, no. 7, pp. 4190-4210, July 2017.

Paper II: M. M. Espeseth, C. Brekke, C. E. Jones, B. Holt, and A. Freeman "**Interpreting backscattering from oil spills in view of system noise in polarimetric SAR imagery**", IEEE Transactions on Geoscience and Remote Sensing, 2019, in review.

Paper III: M. M. Espeseth, C. E. Jones, B. Holt, C. Brekke, and S. Skrunes "**Oil Spill Response-Oriented Information Products Derived from a Rapid Repeat Time-Series of SAR Images**", IEEE Journal of Selected Topics in Applied Earth Observations and Remote Sensing, 2019, submitted.

Paper IV: M. M. Espeseth, C. Brekke, and M. Johansson, "**Assessment of RISAT-1 and Radarsat-2 for Sea Ice Observations from a Hybrid-Polarity Perspective**", Remote Sensing. vol. 9, no. 11, September 2017.

Other published papers (as first author or co-author) that are left out of this thesis, but listed in Section 6.2, are indicated in Figure 1.1 by relevance to the core topics. These four papers compose the research contributions of the thesis and the main objectives are:

- To compare the usefulness of various multipolarization SAR features from a FP and HP perspective in relation to oil spill detection, and identify the most important SAR features (FP and HP) when detecting oil spills in high wind conditions (Paper I).

- To evaluate the impact of system noise on polarimetric SAR measurements for oil spill observations, including both additive and multiplicative noise (Paper II).

- To propose algorithms that produce oil spill response-oriented information products derived from time series of SAR images from an operational perspective (Paper III).

- To identify the potential of HP for separating various types of Arctic sea ice and to demonstrate a technique for comparing simulated and real HP SAR data (Paper IV).

1.2   Thesis Outline

This thesis is structured as follows. Chapter 2 covers the basic theory of SAR and polarimetry. Chapter 3 provides an introduction to SAR remote sensing of oil spills, and Chapter 4 discusses SAR remote sensing of sea ice mostly from a HP perspective. Chapter 5 describes the SAR data gathered from the different exercises and campaigns. The paper summaries and other work are presented in Chapter 6. Papers I-IV are presented in Chapters 7-10. An innovation project embedded the PhD project, which is a collaborative effort between CIRFA and Kongsberg Satellite Services (KSAT), is presented in Chapter 11. Finally, Chapter 12 concludes this thesis and presents a future outlook.
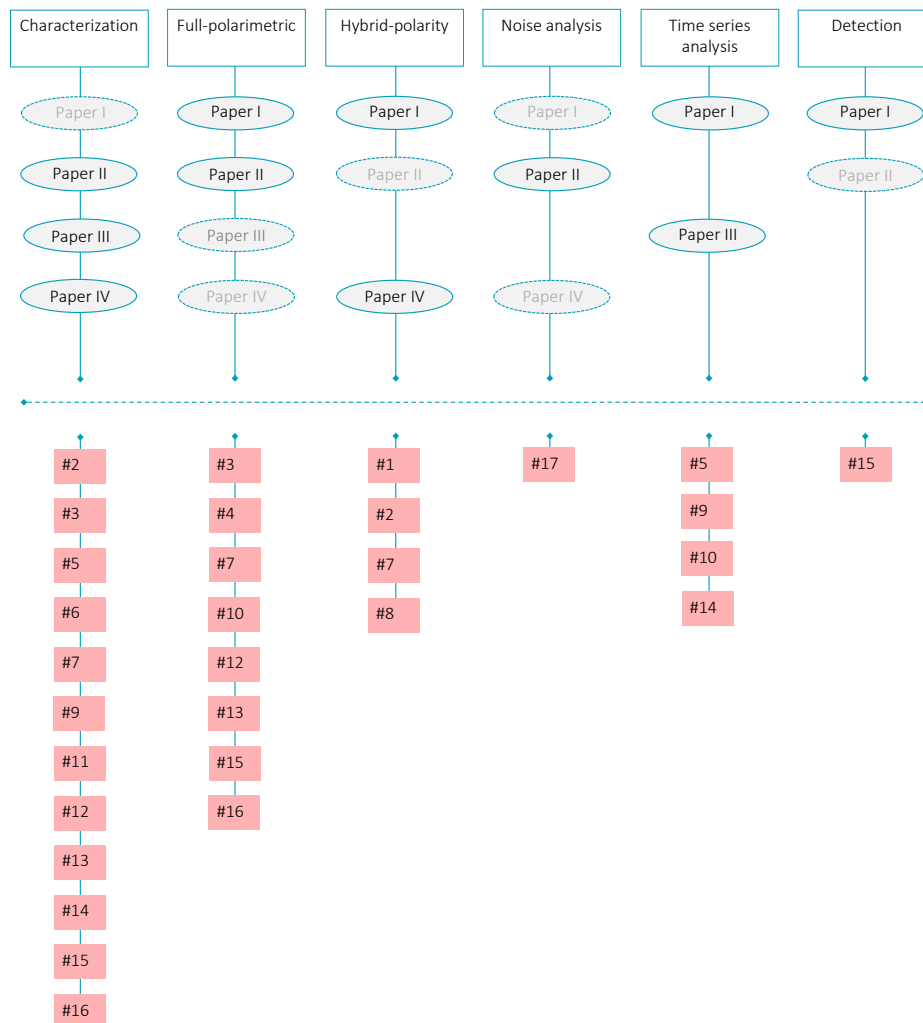
Figure 1.1: Overview of the four papers presented in this thesis (ellipses), in addition to other publications (squares) listed in Section 6.2. Each paper is connected to relevant key-words. The transparent ellipses indicate a weak connection to the key-word.

/2

Remote Sensing by SAR

The groundwork and development of radar instruments started during World War II [Jensen, 2000]. Real Aperture Radar (RAR) and SAR instruments were developed from the 1950s, and the first public domain orbital SAR was provided in late 1970s by National Aeronautics and Space Administration (NASA). Since then, multiple satellites with SAR capabilities have been launched, for example SEASAT (1978), Radarsat-1 (1995) [Jensen, 2000], Radarsat-2 (2007) [Canadian Space Agency, nd], and TerraSAR-X (2007) [Fritz and Eineder, 2010]. During the last decades, the introduction of polarimetry and different imaging modes in spaceborne SAR has improved monitoring and forecasting capabilities that can be of aid in environmental crises, and also benefit industrial operators and governments. Science communities have explored SAR polarimetry and its wide potential in many different applications using methods spanning the field of machine learning to physical modelling.

SAR systems are *active*; the radars provide their own signal to measure the surface backscatter, which enables monitoring both day and night. SAR systems transmit pulses in the microwave region, which is beneficial since these wavelengths penetrate most cloud and weather conditions. This is especially suitable in the Arctic, which is covered in darkness several months of the year and also known for heavy cloud cover.

The upcoming sections describe the SAR geometry, spatial and temporal resolution, and frequency. Additionally, speckle and noise artifacts, surface characteristics, and scattering mechanisms relevant for SAR remote sensing are also discussed as these topics are necessary background for all the papers.

2.1   SAR Geometry

Figure 2.1 shows the geometry of a side-looking radar, such as RAR or SAR. The SAR system is mounted on a platform (aircraft or satellite) and records the backscattered signal, both in *range* and *azimuth* direction (see Figure 2.1), resulting in a two-dimensional image [van Zyl and Kim, 2010]. The two-dimensional image is represented as a matrix where each pixel, i.e., resolution cell, contains unique information about the reflectivity of the scatterers. The reflectivity, also known as the backscatter coefficient, and the radar cross-section (RCS) σ^0, possess unique signatures about the physical composition of the scatterers. The measured RCS is also impacted by the sensor properties, such as the frequency, incidence angle, bandwidth, polarization, and system noise.

The sensor travels along the azimuth direction and the side-looking antenna is pointed in the slant range direction while transmitting electromagnetic (EM) pules towards the ground [Curlander and McDonough, 1991]. The coverage of a scene in ground range direction is equal to the swath width. The physical size of the antenna ($D_R \times D_A$) impacts the resolution on the ground.

The principal difference between SAR and RAR is the azimuth compression applied to the recorded backscattered signal in SAR [Curlander and McDonough, 1991]. With this technique in place, one can achieve extremely fine resolution in the azimuth direction compared to RAR systems.

2.2   Spatial Resolution

Spatial resolution is "the minimum distance between two points on the surface that can still be separable" [Elachi and van Zyl, 2006]. The resulting two-dimensional SAR image has one resolution in range direction (ground and slant range resolution) and one in azimuth direction (azimuth resolution). The ground range resolution (δR_g) is expressed as [Curlander and McDonough, 1991]

$$\delta R_g = \frac{c}{2 B_r \sin(\theta)}, \tag{2.1}$$

where c is the speed of light, B_r is the bandwidth of the transmitted pulse, and θ is the incidence angle. Both RAR and SAR use frequency modulated chirp pulses with a large B_r to achieve a fine range resolution [Elachi and van Zyl, 2006]. Further, a matched filter is applied on the recorded backscatter signal to increase the signal-to-noise ratio (SNR) [Curlander and McDonough, 1991].

The azimuth resolution of a RAR system is [Elachi and van Zyl, 2006]

$$\delta A = \frac{h \lambda}{D_A \cos(\theta)}, \tag{2.2}$$
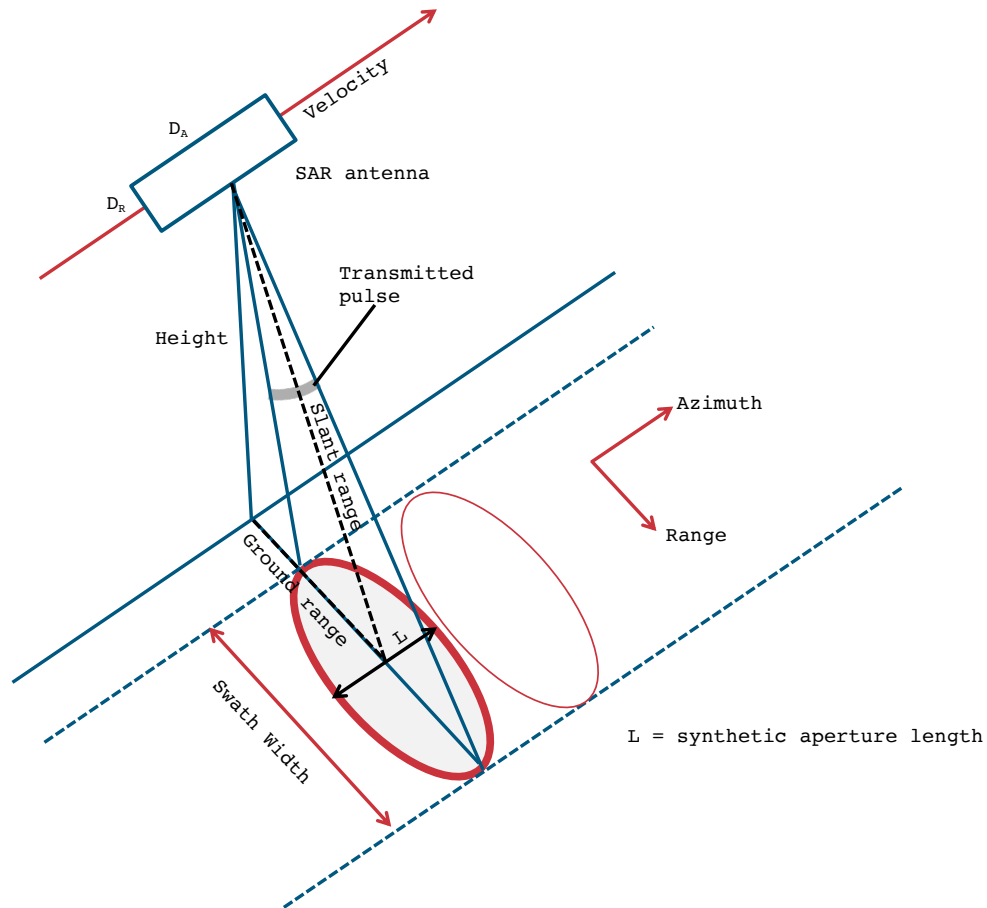
Figure 2.1: Simplified illustration of the SAR geometry (adapted from Figure 1.6 in [Curlander and McDonough, 1991]). D_A and D_R is the antenna length and width, respectively.

where h is the height between the sensor and ground, and λ is the wavelength of the transmitted EM pulse. The azimuth resolution is inversely proportional to the physical antenna length, and a fine azimuth resolution is achieved with a long RAR antenna. The fine azimuth resolution of SAR is achieved as a result of synthesizing a large antenna, hence the name SAR. In order to synthesize a larger antenna, the SAR sensor needs to be in motion while transmitting pulses. After advanced signal processing using the Doppler and phase history of the backscattered pulses the SAR azimuth resolution (δA) is [Curlander and McDonough, 1991]

$$\delta A = \frac{D_A}{2},\tag{2.3}$$

where D_A is the antenna length. As seen from Equation 2.3, a small antenna results in fine resolution. Hence, the SAR is distinctive from other radar systems as it improves the

azimuth resolution by synthesizing a longer antenna.

2.3   Temporal Resolution

The repeat cycle of a satellite is the time it takes for a satellite to pass over the same point on the Earth's surface. The repeat time varies along the latitude, and it can take several days for a spaceborne satellite to revisit the same area with the same orbit. For example, Sentinel-1 and RCM satellites have a repeat cycle of ~12 days, whereas Radarsat-2 has ~24 days [1].

The temporal resolution represents the time it takes for a satellite to cover the same location, i.e., overlap along adjacent orbits in the imaging swaths. The temporal resolution gets finer with distance from the equator. It can take less than one day for a spaceborne satellite to revisit a location in, for example, the Arctic. Combining different satellites will improve the temporal resolution. The same is true if an imaging mode with a large swath width (large coverage) is used. Furthermore, using an airborne instrument, e.g., Uninhabited Aerial Vehicle Synthetic Aperture Radar (UAVSAR) allows for fine temporal resolution. UAVSAR data with a temporal resolution of less than 20 minutes is explored in Papers I, II and III.

2.4   Polarimetry

SAR instruments transmit EM pulses towards the ground, and the EM pulses consist of electric and magnetic fields that are orthogonal to each other. The polarization of the EM wave is defined by the direction of the electric field, and direction and amplitude of the electric field may be described in terms of two orthogonal basis vectors [Elachi and van Zyl, 2006]. In general, the EM waves are elliptically polarized, and special cases are linear and circular polarization [Lee and Pottier, 2009].

Various polarizations and frequencies have different sensitivity to the physical properties of a given surface element, and polarization can therefore provide additional information. In SAR remote sensing, multiple polarization combinations on transmit and receive are available and one given combination is known as a polarization channel. Available polarization channels vary amongst sensors and also within imaging modes of a sensor. In the following subsections, a more detailed description of polarization and polarimetric target descriptors are presented. The concept of compact-polarimetry (CP) – one of the main topics of this thesis – is also introduced.

---

1. `https://earth.esa.int` (accessed 5 September 2019).

2.4.1 Polarization Diversity

SAR instruments can image the surface in different polarimetric modes, referred to as polarization diversity. Note that "mode" also is a common term when referring to the different acquisition modes, like the spotlight, stripmap, and scanSAR modes. There are three main polarimetric modes, namely the QP, DP, and SP mode. The SP mode transmits and receives using a single polarization. The DP mode employs two polarization channels, often one copolarization and one cross-polarization channel. The QP mode both transmits and receives in two polarization channels, resulting in four channels (HH, HV, VH, and VV).

Most satellites have linear polarizations on the transmitter and the receiver, either horizontal and/or vertical. In current satellite missions, there is a compromise between number of polarization channels, swath width, and spatial resolution. Over the last decades, CP has emerged, especially the HP mode [Raney, 2007]. The CP mode employs two channels, and is therefore categorized as a DP system.

There are three modes established in the CP architecture. The first was introduced by [Souyris et al., 2005], known as the $\pi/4$-polarization mode, which transmits diagonally polarized waves (orientated at $45°$) and receives on two linear polarizations. The second mode, the HP mode, was suggested by [Raney, 2007]. In this case, circular polarization is transmitted while receiving linear horizontal and vertical polarizations. The third CP mode transmits in circular and measures the response in left- and right-hand circular polarizations, known as the dual-circular polarization (DCP) mode. In DCP and HP modes, both horizontal and vertical polarizations with different phases are transmitted simultaneously. The reasons for the large interest in the HP mode is that it provides the polarimetric benefits from the QP mode, the large swath width from the conventional co- and cross-polarimetric DP mode, and a simpler implementation of the radar design than the DCP mode [Raney, 2007].

In the literature, the HP mode has received the most attention, and has also been integrated in both previous and current satellites (RISAT-1, ALOS, and the RCM). This mode is explored throughout this thesis and in all the included papers. Papers I and IV are particularly focused on the HP mode.

2.4.2 The Scattering Coefficient

The scattering coefficients holds information about the unique target scattering signatures [Cloude, 2010]. The scattering coefficients are functions of both the sensor properties (frequency, incidence angle, and polarization) and the unique physical signatures of the target. In remote sensing, this unique signature is of special interest. Mathematically, the transformation between the transmitted and the received EM wave is [Lee and Pottier,

2009]

$$E^{sc} = \begin{bmatrix} S_{HH} & S_{HV} \\ S_{VH} & S_{VV} \end{bmatrix} E^{tr} = [S]E^{tr}, \tag{2.4}$$

where E^{tr} is the transmitted electric field vector and E^{sc} is the received electric field vector. $[S]$ is the 2×2 complex scattering matrix that contains the scattering coefficients, where the first (second) subscript represents polarization on transmit (receive). Here, the H and V denotes horizontal and vertical polarizations. For a QP system the full 2×2 scattering matrix can be measured. For the DP system only two of the scattering coefficients are available, while the SP system only allows for one scattering coefficient to be measured. If the complete scattering matrix is known, one can synthesize any arbitrary combination of transmit and receive, for example synthesizing one of the CP modes [Cloude et al., 2012, Cloude, 2010]. This is done in Paper I, Paper II, and Paper IV presented in this thesis, which allows for testing and evaluating the potential of HP modes for applications such as oil spill and sea ice observation.

2.4.3   Covariance and Coherency Matrix

From the full scattering matrix, the target covariance and coherency matrices can be calculated. These matrices have been used frequently in various decomposition methods (for example the H/α decomposition [Lee and Pottier, 2009]) and as input to physical scattering models. Further, these matrices also form the fundamental basis of polarimetric feature retrieval. The full covariance and coherency matrix is derived from FP data. Reciprocity ($S_{HV} = S_{VH}$) is often assumed [Lee and Pottier, 2009], which reduces the covariance and coherency matrices by one dimension. The covariance matrix (C_3) and the coherency matrix (T_3) (with reciprocity) are [Lee and Pottier, 2009]

$$C_3 = \langle s_L s_L^{\star T} \rangle = \begin{bmatrix} \langle |S_{HH}|^2 \rangle & \sqrt{2} \langle S_{HH} S_{HV}^{\star} \rangle & \langle S_{HH} S_{VV}^{\star} \rangle \\ \sqrt{2} \langle S_{HV} S_{HH}^{\star} \rangle & 2 \langle |S_{HV}|^2 \rangle & \sqrt{2} \langle S_{HV} S_{VV}^{\star} \rangle \\ \langle S_{VV} S_{HH}^{\star} \rangle & \sqrt{2} \langle S_{VV} S_{HV}^{\star} \rangle & \langle |S_{VV}|^2 \rangle \end{bmatrix} \tag{2.5}$$

and

$$T_3 = \langle s_P s_P^{\star T} \rangle$$

$$= \frac{1}{2} \begin{bmatrix} \langle |S_{HH} + S_{VV}|^2 \rangle & \langle (S_{HH} + S_{VV})(S_{HH} - S_{VV})^\star \rangle \\ \langle (S_{HH} - S_{VV})(S_{HH} + S_{VV})^\star \rangle & \langle |S_{HH} - S_{VV}|^2 \rangle & \cdots \\ 2\langle S_{HV}(S_{HH} + S_{VV})^\star \rangle & 2\langle S_{HV}(S_{HH} - S_{VV})^\star \rangle \\ & & 2\langle (S_{HH} + S_{VV})S_{HV}^\star \rangle \\ \cdots\cdots\cdots & & 2\langle (S_{HV} - S_{VV})S_{HV}^\star \rangle \\ & & 4\langle |S_{HV}|^2 \rangle \end{bmatrix} \tag{2.6}$$

where $\langle ... \rangle$ denotes spatial averaging, T is the transpose operator, and $\star$ denotes the complex conjugate. The scattering vector in the Lexicographic space, s_L, is defined as [Lee and Pottier, 2009]

$$s_L = [S_{HH}, \sqrt{2}S_{HV}, S_{VV}]^T, \tag{2.7}$$

while s_P is the scattering vector in the Pauli basis, defined as

$$s_P = \frac{1}{\sqrt{2}}[S_{HH} + S_{VV}, S_{HH} - S_{VV}, \sqrt{2}S_{HV}]^T. \tag{2.8}$$

2.4.4 Hybrid-Polarity

Since the late 1980s research communities have synthesized various polarization on transmit and receive from a FP system. Kennaugh and Huynen first presented how to synthesize various polarization on transmit and receive using the unitary change of polarization state transformation [Huynen, 1970, Kennaugh, 1952]. The process of synthesizing various polarization channels is by multiplying the target scattering matrix with unitary matrices that contain information about the ellipticity angle (χ) and the orientation angle (ψ) of the transmitted and received EM wave. Figure 2.2 shows, at a given time-step and at a fixed point in space, an illustration of an elliptically polarized wave. For linear horizontal or vertical polarization the $\chi = 0$, whereas for perfect left- and right-hand circular polarized wave the $\chi = 45°$ and $\chi = -45°$, respectively [Lee and Pottier, 2009].

The HP SAR mode is a subgroup of CP, where the transmitted pulse is either left- or right-hand circular polarized, with linear horizontal and vertical polarizations on receive [Raney, 2007]. Touzi and Charbonneau [2014] pointed out the challenges with generating a perfectly circular polarized wave using current technology. A practical consequence of this is a more elliptically polarized wave rather than circularly polarized in an HP SAR system. This is known as the non-circularity property [Touzi and Charbonneau, 2014]. Paper IV briefly explores the impact of not having a perfect circularly polarized wave when separating different types of sea ice.
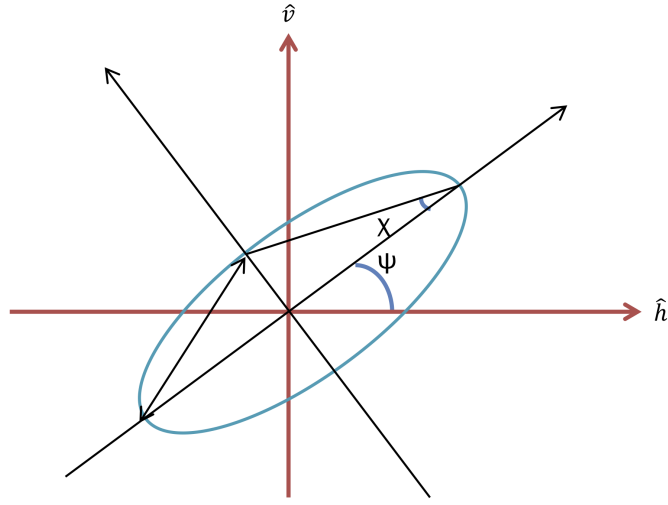
Figure 2.2: Geometry of an elliptical polarized wave described by the orientation angle (ψ) and ellipticity angle (χ). Illustration based on Figure 2.5 in [Lee and Pottier, 2009].

Figure 2.3 gives an overview of the three main CP modes, and three common ways of working with such modes. The three methods, namely reconstruction, feature retrieval, and decomposition, are ways of extracting information about the target. Espeseth et al. [2016] tested two existing reconstruction methods and suggest a new one for sea ice data. This paper is not included as one of the four main papers presented in this thesis. Decomposition has not been the focus of any of the included papers. This is because most of the explored targets usually are dominated by surface scattering, and not double-bounce and volume scattering. Feature retrieval is the method that has received the most attention in the four presented papers.

The Scattering Vector in HP mode

Any polarization can be synthesized on transmit and receive, as long as the full target scattering matrix is available. For example, the DP scattering vector of a general (G) transmit and horizontal (H) and vertical (V) polarizations on receive is defined as [Lee and Pottier, 2009, Sabry and Vachon, 2014];

$$
\boldsymbol{k}_{(GH,GV)} =
\begin{bmatrix}
\cos(\chi_t)\left(\cos(\psi_t)S_{HH} + i\sin(\psi_t)S_{VH}\right) + i\sin(\chi_t)\left(\sin(\psi_t)S_{HH} + i\cos(\psi_t)S_{VH}\right) \\
\cos(\chi_t)\left(\cos(\psi_t)S_{HV} + i\sin(\psi_t)S_{VV}\right) + i\sin(\chi_t)\left(\sin(\psi_t)S_{HV} + i\cos(\psi_t)S_{VV}\right)
\end{bmatrix},
\quad (2.9)
$$

where χ_t and χ_r are the ellipticity angles, and ψ_t and ψ_r are the orientation angles. The superscripts t and r represents transmit and receive. The reason for fixing the receive is because present, current, and future DP SAR missions receive in vertical and horizontal

Compact Polarimetry
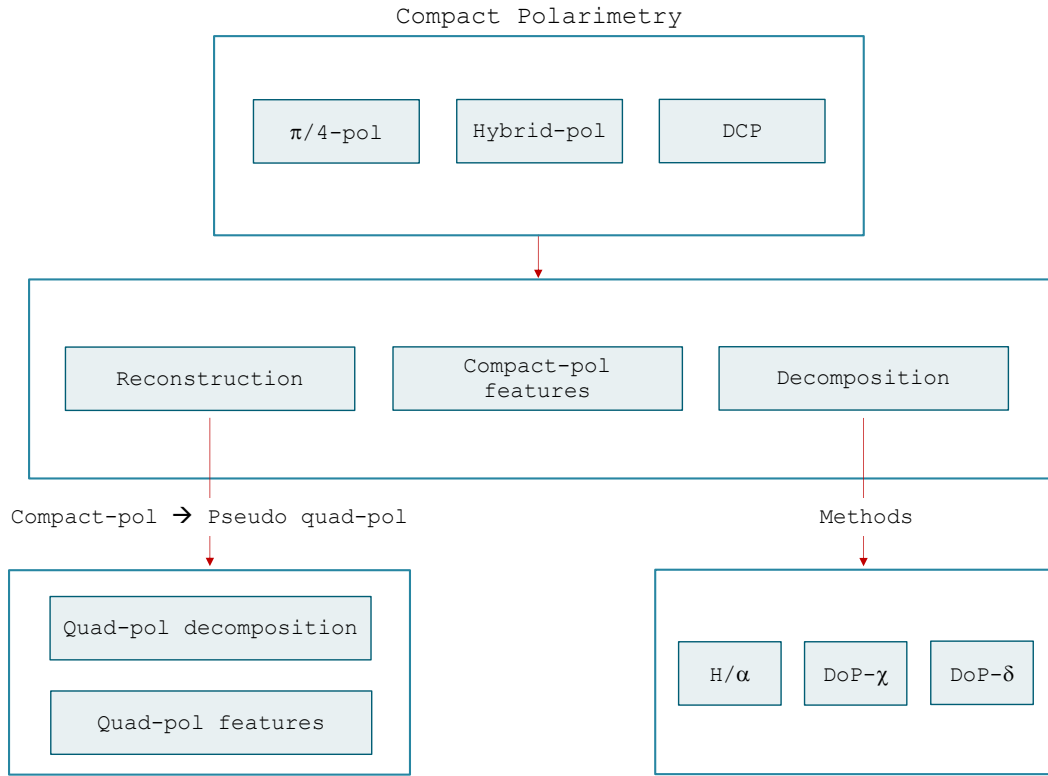
Figure 2.3: Compact polarimetry steps towards reconstruction, feature retrieval, or decomposition.

polarizations, while the transmit varies between vertical, horizontal, and circular. From Equation 2.9 several scattering coefficients can be synthesized, for example the HP mode with right-hand circular transmit and linear horizontal and vertical receive, i.e., $\chi_t = \pm 45$, $\psi_t = 0$, $\chi_r = \psi_t = 0$;

$$\boldsymbol{k}_{HP} = \begin{bmatrix} S_{RH} \\ S_{RV} \end{bmatrix} = \begin{bmatrix} S_{HH} & S_{VH} \\ S_{HV} & S_{VV} \end{bmatrix} \begin{bmatrix} \frac{1}{\sqrt{2}} \\ \pm\frac{j}{\sqrt{2}} \end{bmatrix} = \frac{1}{\sqrt{2}} \begin{bmatrix} S_{HH} \pm jS_{VH} \\ \pm jS_{VV} + S_{HV} \end{bmatrix}. \tag{2.10}$$

Equation 2.10 also demonstrates how the HP mode is simulated from the FP SAR system. This makes it possible to perform a direct comparison between various polarization modes, such as the FP versus HP SAR modes. Such a comparison is performed in most of the presented papers of this thesis. Equation 2.10 also serves as the starting point for feature extraction.

The Stokes Vector

The Stokes vector is a useful tool for representing the data collected by an HP system [Raney, 2007]. The polarization state of a wave can be described through the Stokes

vector [Denbina, 2014]. The four real parameters given in the Stokes vector are incoherent, i.e., have no phase dependency. If the transmitted wave is either left- or right-circularly polarized, the Stokes vector becomes [Raney, 2007]:

$$
\boldsymbol{q}_{LC} = \begin{bmatrix} |E_{RH}|^2 + |E_{RV}|^2 \\ |E_{RH}|^2 - |E_{RV}|^2 \\ 2\Re(E_{RH}E_{RV}^{\star}) \\ 2\Im(E_{RH}E_{RV}^{\star}) \end{bmatrix} \qquad \boldsymbol{q}_{RC} = \begin{bmatrix} |E_{LH}|^2 + |E_{LV}|^2 \\ |E_{LH}|^2 - |E_{LV}|^2 \\ 2\Re(E_{LH}E_{LV}^{\star}) \\ -2\Im(E_{LH}E_{LV}^{\star}) \end{bmatrix}, \tag{2.11}
$$

where E is the complex electric field in the subscripted polarization [Raney, 2007], and L=left-hand circular and R=right-hand circular. Various polarimetric decomposition methods (see lower right box of Figure 2.3) describing scattering mechanisms have been suggested using the Stokes vector [Raney et al., 2012, Cloude et al., 2012]. Several features can be extracted from the Stokes vector, for example the Degree of Polarization (DoP) and ellipticity χ. The DoP has been connected to the entropy describing the scattering degree of randomness [Cloude et al., 2012]. Both DoP and χ have been used frequently in oil spill (see, e.g., [Shirvany et al., 2012, Zhang et al., 2017, Buono et al., 2016b, Nunziata et al., 2015, Nunziata et al., 2013]) and sea ice (see, e.g., [Li and Perrie, 2016, Dabboor and Geldsetzer, 2014b, Zhang et al., 2016, Geldsetzer et al., 2015]) studies. These features are used in three of the papers presented in this thesis.

2.5   Frequency

Frequency plays an important role in the physical interaction between the incident EM wave and the observed surface. The choice of frequency is controlled by the purpose of the SAR mission and its relevant applications. Table 2.1 shows different frequency bands that are commonly used in SAR. In this thesis, frequencies from X-, C-, and L-band have been explored. Ka- and Ku-bands suffer from high interference from the atmosphere due to the short wavelengths in these bands. Hence, these bands are not used frequently for surface studies using spaceborne radar systems.

Frequency band	Ka	Ku	X	C	S	L	P
Frequency [GHz]	40-25	17.6-12	12-7.5	7.5-3.75	3.75-2	2-1	0.5-0.25
Wavelength [cm]	0.75-1.2	1.7-2.5	2.5-4	4-8	8-15	15-30	60-120

Table 2.1: Microwave frequency bands [Chuvieco and Huete, 2010].

2.6 Speckle

Speckle is an inherent property in SAR and causes a grainy appearance and is a result of constructive and destructive interference between many scatterers within a resolution cell [Lee and Pottier, 2009]. Speckle is a multiplicative noise-like feature that is unavoidable in SAR images. Several advanced filter methods exist (see, e.g., [Lee and Pottier, 2009]) to reduce the speckle, but a simple method is averaging over a neighborhood of pixels in the spatial domain. The reduction of speckle is performed after the formation of the image, and when calculating the coherency or covariance matrix.

Figure 2.4 shows the effect of using a boxcar filter to reduce speckle. The left image in Figure 2.4 is the VV-intensity (σ^0_{VV}) without any speckle reduction, while the right image shows the improved visibility of the oil slicks after applying a boxcar filter with a 9×9 window.

Speckle also complicates image analysis like image segmentation and classification of various surfaces [Lee and Pottier, 2009]. Figure 2.5 shows the segmentation results (using a regular k-means clustering [Theodoridis and Koutroumbas, 2009]) without and with speckle reduction using a boxcar filter. A significant effect can be observed from applying speckle reduction, where most of the oil slick is segmented into one class and the surrounding clean sea is segmented as another.
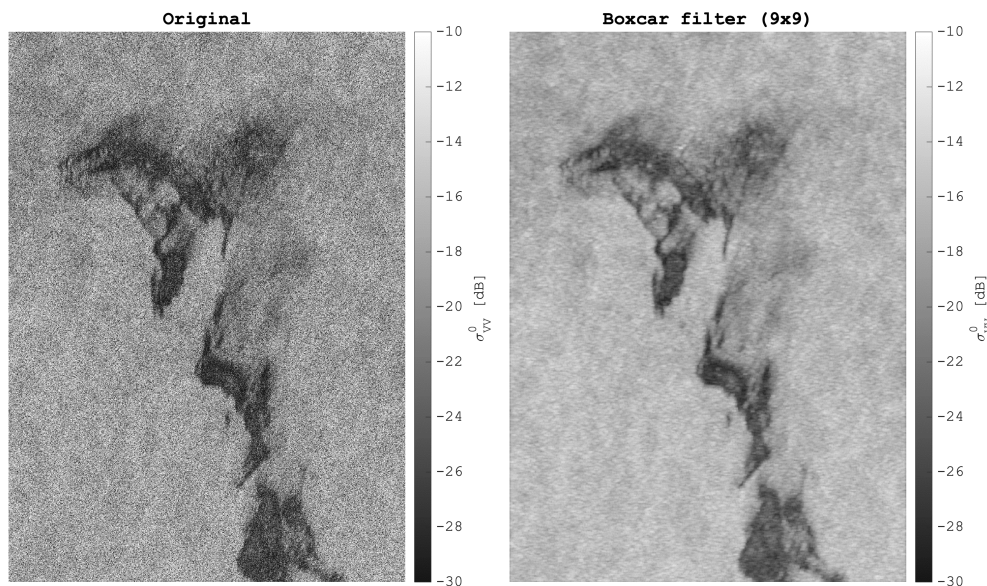
Figure 2.4: σ^0_{VV} images of an oil spill from the oil-on-water exercise in 2012. Left: the original σ^0_{VV} image. Right: σ^0_{VV} with a boxcar filter with a 9×9 window. The Radarsat-2 data and Products © MDA LTD. 2012 - All Rights Reserved.
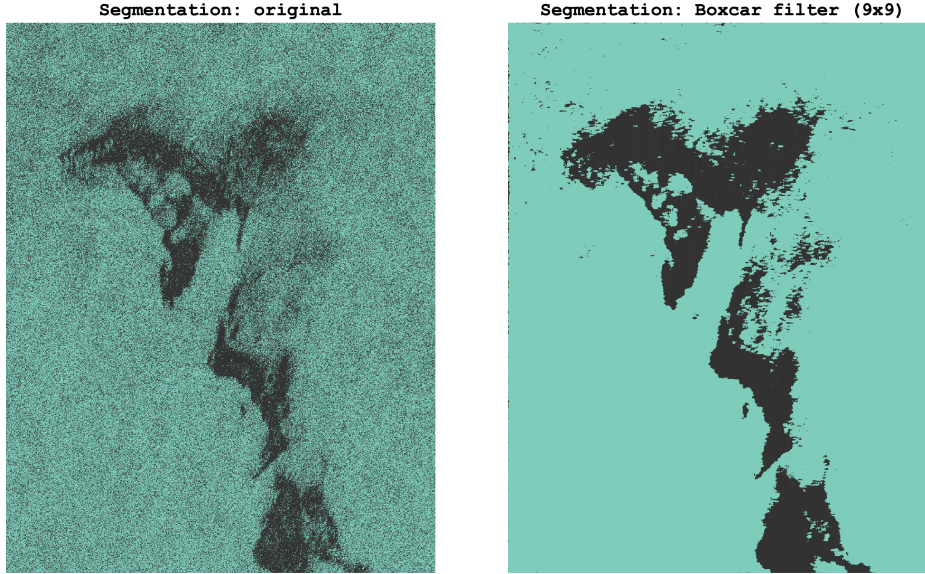
Figure 2.5: Left: Results of segmentation (k-means) on the original VV-intensity image. Right: The effect of speckle reduction (boxcar filter) when segmenting (k-means) the oil slick.

2.7   Noise Artifacts

Polarimetric SAR data contains a great deal of information about the physical interactions between the incident radar wave and the surface elements. Unfortunately, the measured and processed SAR signal contains various types of unwanted noise. As mentioned in Section 2.6, speckle is a multiplicative noise-like feature that is unavoidable in SAR. SAR images suffer not only from speckle noise, but also additive and multiplicative system noise sources. It is not possible to fully recover the RCS, but understanding the effects of various noise types is extremely important to avoid misinterpretations. Noise in SAR data might lead to degraded performance and accuracy of the intended application. The impact of both additive- and multiplicative instrumental noise is studied in Paper II for low-backscattering targets like oil slicks. The upcoming sections provide a brief overview of the various types of noise. This theory is necessary background for Paper II.

The measured scattering matrix can be expressed as [van Zyl, 1990]

$$M = R_s{}^T S T_s + N$$
$$= \begin{bmatrix} 1 & \delta_2 \\ \delta_1 & \delta_{CI} \end{bmatrix} \begin{bmatrix} S_{HH} & S_{HV} \\ S_{VH} & S_{VV} \end{bmatrix} \begin{bmatrix} 1 & \delta_1 \\ \delta_2 & \delta_{CI} \end{bmatrix} + \begin{bmatrix} N_{HH} & N_{HV} \\ N_{VH} & N_{VV} \end{bmatrix}, \tag{2.12}$$

where S is the complex scattering matrix of the target, R_s and T_s are effects of the receiving and transmitting system on the scattering matrix, and N is the complex additive (thermal) system noise [van Zyl, 1990]. δ_1 and δ_2 represent cross-talk, whereas δ_{CI} represents the channel imbalance [van Zyl, 1990]. Equation 2.12 only considers cross-talk and thermal

noise, but there are several additional unwanted noise sources in the measured signal that reduces the SNR. Since the backscatter from oil slicks are low these noise sources might have a significant impact on the polarimetric SAR data covering such areas. The range and azimuth ambiguities, effects from sidelobes, and degradation due to quantization when compressing the measured voltage are not considered in Equation 2.12. These noise sources are just as important as the well known additive system noise when investigating the signal quality from an oil covered pixel. The upcoming subsections briefly discuss each of these noise/degradation sources in SAR, which are also used in Paper II.

2.7.1 Cross-talk and Channel Imbalance

Any SAR mode with more than one channel on either receive or transmit is exposed to cross-talk and channel imbalance. Cross-talk represents leakage between the polarization channels, both within the transmitting and receiving channels. Channel imbalance is inconsistency in amplitude and phase between the polarization channels [van Zyl and Kim, 2010]. Cross-talk and channel imbalance are both unavoidable. The response in the cross-polarization channels is much lower than that of the copolarization channels for most targets and certainly for oil slicks and ocean backscatter. Hence, the leakage is more serious for the cross-polarization channels.

There are ways of estimating and adjusting the cross-talk and channel imbalance using the imaging parameters with some assumptions about the scattering medium [van Zyl, 1990, Ainsworth et al., 2006, Quegan, 1994]. Adjusting the cross-talk and channel imbalance might be crucial when, for example, estimating physical parameters from models, interpreting the scattering physics, and synthesizing (simulating) different polarization modes.

Cross-talk calibration can only be performed on FP SAR data, since the full scattering matrix is required [Touzi et al., 2010, Freeman et al., 1992]. Cross-talk calibration is already performed on the FP Radarsat-2 products before being delivered to customers. Estimation of cross-talk values is not done for UAVSAR and TerraSAR-X in this thesis study. This is because the DP (HH-VV) mode is used in TerraSAR-X, and estimation of cross-talk values is not possible. Cross-talk calibration (see, e.g., [van Zyl, 1990, Ainsworth et al., 2006, Quegan, 1994]) relies on assumption about the scattering surface, and might introduce artifacts in the data. For the UAVSAR products, cross-talk calibration is not recommended for ocean applications, as this might introduce artifacts in the data [personal correspondence Cathleen E. Jones (JPL)]. Paper II highlights the unique cross-talk values in each of the investigated sensors.

2.7.2 Aliasing

Another noise artifact is ambiguity due to aliasing both in range and azimuth direction. These ambiguities appear as ghost images in the SAR data. For example, the ghost of ships might occur at an azimuth distance from the ship, and can in some unfortunate cases be located in an oil slick, corrupting the SAR data in that area. Azimuth ambiguities are affected by, e.g., wavelength, pulse repetition frequency (PRF), and azimuth antenna pattern [Cumming and Wong, 2005]. Range and mostly azimuth aliasing reduce the SNR by introducing unwanted signals that are repeated from other targets and mixed with the desired target signal, and is therefore an important factor to consider for low-backscattering areas such as oil slicks. Paper II briefly discusses the impact of aliasing in range and azimuth direction and how these effects can reduce the SNR.

2.7.3 Effects from Sidelobes

The signal around a target might be spatially smeared as a result of sidelobes of the antenna beam pattern. The terms established to measure these effects are the peak-to-sidelobe ratio (PSLR) and integrated sidelobe ratio (ISLR). These provide an indication of the SAR performance in resolving a weak target in the presence of a strong target (e.g., oil versus ships) [Cumming and Wong, 2005]. Most of the backscattered energy is measured in the mainlobe of the antenna beam pattern (see Figure 2.6). Unfortunately, some energy from adjacent areas will be measured in the sidelobes (like clean sea and ships). The energy from the sidelobes is unwanted signals, resulting in a reduction in the SNR.

The PSLR is defined as the ratio between the highest sidelobe value and the peak value of the mainlobe. The ISLR is the ratio between the total power in all the sidelobes and mainlobe [Cumming and Wong, 2005]. The signal is smeared out along and across track if the ratios of the PSLR and ISLR are high. The effects from the sidelobes can be mitigated by avoiding areas around ships. But the clean sea pixels surrounding the oil slick will have a significant effect on the measured signal from the oil slick if the ISLR is high. Hence low PSLR and ISLR values are desired, such that low-backscattering areas (e.g., oil slicks) have minor impacts caused by spillover from adjacent areas, such as clean sea and ships. The ISLR is therefore factored into the multiplicative noise ratio in the estimation of the SNR for Paper II.

2.7.4 Quantization Degradation

The SAR signal is digitized with an analog-to-digital converter followed by a compression technique (for example Block Adaptive Quantization (BAQ)) to improve the data storage and downlink rate [MDA, 2018]. This introduces degradation noise in the end-product. This could result in lower SNR values (see, e.g., [Vespe and Greidanus, 2012]) especially impacting low-backscattering surfaces like oil slicks and sea ice leads. In some sensors,

Azimuth

sidelobes   sidelobes
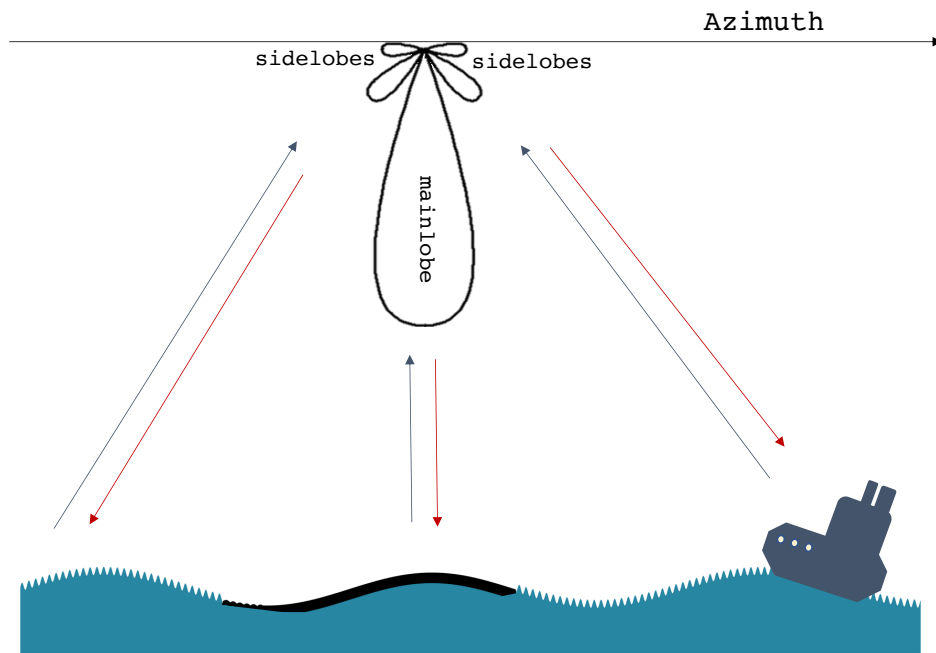
mainlobe

Figure 2.6: Backscattered signal from sidelobes can be captured by the sensor and cause errors in the measured signal from the mainlobe.

the Noise-Equivalent-Sigma-Zero (NESZ) values provided in the product file includes the quantization degradation in the estimation of the nominal NESZ values. One example is the nominal NESZ provided with TerraSAR-X products [Fritz and Eineder, 2010], which includes the quantization noise. On the other hand, Radarsat-2 (see [MDA, 2018]) and UAVSAR products do not include the quantization noise in the nominal NESZ. For example, as pointed out in [MDA, 2018], the quantization noise levels for Radarsat-2 are estimated -19dB times the mean signal level for 4-bit BAQ. This results in larger contributions from the BAQ noise for high values of the mean signal level. The quantization noise is therefore considered in the estimation of the SNR in Paper II.

2.7.5   Additive Noise

The additive noise power is contained in the NESZ, and consists of system and processing noise (e.g., thermal noise and in some cases quantization degradation) that is added to the observed signal from the target. The NESZ is defined as the value for which the radar backscatter coefficient has equal strength to the background noise. NESZ varies as a function of slant range due to the antenna elevation pattern, and also across different sensors and their imaging modes, as demonstrated in Figure 2.7. Examples of some noise
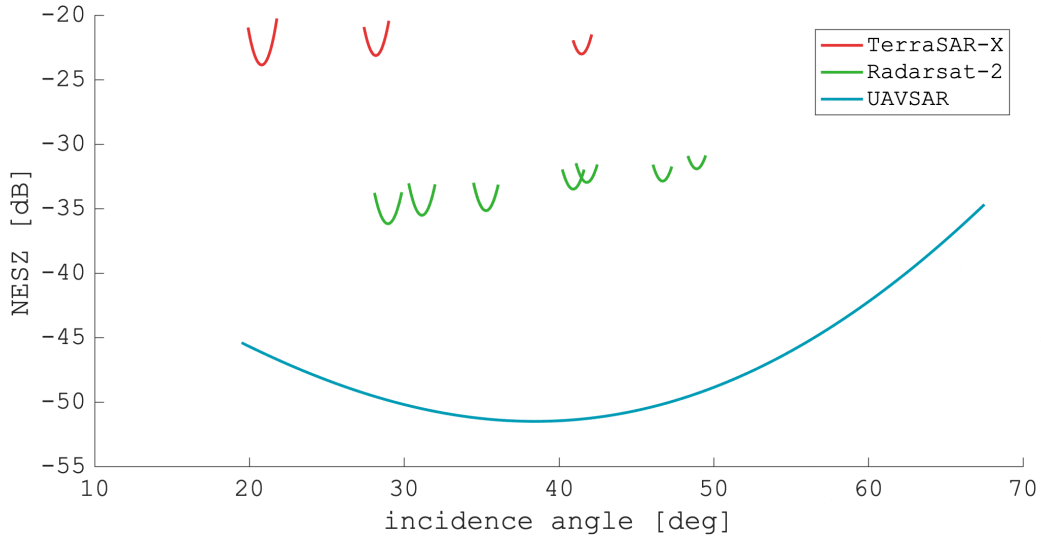
Figure 2.7: NESZ versus incidence angle (θ) for TerraSAR-X (SSC DP (HH-VV) strip-map mode), Radarsat-2 (strip-map fine FP mode), and the UAVSAR (FP mode).

profiles (NESZ) of TerraSAR-X, Radarsat-2, and the UAVSAR are displayed in Figure 2.7. Since the UAVSAR instrument operates in a wide range of incidence angles, only one NESZ profile is shown in Figure 2.7. The NESZ is lowest for the UAVSAR sensor, and this is one of several reasons for this instrument being particularly relevant for oil spill observation.

The SNR is the signal level above the noise floor, and is expressed as;

$$SNR = \frac{\sigma^0}{\sigma^n}, \tag{2.13}$$

where σ^0 is the RCS and σ^n, is the additive noise power. The SNR should be as large as possible. The SNR is often low for spaceborne radar instruments when monitoring low-backscattering targets like oil slicks, grease, or sea ice leads. This is because the smoothness of such surfaces reduces the backscatter response from the incident wave.

2.7.6   Additive and Multiplicative Noise

Most oil spill SAR studies ignore the noise issue or only considers additive noise power using the nominal NESZ when performing a noise analysis, which includes a comparison between the NESZ and the RCS. The impact of ISLR, mostly azimuth aliasing, and quantization noise depends on the mean signal level in the scene. These system noise sources are often left out, but should be included in order to achieve a realistic estimate of the SNR. Since these noise sources depend on the mean signal level in the scene, their effects increase

with the mean signal level. These noise factors are called multiplicative system noise due to their dependency on the mean signal level in the scene, but are in fact another additive noise contribution to the measured signal. The multiplicative-noise-ratio (MNR) is a sum of ISLR, quantization-noise ratio (QNR), and ambiguity ratio (in linear units). Paper II demonstrates the negative impact these noise sources have on the SNR. Paper II suggests the following model (based on [Hensley et al., 2014]) for the measured RCS ($\sigma^{0,m}$)

$$\sigma_{pq}^{0,m} = \sigma_{pq}^0 + \sigma_{pq}^n + \sigma_{pq}^{AVG}MNR, \tag{2.14}$$

and

$$MNR = ISLR + 1/QNR + AMB_t \tag{2.15}$$

where AMB_t is the total ambiguity-to-signal ratio. Since oil slicks are usually surrounded by clean sea, the signals from clean sea areas are repeated (due to aliasing) in the oil-covered areas by a factor equal to $AMB_t \times \sigma_{pq}^{AVG}$ (aliased power). A more accurate representation of the SNR should therefore include both the additive and multiplicative system noise, i.e;

$$SNR_{pq} = \frac{\sigma_{pq}^{0,m} - (\sigma_{pq}^n + \sigma_{pq}^{AVG}MNR)}{\sigma_{pq}^n + \sigma_{pq}^{AVG}MNR}. \tag{2.16}$$

Paper II demonstrates how Equation 2.16 is used and estimated from three different SAR sensors covering oil slicks and clean sea.

2.8 Surface Characteristics

The backscattering signature is highly dependent on the surface characteristics (e.g., roughness and dielectric constant) and sensor properties (e.g., frequency, polarization, incidence angle). The roughness and dielectric constant are discussed in the upcoming sections.

2.8.1 Roughness

High frequency EM waves, i.e., X-band (see Table 2.1), interacts with smaller surface elements than lower frequency waves. Scattering from a rough surface depends strongly on the frequency [Elachi and van Zyl, 2006]. Figure 2.8 shows an example of VV-intensity images from TerraSAR-X (X-band) and UAVSAR (L-band). For a constant roughness spectrum, the RCS increases with the fourth power of the frequency [Elachi and van Zyl, 2006]. The surface roughness and its relation to the incident frequency/wavelength is often described by the Rayleigh criterion, and the surface is considered rough if;

$$s_h \geq \frac{\lambda}{8}\cos(\theta) \tag{2.17}$$

where s_h is the standard deviation of the surface height, λ is the wavelength of the incident wave, and θ is the incidence angle.

The X-band radar observes a rougher sea and more pronounced wave pattern compared to the longer wavelength L-band UAVSAR (see Figure 2.8). The roughness plays an important role when monitoring both oil and sea ice. In oil spill remote sensing, the roughness of the sea is influenced by the wind and ocean conditions, which again will impact the oil-sea contrast. More theory of the roughness in relationship to oil spills and its dampening effects on surface waves is discussed in Chapter 3.
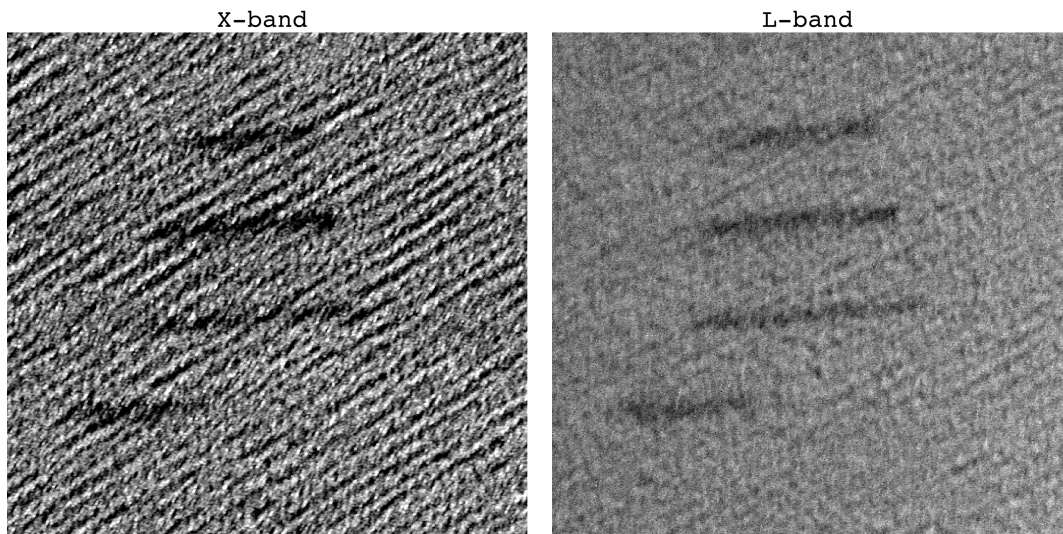
Figure 2.8: VV-intensity of TerraSAR-X (left) and UAVSAR (right) acquired over four oil slicks that were released during the oil-on-water exercise in 2015. TerraSAR-X ©2015 Distribution Airbus DS, Infoterra GmbH. UAVSAR data are courtesy of NASA/JPL-Caltech.

2.8.2 Dielectric Properties

The dielectric constant (ϵ_r) of the surface medium impacts the interaction between the incident EM pulse and the surface. The dielectric properties together with the frequency of the incident wave controls the penetration depth. Lower frequencies penetrate deeper into the surface than higher frequencies. The penetration depth (δ_p) is defined as the depth at which the EM signal is attenuated to $\frac{1}{e}$ [Cloude, 2010], i.e.,

$$\delta_p \approx -\frac{1}{2k\Im(\sqrt{\epsilon_r})} \tag{2.18}$$

where $\mathfrak{I}(\cdot)$ is the imaginary part, ϵ_r is the relative dielectric constant consisting of both a real and imaginary part, and k is the wavenumber defined as

$$k = \frac{2\pi f}{c} \tag{2.19}$$

where f is the frequency of the transmitted EM wave and c is the speed of light. For example, water has a high dielectric constant (both in real and the imaginary parts), and the penetration depth is therefore lower in water compared to pure ice, which has a much lower dielectric constant. Although the dielectric constant of oil is much lower than clean sea (see, e.g., [Minchew et al., 2012, Brekke et al., 2014]), most slicks are too thin for their dielectric properties to significantly influence the backscattered signal.

2.9   Scattering Mechanisms

The scattering mechanism defines how the incident EM wave from the satellite interacts with the target. In general, surface, double-bounce, and volume scattering are the three main scattering mechanisms. Within each category, more complex scattering models can be used that include for example physical interactions within multiple layers (air-snow-ice-water). The measured backscatter signal might be a mixture of one or more scattering types, as a result of several scattering mechanisms occurring within a single resolution cell.

The majority of the papers in this thesis focus on surfaces that are dominated by surface scattering, but some of the papers also discuss volume scattering in context of sea ice or as misinterpreted scattering from oil slicks. As such, only surface and volume scattering is presented in the upcoming sections.

2.9.1   Surface Scattering

Surface scattering, also known as single-bounce scattering, occurs when the incident wave has dispersed only once by the surface boundary between two media (often air and the surface element). There are three main surface scattering scenarios that are controlled by the roughness; (1) smooth surface; (2) slightly rough surface; and (3) a very rough surface [Chuvieco and Huete, 2010] (see Figure 2.9). In the smooth surface scenario, the incident wave is reflected away from the sensor (specular reflection). For a slightly rough surface, the incident wave is divided into two components; specular and diffuse (Lambertian). If the surface is very rough, the backscattered signal is completely diffuse, and a response is generated in all the polarization channels [Cloude, 2010]. No depolarization occurs for a perfectly smooth surface with no out-of-plane tilt [Cloude, 2010], which means no response in the cross-polarization channels. However, if the surface is slightly tilted, a depolarization effect is generated, and a response is introduced in the

cross-polarization channel.
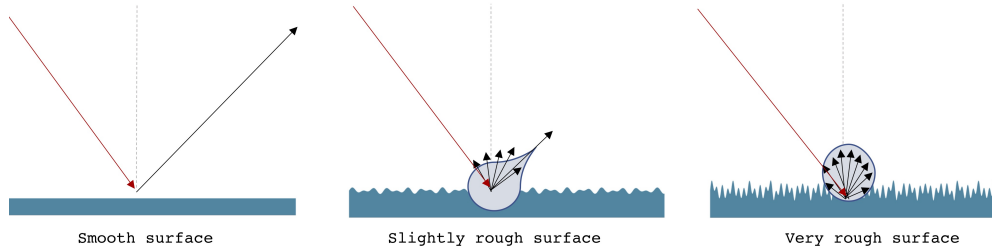
Figure 2.9: Scattering from surfaces with different roughness conditions.

Bragg scattering is a type of surface scattering where the backscatter return from the surface possesses the typical resonant scattering. This occurs when the incident wave's wavelength projected onto the surface is in resonance with the ocean waves [Valenzuela, 1978]. Bragg scattering is an important factor in several of the papers (Papers I-III), and is thus discussed further in Chapter 3. Further, sea ice with various roughness is also investigated (Paper IV), and surface scattering again plays an important role in the set of features that are selected and investigated throughout the papers.

2.9.2   Volume Scattering

Volume scattering occurs within heterogeneous bulk materials with varying particle density and particle distribution that contain local dielectric property variations [Cloude, 2010]. As discussed in Section 2.8.2, frequency, and dielectric properties are two important factors that control the penetration depth. The penetration depth lays the foundation for the dominant scattering type. If the dielectric constant of the scattering element is large, little transmission into the material occurs and thus little or no volume scattering takes place [Tucker III et al., 2013]. However, a higher penetration depth might allow for possible volume scattering to occur within the material, for example multi-year ice [Tucker III et al., 2013]. When volume scattering occurs, a response is generated in all the polarization channels.

There have been several studies within oil spill remote sensing claiming that volume scattering is part of the non-Bragg scattering occurring in oil slicks. One possible origin of volume scattering within the oil slick is breaking waves [Cloude, 2010], which often is classified as the non-polarized component in the non-Bragg scattering group [Alpers et al., 2017]. Unfortunately, system noise has often been misinterpreted as volume scattering measured in the backscattering response from oil slicks. This is the main topic of Paper II, where the influence of various system noise sources in the polarimetric measurements of radar-dark surfaces is explored.

/3

SAR Remote Sensing of Oil Spill

Oil spills in the ocean due to human activities have a major and immediate impact on the marine ecosystem. Oil spills might originate from e.g., a pipeline leakage, illegal and legal discharge from vessels/platforms, or accidents. With approximately 8000 platforms and offshore facilitates in the World's oceans [Coleman, 2003], in addition to shipping, fishing, and tourism, there are many potential sources for oil spills. Another marine pollution is natural seeps from the seafloor, which are the largest source of oil entering the ocean [NOAA, nd].

Oil slicks are detected as dark spots in SAR images due to oil's damping effect on the capillary and small gravity waves. SAR is the main tool for oil spill monitoring, both operationally (see, e.g., [Ferraro et al., 2010]) and also within research (see, e.g., [Skrunes et al., 2014, Brekke et al., 2014, Migliaccio et al., 2009a, Wismann et al., 1998, Solberg et al., 2004]). For example, oil spill detection reports from KSAT are delivered daily to customers around the world. In research, most work has focused on the characterization aspect of the oil, i.e., investigating whether there is any additional information that can be extracted from oil slicks after detection.

The use of optical instruments has been valuable in terms of identifying different oil zones that can be connected to oil thickness according to the Bonn agreement oil appearance code [BAO, 2017]. Additionally, infrared (IR) sensors could potentially detect relative thickness variations within oil slicks [Fingas, 2011]. Unfortunately, one major disadvantage of optical instruments is the need for an external illumination source, like the Sun, and cloud-free view of the target area. SAR is independent of these factors, and therefore an extremely useful tool when monitoring oil slicks. Figure 3.1 demonstrates this and shows

the Landsat-8 panchromatic band and the VV-intensity from the UAVSAR. It is impossible to see the oil in the Landsat-8 image due to clouds, cloud shadows, and/or sun glint conditions. The SAR image, on the other hand, clearly shows the oil slick.

It is well known that a single polarization channel system can detect oil slicks. Over the last decades, SAR polarimetry has been explored with the intention of extracting even more information from oil slicks and for improving the oil detection performance. The successive sections provide the necessary background for Papers I-III.
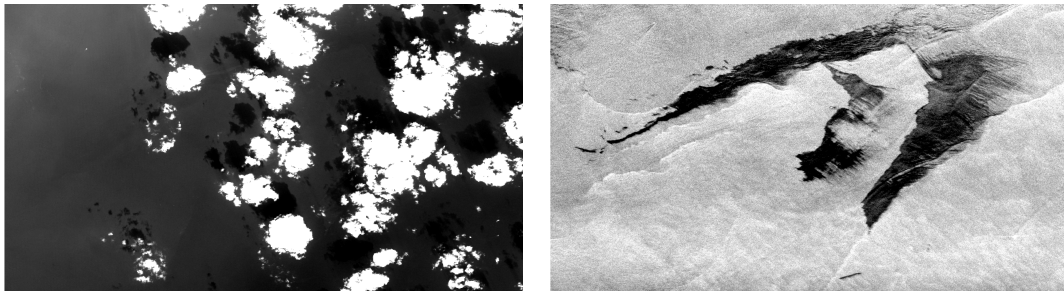
Figure 3.1: Left: Landsat-8 image (Landsat-8 product provided by USGS/NASA Landsat Program). Right: VV-intensity from UAVSAR. UAVSAR data courtesy of NASA/JPL-Caltech.

3.1   Oil Properties and Weathering Processes

The term "oil" is used to describe a wide variety of natural substances of plant, animal, and mineral origin. Crude oil and derived petroleum products contain dozens of major hydrocarbon compounds and thousands of minor ones [Coleman, 2003] generated by geological and geochemical processes. The fate and behaviour of oil in the marine environment are controlled by several physical properties like viscosity, density, solubility, and surface tension [Fingas, 2011]. Viscosity is the oil's resistance to flow, and low viscosity oils move readily compared to higher viscosity oils [Fingas, 2011]. High viscosity oils also tend to weather more slowly compared to low viscosity oils [Coleman, 2003]. The density is used by the petroleum industries to define light or heavy crude oil types and is an important property that indicates whether a certain oil will sink or float in water [Coleman, 2003]. Solubility in water is a measure of the amount of oil that will dissolve in the water on a molecular basis [Coleman, 2003].

These oil properties impact the efficiency of cleanup operations [Fingas, 2011] and change as the oil weathers on the sea surface. When crude oil is released onto the sea surface, it starts to undergo various physical (emulsification, evaporation, dissolution) and chemical (oxidation) weathering- and transport processes. These include spreading, dispersion and entrainment, sinking and sedimentation, partitioning and bioavailability, as well as stranding [Coleman, 2003]. Figure 3.2 illustrates these processes. All these processes alter the oil composition and oil thickness at the surface, which again influences the interaction

process between the incoming SAR pulses and the oil.
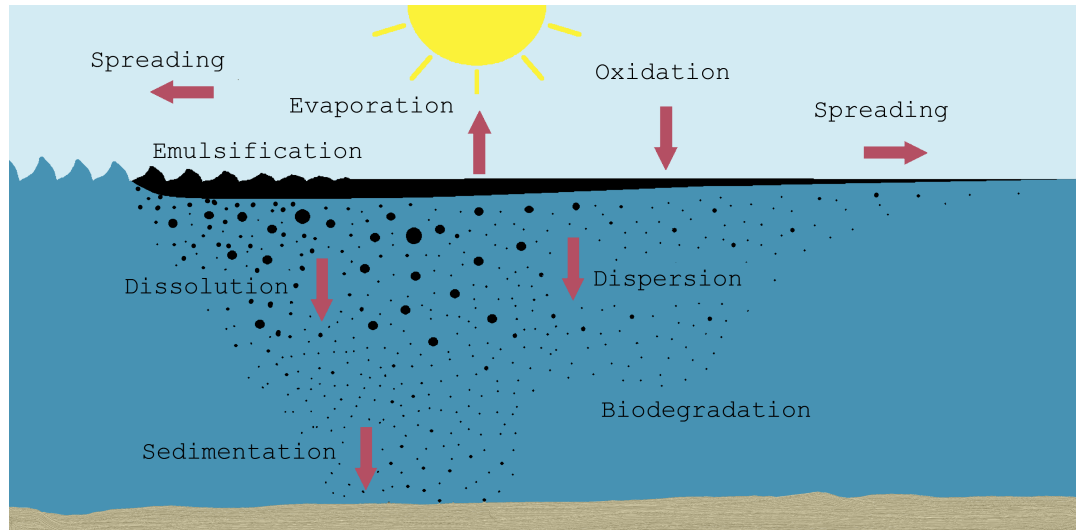
Figure 3.2: Weathering processes acting on an oil spill. The figure is from [Skrunes, 2014] and adapted from [ITOPF, 2002].

The wind and ocean currents play important roles in the oil slick transport (both horizontal and vertical movements) and weathering processes. The spreading of the oil is not necessarily uniform, and previous studies have found that more than 90% of the oil is located in less than 10% of the slick area [Hollinger and Mennella, 1973]. Furthermore, the weathering and wave actions cause the oil to mix with water. These factors might result in potential zoning within oil slicks. The wave-driven transport, known as the Stokes drift, as well as the ambient ocean current, transports the oil particles. Additionally, the oil slick drifts with approximately 3.5% of the wind speed [Schwartzberg, 1971]. Vertical movements contribute to mixing into the water column, which might lead to dispersion and break-up of the oil slick. Jones et al. [2018] compared a UAVSAR time series with an oil drift model (OpenDrift) to simulate the oil transport. Different oil types were released on a high-wind-driven sea surface. The authors discovered that by comparing the UAVSAR observations with the model simulations, one type of oil (biogenic oil) was shielded from the Stokes- and surface wind drift, and moved due to the Eulerian currents. This was a result of the vertical mixing into the water column, and only a few percents of the biogenic oil droplets were at the surface. On the other hand, a crude oil emulsion with 80% oil and 20% water drifted with the surface wind and Stokes drift, as well as the Eulerian currents. Based on the results from [Jones et al., 2018], it is clear that different types of oil react differently to these external drag forces.

3.2   Limitations of Oil Spill Observations by SAR

The SAR instrument is a valuable tool for oil spill monitoring, but there are several limitations associated with both detecting and characterizing the oil. Some examples are separating look-alikes from mineral oil, wind speed-, and sensor limitations.

3.2.1   Look-alikes

Mineral oil slicks produce a low-backscattering signature in SAR imagery. Unfortunately, several other phenomena also exhibit the same low-backscattering signatures. These are called oil spill look-alikes, and can be caused by low wind areas, natural biogenic slicks, wind shadowing due to coastal topography or man-made objects, rain cells, newly formed sea ice, upwelling, and internal waves [Clemente-Colón and Yan, 2000]. The most studied oil spill look-alike in SAR imagery is natural biogenic slicks (e.g., from algae and bacteria). As with mineral oil slicks, natural biogenic slicks will also dampen the capillary and small gravity waves [Fingas and Brown, 2014]. Therefore, several studies have explored SAR polarimetry and different sensors to separate the backscattered signal from mineral oil spills and biogenic surface films [Alpers et al., 2017], with various outcomes of success in specific cases. Natural biogenic slick areas are expected to form a monomolecular film on the sea surface due to their chemical composition [Hühnerfuss, 2006]. In contrast, crude oil or emulsified oil have a different composition than natural biogenic slicks, and the thickness of the crude oil is orders of magnitude higher than the monomolecular films [Hühnerfuss, 2006]. Efforts have been made in separating biogenic films from mineral oil spills using polarimetry (see, e.g., [Skrunes et al., 2014, Salberg and Larsen, 2018, Singha et al., 2013]), damping ratio (see, e.g., [Gade et al., 1998]), and multifrequency data (see, e.g., [Gade et al., 1998]). Figure 3.3 shows an example of an oil slick in near vicinity of an oil spill look-alike, which could either be a low wind area, ocean fronts, and/or a natural biogenic slick. The oil slick shown in Figure 3.3 was released close to this look-alike area, and identifying a way of separating the oil slick from the look-alike is extremely challenging. Paper I explores different polarimetric features as a function of time for one plant oil (simulant to biogenic slick) against three mineral oil emulsions.

3.2.2   Wind Speed Limitations

The wind is the main factor controlling the ocean surface roughness, and oil spill detection can only be performed in a limited range of wind speeds. If the wind speed is too low, the oil slicks are too similar to the calm smooth sea areas [Girard-Ardhuin et al., 2005]. If the wind is too strong, the oil might break and/or sink due to the turbulence of the upper surface layer. This might limit detection and also any discrimination between mineral oil and look-alikes. The optimal wind speed has been reported to be in the range 2-3 m/s to 10-14m/s [Alpers and Hühnerfuss, 1989, Singh et al., 1986].
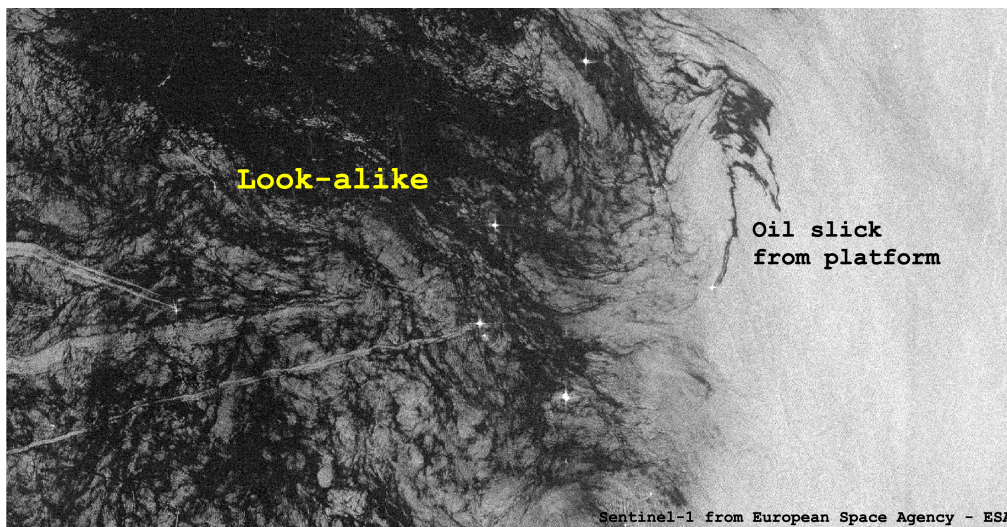
Figure 3.3: Sentinel-1 image of an oil slick in vicinity of oil spill look-alikes (most likely low wind areas, ocean fronts, or natural biogenic slicks).

3.2.3 Sensor Limitations

Each SAR sensor and its imaging modes have a variety of properties that impact the oil slick detection and characterization capabilities. It is well known that the backscatter response depends on the incidence angle. At low incidence angles specular reflection becomes important [Alpers et al., 2017, Gade et al., 1998], and the contrast between oil and the surrounding clean sea is low (see, e.g., [Minchew et al., 2012] for the copolarization channels). Low signal return from both oil slicks and clean sea occurs at high incidence angles [Minchew et al., 2012]. At higher incidence angles, less oil damping of the sea surface waves has been reported [Minchew et al., 2012], and sensor noise might also start to dominate the measured signal [Alpers et al., 2017]. As discussed in Section 2.7 several noise sources like thermal noise, quantization noise, sidelobe effects, and ambiguities will dilute the backscattered signal from oil slicks, and hamper any characterization and extraction of physical parameters like dielectric properties and volumetric fraction of oil.

Further, the temporal resolution of each satellite is poor, which limits the possibility of a high quality time series of drifting and evolving oil. However, due to the increasing number of active and planned satellites and microsatellites, the overall temporal resolution will improve if several sensors are combined. The search for oil spills requires a large swath width, which comes at a cost of few polarization channels and/or poorer spatial resolution. The use of HP modes can mitigate this as the polarimetric information level is somewhat comparable to a FP SAR system and offers twice the swath (or finer resolution) as a FP SAR system (see Section 2.4.4). The spatial resolution decides the minimum oil slick that is possible to detect, as coarse resolution modes might miss small oil slicks and also limit

observation of internal variations within the slick.

3.3   Sea Surface Scattering

The dominant scattering mechanism from the ocean is Bragg scattering, i.e., surface scattering. This is the most important scattering mechanism of the interaction between the EM wave and the ocean surface [Valenzuela, 1978]. However, typical Bragg scattering from the ocean might be influenced if an oil slick pollutes the clean sea area and introduces other effects that must be included. The polarization of the incoming EM wave also plays an important role in the scattering process, as the return for vertical polarization is greater than for horizontal polarization [Wright, 1968]. Further, the backscattering response increases as the incidence angle decreases and with increasing wind, i.e., rougher sea surface [Wright, 1968, Valenzuela, 1978]. The upcoming sections discuss some of the most frequently used scattering models for ocean surface scattering.

3.3.1   Scattering Models

The backscattering response over the ocean comes from small- to large-scale roughness components controlled by several processes like the wind and wave-wave interactions [Holt, 2004]. According to the Bragg scattering theory, the incident EM wave is backscattered by the wind-generated short wave component (Bragg waves) of the ocean surface waves, whose wavelengths (λ_B) are on the same order as the EM signal (λ) with the following relation:

$$\lambda_B = \lambda/(2\sin\theta) \tag{3.1}$$

where θ is the incident angle of the radar. According to the first order Bragg scattering model (also known as the small perturbation model (SPM)) the backscattering coefficients are generated in the following manner;

$$\sigma^0_{pq}(\theta) = 4\pi k^4 \cos\theta |R_{pq}|^2 W(2k\sin\theta, 0) \tag{3.2}$$

where p and q denotes the polarization of the incident and backscattered signal, θ is the incidence angle of an untilted horizontal plane, $W(\cdot)$ is the two-dimensional ocean wave spectral density, and k is the wavenumber. The Bragg scattering coefficients R_{pq} are expressed as [Valenzuela, 1978]:

$$R_{HH}(\theta, \epsilon_r) = \frac{\cos\theta - \sqrt{\epsilon_r - \sin^2\theta}}{\cos\theta - \sqrt{\epsilon_r + \sin^2\theta}} \tag{3.3}$$

$$R_{VV}(\theta, \epsilon_r) = \frac{(\epsilon_r - 1)(\epsilon_r(1 + \sin^2\theta) - \sin^2\theta)}{(\epsilon_r \cos\theta + \sqrt{\epsilon_r - \sin^2\theta})^2} \tag{3.4}$$

where ϵ_r is the relative dielectric constant. The Bragg scattering model simulates the backscatter from small-scale ocean surface roughness (at the Bragg wavelength), and excludes any effects of tilted facets that model longer waves, also known as large-scale roughness. Therefore, no cross-polarization nor depolarization effects are generated with this model. The longer waves will modify these short Bragg waves which impact the measured SAR signal [Vachon et al., 2004]. Figure 3.4 illustrates this concept, where the short waves, i.e., Bragg waves, rides on the longer waves. Scattering from each rough facet is evaluated by the first-order Bragg scattering model [Iodice et al., 2011]. Various two-scale models have been suggested for modelling the backscatter of both small- and large-scale ocean surface roughness components as illustrated in Figure 3.4. Examples of two-scale models are the tilted Bragg [Valenzuela, 1978], X-Bragg [Hajnsek et al., 2003], and the polarimetric two-scale model [Iodice et al., 2011]. Each of these two-scale models has a different approach to modeling the tilts, slopes, and/or rotation of the surface facets. Only the intensities are generated in the tilted Bragg model, whereas the entire covariance/coherency matrix can be simulated from the X-Bragg and the polarimetric two-scale models. The tilted Bragg model has been the most frequently used for oil spill remote sensing, and in this case the backscattering response is modeled as [Valenzuela, 1978];

$$\sigma^0_{HH}(\theta_i) = 4\pi k^4 \cos^4 \theta_i \left| \left(\frac{\sin(\theta + \psi_{ti}) \cos \zeta_{ti}}{\sin \theta_i} \right)^2 R_{HH}(\theta_i) + \left(\frac{\sin \zeta_{ti}}{\sin \theta_i} \right)^2 R_{VV}(\theta_i) \right|^2 \times$$
$$W(2k \sin(\theta + \psi_{ti}), 2k \cos(\theta + \psi_{ti}) \sin \zeta_{ti}) \tag{3.5}$$

$$\sigma^0_{VV}(\theta_i) = 4\pi k^4 \cos^4 \theta_i \left| \left(\frac{\sin(\theta + \psi_{ti}) \cos \zeta_{ti}}{\sin \theta_i} \right)^2 R_{VV}(\theta_i) + \left(\frac{\sin \zeta_{ti}}{\sin \theta_i} \right)^2 R_{HH}(\theta_i) \right|^2 \times$$
$$W(2k \sin(\theta + \psi_{ti}), 2k \cos(\theta + \psi_{ti}) \sin \zeta_{ti}) \tag{3.6}$$

$$\sigma^0_{HV}(\theta_i) = \sigma^0_{VH}(\theta_i) = 4\pi k^4 \cos^4 \theta_i \left(\frac{\sin(\theta + \psi_{ti}) \sin \zeta_{ti} \cos \zeta_{ti}}{\sin^2 \theta_i} \right)^2 \times$$
$$|R_{VV}(\theta_i) - R_{HH}(\theta_i)|^2 \times W(2k \sin(\theta + \psi_{ti}), 2k \cos(\theta + \psi_{ti}) \sin \zeta_{ti}) \tag{3.7}$$

where θ_i is the local incidence angle relative to the tilted facet. The tilts are defined by ψ_{ti} and ζ_{ti}, where the normal to the facet deviates from the vertical by ψ_{ti} in the incidence plane and deviates by an angle ζ_{ti} in the plane perpendicular to the plane of incidence [Valenzuela, 1978]. It can be seen from Equations 3.5-3.6 that the ratio of $\sigma^0_{HH}/\sigma^0_{VV}$ cancels the ocean wave spectrum $W(\cdot)$, i.e., the small-scale ocean surface roughness. Unfortunately, the tilted Bragg model cannot be used for modelling the response from a HP SAR system, since the co- and cross-polarization intensity coefficients are no longer available in HP. The X-Bragg model in [Hajnsek et al., 2003] or the polarimetric two-scale model in [Iodice et al., 2011] outputs the 3×3 covariance/coherency matrix. The backscattering coefficients for a HP SAR can be modelled using the X-Bragg and the polarimetric two-scale models, since a connection between the HP and the covariance/coherency matrix exist [Raney, 2007]. The X-Bragg model is an extension of the SPM, where

the complex scattering matrix is [Hajnsek et al., 2003, Iodice et al., 2011]:

$$S = a_s R(\phi) \begin{bmatrix} R_{HH}(\theta_i, \epsilon_r) & 0 \\ 0 & R_{VV}(\theta_i, \epsilon_r) \end{bmatrix} R^T(\phi) \tag{3.8}$$

where $|a_s|^2 = k_r^4 \cos^4(\theta_i) W(\cdot)$ contains factors related to the small-scale roughness like the small-scale ocean surface roughness, incidence angle, and wave number. The tilt of the facet causes a rotation of the local plane of incidence around the look direction by an angle ϕ [Lee et al., 2000]. $R(\phi)$ depends on the radar look angle and the surface slope (range and azimuth directions) or large-scale roughness [Cloude, 2010, Lee et al., 2000], and is expressed as:

$$R(\phi) = \begin{bmatrix} \cos\phi & \sin\phi \\ -\sin\phi & \cos\phi \end{bmatrix} \tag{3.9}$$

Calculating the expression in Equation (3.8) gives:

$$S = \begin{bmatrix} S_{HH} & S_{HV} \\ S_{HV} & S_{VV} \end{bmatrix}$$

$$= a_s \begin{bmatrix} R_{HH}(\theta_i, \epsilon_r)\cos^2\phi + R_{VV}(\theta_i, \epsilon_r)\sin^2\phi \\ \cos\phi\sin\phi(-R_{HH}(\theta_i, \epsilon_r) + R_{VV}(\theta_i, \epsilon_r)) \end{bmatrix} \cdots \tag{3.10}$$

$$\cdots \begin{bmatrix} \cos\phi\sin\phi(-R_{HH}(\theta_i, \epsilon_r) + R_{VV}(\theta_i, \epsilon_r)) \\ R_{VV}(\theta_i, \epsilon_r)\cos^2\phi + R_{HH}(\theta_i, \epsilon_r)\sin^2\phi \end{bmatrix}.$$

From Equation 3.8, the covariance and coherency can be estimated. The X-Bragg can be used to model the complex scattering vector for a HP system in the following manner [Salberg et al., 2014]:

$$k_{(RH,RV)} = \begin{bmatrix} S_{RH} \\ S_{RV} \end{bmatrix} = \frac{a_s}{\sqrt{2}} \begin{bmatrix} R_{HH}(\theta_i, \epsilon_r)\cos^2\phi + R_{VV}(\theta_i, \epsilon_r)\sin^2\phi + \\ \cos\phi\sin\phi(R_{VV}(\theta_i, \epsilon_r) - R_{HH}(\theta_i, \epsilon_r)) - \end{bmatrix}$$

$$\begin{bmatrix} j(\cos\phi\sin\phi(R_{HH}(\theta_i, \epsilon_r) - R_{VV}(\theta_i, \epsilon_r))) \\ j(R_{HH}(\theta_i, \epsilon_r)\sin^2\phi + R_{VV}(\theta_i, \epsilon_r)\cos^2\phi) \end{bmatrix}. \tag{3.11}$$

From Equation 3.11, the HP covariance matrix and the Stokes vector can be estimated. Both the tilted Bragg and X-Bragg are two-scale models that extend the SPM model with tilted/rotated facet, but the difference between tilted Bragg and X-Bragg is in how they model the tilt. X-Bragg uses a single rotation angle, whereas the tilted Bragg uses two tilt angles. There is a connection between the rotation angle in X-Bragg model and the two tilt angles in the tilted Bragg model, which was demonstrated in [Salberg et al., 2014]. Both the tilted Bragg and X-Bragg models are used in Paper I, and other studies using these models are [Minchew, 2012, Minchew et al., 2012, Salberg et al., 2014, Yin et al., 2015, Buono et al., 2019, Buono et al., 2016a].
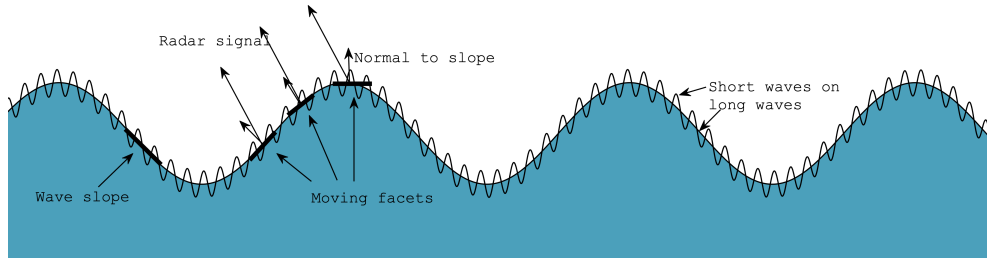
Figure 3.4: Illustration of small- and large-scale ocean surface roughness. The roughness within each facet is considered as the small-scale roughness, whereas the large-scale roughness is composed of many tilted facets. Figure adapted from [Holt, 2004, Shokr and Sinha, 1985].

3.4 Oil Slick Detection and Characterization

Oil slicks dampen the capillary and short gravity waves resulting in reduced backscatter compared to the surrounding sea [Fingas and Brown, 1997]. The oil slicks are seen as dark patches in SAR images, and the contrast is controlled by several factors like sensor properties (e.g., frequency, polarization, incidence angle), oil slick characteristics, weathering processes, and environmental conditions. As mentioned in Section 2.8.1, roughness and dielectric properties are two main factors impacted by oil slicks, i.e., through damping of the small scale ocean roughness and a change in the dielectric properties between the oil slick and clean sea, where both factors result in a reduction in the backscattered signal. Polarimetric features are a key tool when analyzing the detection capabilities within both FP and DP SAR products, as features vary in their detection and characterization properties. The upcoming section highlights the concept of polarimetric features and how these can be used in both detection and characterization of oil slicks.

3.4.1 Polarimetric Features

The traditional SP SAR system was first used when monitoring oil spills. Since the SP system provides only one polarization channel, information such as the geometry and shape of the oil patch, oil-sea contrast, contextual features (wind history, location relative to ships, oil rigs, and shore), and texture were used to describe the segmented low-backscattering regions [Brekke and Solberg, 2005]. Over the last decade, the use of multipolarization features for detection and characterization purposes of low-backscattering ocean areas has been discussed frequently in the literature [Skrunes et al., 2014, Brekke et al., 2014, Migliaccio et al., 2009a, Brekke et al., 2017, Migliaccio et al., 2005, Zhang et al., 2017,

Skrunes et al., 2018, Salberg and Larsen, 2018, Singha et al., 2016, Li et al., 2016, Migliaccio et al., 2009b]. For several years, polarimetric features have been applied on all kinds of FP SAR data acquired under various wind- and ocean conditions and for different oil types. Polarimetric features are in general extracted from FP SAR products, but can also be extracted from DP SAR data when the two polarization channels are combined. Polarimetric features have seen extensive use when attempting to separate biogenic slicks from mineral oil slicks [Migliaccio et al., 2009b, Zhang et al., 2011, Skrunes et al., 2014, Zhang et al., 2017, Salberg and Larsen, 2018]. The polarimetric features are often used as input to various classification algorithms (see, e.g., [Salberg and Larsen, 2018, Zhang et al., 2017, Skrunes et al., 2014]), and/or separability measures when exploring the different polarimetric features' suitability for, e.g., detecting the oil and/or differentiating between types of surface films.

Polarimetric features extracted from HP SAR data have been increasingly discussed and studied in the literature [Nunziata et al., 2015, Salberg et al., 2014, Zhang et al., 2017, Brekke et al., 2017, Espeseth et al., 2017, Li et al., 2016]. The large interest is caused by the possibility of doubling the swath width compared to a FP SAR system, while at the same time retaining enough polarimetric information to describe the surface element. For oil slick monitoring this is beneficial as a large swath is necessary to cover a vast area. The FP features are extracted from both the sample covariance and coherency matrices, whereas the simulated HP features are extracted from the Stokes vector and the sample HP covariance matrix. Previous studies have investigated oil slick detection performance using features extracted from a simulated HP system and often compared the performance with features extracted from a FP system [Salberg et al., 2014, Zhang et al., 2017]. The results indicate a similar oil detection performance between a FP and HP system.

The features investigated in this thesis are grouped by their sensitivity to the physical parameters based on the two-scale Bragg models presented in Section 3.3. These are the small- and large-scale ocean surface roughness, incident angle, tilt angles, and the relative dielectric constant. Paper I identified two feature categories, shown in Table 3.1. In general, all the non-ratio-based features are found in category I and depends on small- and large-scale ocean surface roughness, relative dielectric constant, and incident angle, whereas the ratio-based belong to category II and depend on the large-scale ocean surface roughness, tilt angles, relative dielectric constant, and incident angle, i.e., they are independent of the small-scale roughness.

Figures 3.5 and 3.6 show examples of one feature from category I (the span), and one feature from category II (copolarization ratio). Here, based on visual inspection, the contrast between oil and the surrounding clean sea is higher for the span (category I) than the copolarization ratio (category II). In Figure 3.6, the top-most oil slick (a plant oil release during the oil-on-water exercise in 2013) is almost impossible to detect using the copolarization ratio, while it is visible using the span. The low visibility of the plant oil in the copolarization ratio is most likely due to the cancellation of the small-scale roughness (according to the two-scale Bragg models), which contains information about the damping

Table 3.1: Overview of the two categories that multipolarization features can be grouped into based on the two-scale Bragg models presented in Section 3.3.

Category I (non-ratio-based)	Large-scale roughness
	Small-scale roughness
	Incidence angle
	Dielectric properties
Category II (ratio-based)	Large-scale roughness
	Incidence angle
	Dielectric properties

of the small ocean waves. Since the plant oil forms a monomolecular layer, the EM wave penetrates the oil to scatter from the water. Hence, the dielectric constant of the plant oil will not influence the backscattered signal. The span (category I) shows higher contrast for the plant oil, indicating that the small-scale roughness is an important factor for detecting the plant oil.

Oil slicks seen in polarimetric SAR data are particularly susceptible to misinterpretation due to noise contamination, and the behaviour of these polarimetric features in the presence of noise contamination is explored in Paper II.
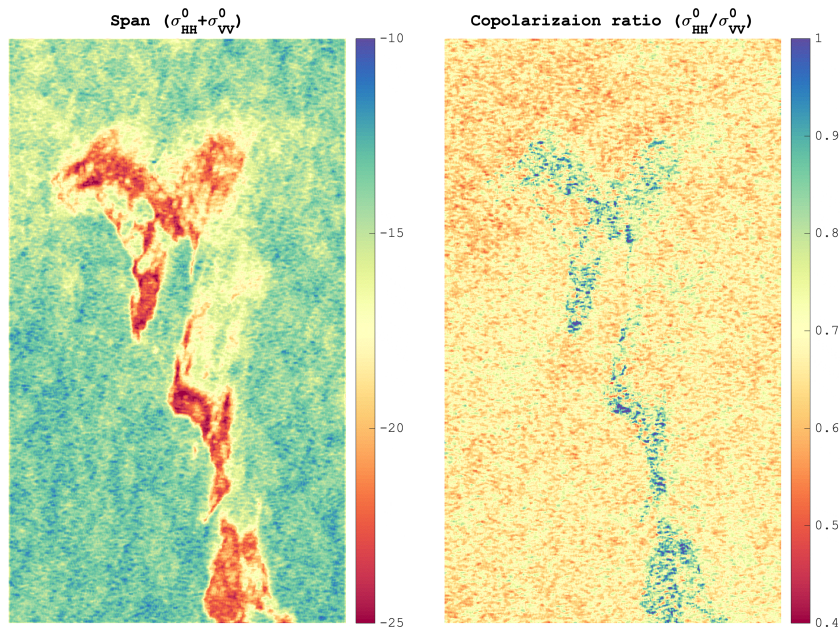
Figure 3.5: Pseudo-color images of the span (left panel) and copolarization ratio (right panel) of a Radarsat-2 acquisition (June 2012) covering mineral oil slicks from NOFO's oil-on-water exercise in 2012. The Radarsat-2 data and Products © MDA LTD. 2012– All Rights Reserved.
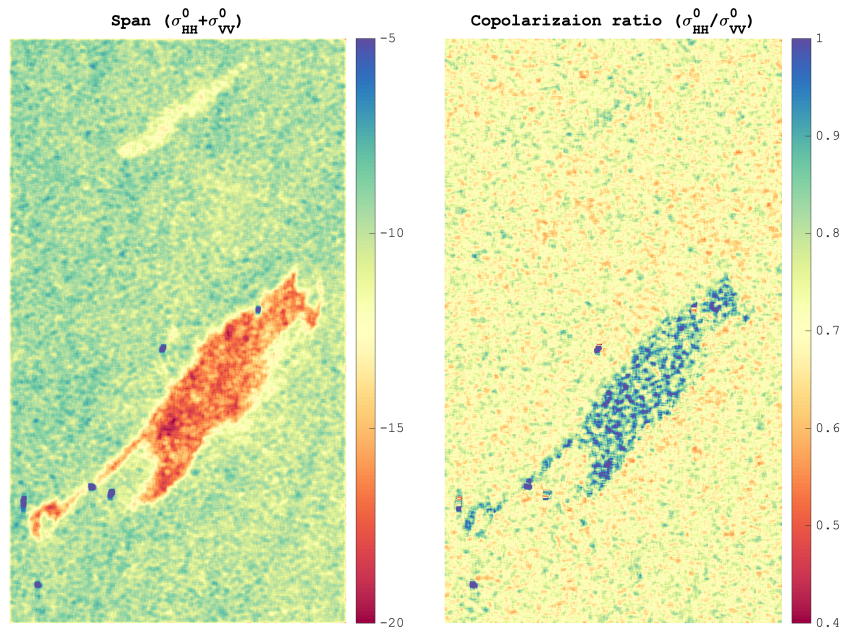
Figure 3.6: Pseudo-color images of the span (left panel) and copolarization ratio (right panel) of a Radarsat-2 acquisition (June 2013) covering plant oil (top-most slick) and mineral oil from NOFO's oil-on-water exercise in 2013. The Radarsat-2 data and Products $^{©}$ MDA LTD. 2013 – All Rights Reserved.

3.4.2   Damping Ratio

The damping ratio (DR) is a measure of the contrast between the oil and the surrounding clean sea [Gade et al., 1998], and is defined as

$$DR = \frac{\sigma^0_{clean\ sea}(\theta)}{\sigma^0(\theta)}. \tag{3.12}$$

The damping ratio has been reported to increase with wavenumber, oil viscosity, and thickness [Wismann et al., 1998, Gade et al., 1998, Pinel et al., 2014, Sergievskaya et al., 2019]. The wave damping of oil films are controlled by various physical parameters like for example the volume viscosity, surface and interfacial tensions, and elasticity [Sergievskaya et al., 2019, Jenkins and Jacobs, 1997]. Different oil types have unique physical and chemical compositions that might results in various damping ratio characteristics at different wavenumber and wind speed, allowing for discrimination of different oil types [Wismann et al., 1998, Gade et al., 1998, Jenkins and Jacobs, 1997]. A recent study [Sergievskaya et al., 2019] based on a laboratory experiment with two oil types (oil emulsion and crude oil) and different thicknesses demonstrated that the damping ratio increased with oil thickness, but reached a maximum value at a given oil thickness threshold that varied between the oil types. Higher damping was also reported for crude oil compared to oil

emulsion in [Sergievskaya et al., 2019]. Figure 3.7 shows the VV-intensity and the damping ratio from a Radarsat-2 scene covering three different types of oil acquired during NOFO's oil-on-water exercise in 2011. In Figure 3.7, the damping ratio is lower for plant oil compared to the mineral oil films. The damping ratio image also reveals internal variations within the slicks, which might indicate thickness variations. Information about the relative thickness within an oil slick might aid in identifying actionable oil, monitoring the dispersion and evolution of the oil, and for discriminating between different oil types. Skrunes et al. [2017] used overlapping infrared (IR) observations and a SAR acquisition to demonstrate that the high damping ratio area corresponded to the IR white region indicating relatively thick oil.

The damping ratio has been widely explored in this work, especially in Papers I and III, and is also the key concept of the innovation project presented in Chapter 11.
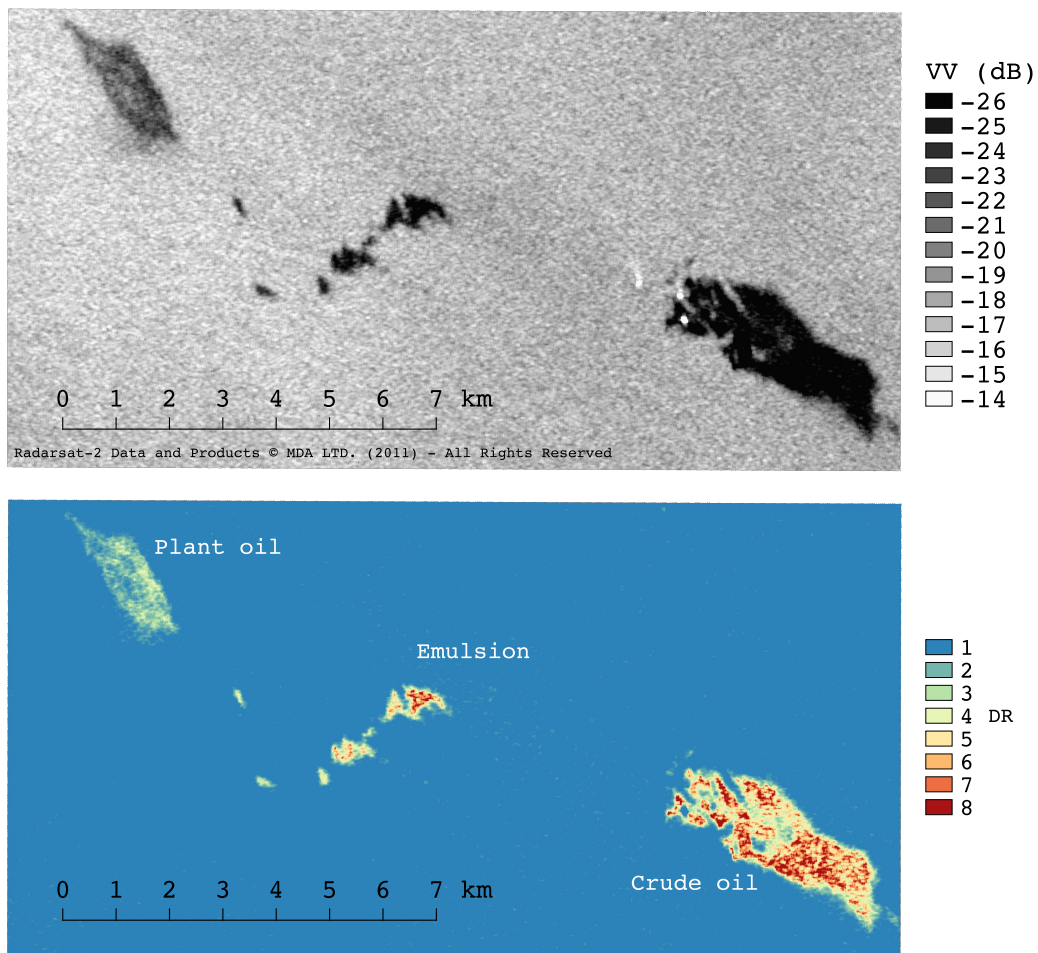
Figure 3.7: Top: VV-intensity of Radarsat-2 covering three different types of oil. Bottom: VV damping ratio (DR). The three oil types are displayed in the DR image.

4

SAR Remote Sensing of Arctic Sea Ice

Sea ice is mostly located in remote areas with challenging conditions of heavy cloud cover and darkness for several months of the year. SAR satellites overcome these challenges, and are therefore an important tool for sea ice monitoring. Operational sea ice services around the world rely on SAR observations when creating various types of ice charts. These ice charts are then used, for example, for risk assessment and to make efficient decisions when operating in ice infested areas. This is one of the main goals and motivations for CIRFA; extracting information from remote sensing to aid decision making in Arctic operations. Another important reason for studying sea ice is its role in the global climate. Sea ice has an impact on the environment and global climate through its interactions with the ocean and atmosphere, and influence heat and gas exchange between the water and atmosphere [Onstott and Shuchman, 2004].

X-, C-, L-band SAR satellites have been used frequently for studying the radar signatures of sea ice (see, e.g., [Eriksson et al., 2010, Dierking and Busche, 2006, Johansson et al., 2017, Singha et al., 2018]). The FP SAR mode has been shown to improve classification of various sea ice types (see, e.g., [Moen et al., 2015, Singha et al., 2018, Dierking et al., 2003]) compared to SP or DP SARs. However, monitoring of vast areas requires large spatial coverage, which comes at a cost of coarse resolution and fewer polarization channels. Therefore, the HP SAR mode could be an important turning point, providing both large coverage and improved polarimetric information compared to the conventional SP and DP modes currently available in Radarsat-2 and Sentinel-1. Furthermore, integrating different

sensors and modes will also increase the monitored area.

Paper IV focuses on sea ice from a HP perspective. Therefore, this chapter is limited to HP and provides the necessary background information for Paper IV.

4.1   Sea Ice Types

Sea ice generally consists of frozen water with inclusion of liquid brine pockets and gas bubbles. However, depending on atmospheric and ocean conditions, sea ice may appear in a large variety of forms. The sea ice is often labeled for classification purposes according to different properties such as thicknesses, sea ice concentration levels, sea ice age, or floe sizes [Onstott and Shuchman, 2004]. For example, sea ice classification from SAR data often uses sea ice labels defined by The World Meteorological Organization [WMO-No.574, 2010]. Various sea ice types have different EM signatures due to variations in surface roughness and composition. In the Norwegian Arctic, first-year ice, young ice, fast ice, and multi-year ice are the dominant types. The salinity content varies between these ice types and the brine pockets within the ice affect the radar signatures [Onstott and Shuchman, 2004]. The importance of volume- and multiple scattering will increase with snow thickness [Gill et al., 2015], resulting in different radar signatures between an ice layer with and without a snow layer. Figures 4.1 and 4.2 show example images of some sea ice types: nilas, lead, ridges, floes, multi-year-ice, and grey-white ice.
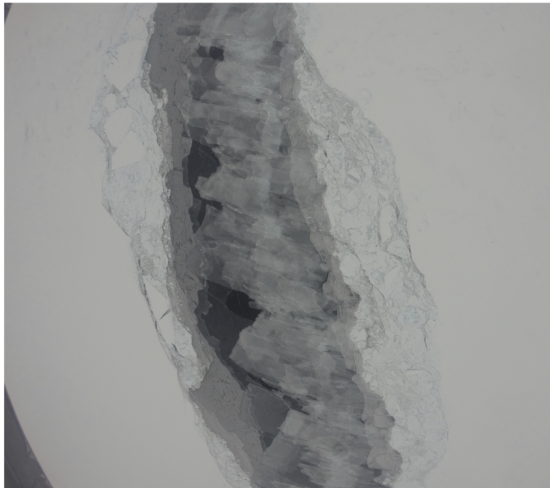
Nilas formed in calm water
Photographs courtesy Martine Espeseth, N-ICE 2015, Norweigan Polar Institute , Date: May 2015
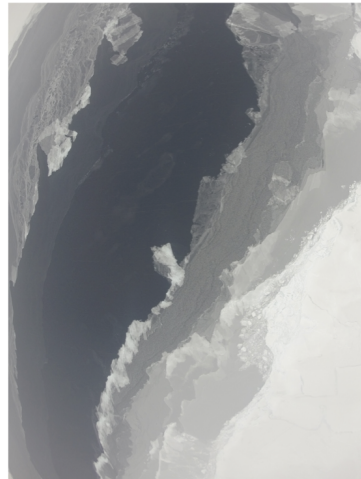
Lead
Photographs courtesy Martine Espeseth, N-ICE 2015, Norweigan Polar Institute, Date: May 2015

Figure 4.1: Photos of different sea ice types in the Barents Sea acquired during the N-ICE project managed by the Norwegian Polar Institute.

Ridges
Photographs courtesy Martine Espeseth, N-ICE 2015,
Norweigan Polar Institute, Date: May 2015

Floes
Photographs courtesy Martine Espeseth, N-ICE 2015,
Norweigan Polar Institute, Date: May 2015
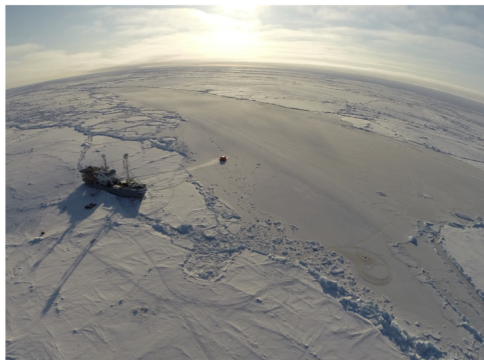
Multi-year ice (left corner) and newly formed ice
(right side of the photo)
Photographs courtesy Sebastian Sikora, UNIS, N-ICE 2015,
Norweigan Polar Institute, Date: May 2015

Grey-white ice covered with 2-3 cm of snow
(removed manually on the lower corner of the photo)
Photographs courtesy Martine Espeseth, N-ICE 2015,
Norweigan Polar Institute, Date: May 2015

Figure 4.2: Photos of different sea ice types in the Barents Sea acquired during the N-ICE project managed by the Norwegian Polar Institute.

4.2   Scattering Characteristics of Sea Ice

The backscatter signature of sea ice depends on the ice type, the sensor properties (e.g., frequency, polarization, incidence angle), and other environmental factors like season, temperature, etc. The surface characteristics depend on a combination of four surface parameters: (1) surface roughness (both large and small scales); (2) the complex dielectric constant of sea ice; (3) dielectric discontinuities or discrete scatterers (e.g., gas bubbles in the ice); (4) orientation of the ice and its surface features to the radar [Onstott and Shuchman, 2004]. As mentioned in Section 2.8.1, the surface is considered rough if the Rayleigh criterion (see Equation 2.17) is satisfied. Hence, X-band SAR is more sensitive to small-scale roughness of sea ice than C- and L-band SAR. The roughness is a key parameter in the backscatter as compared to the dielectric properties [Spreen and Kern, 2016]. Figure 4.3 shows overlapping Sentinel-1 (C-band SAR) and Sentinel-2 (optical) images covering Arctic sea ice. The leads can be seen as dark features in both the optical

and SAR image, whereas the other sea ice types have different visual appearance in the two images.

For EM scattering of sea ice and snow-covered surfaces, two main processes take place: surface and volume scattering [Spreen and Kern, 2016]. The penetration depth controls the scattering processes that might take place. Since L-band waves penetrate deeper than X- and C-band waves, more volume scattering might occur. Although the penetration depth depends on the frequency and incident angle of the EM wave, it also depends on the surface characteristics like the temperature, dielectric properties, and porosity of the ice and wet snow [Onstott and Shuchman, 2004, Spreen and Kern, 2016]. The penetration depth is low for sea ice and snow (but it is much lower for water), hence the surface scattering is considered to be the dominant scattering mechanism for sea ice, especially for young and first-year ice [Spreen and Kern, 2016]. Volume scattering within the sea ice might happen due to brine pockets (first-year ice), drainage structures, or air bubbles (multi-year ice) [Winebrenner et al., 1989]. The EM penetration depth and volume scattering are related to the age of the sea ice [Spreen and Kern, 2016].
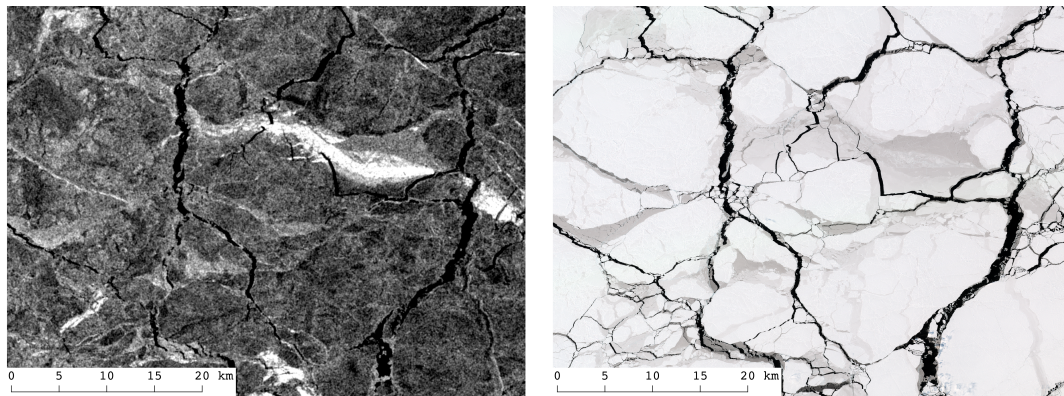
Figure 4.3: Left: Sentinel-1 HH-intensity image of Arctic sea ice acquired 5 April 2016 at 15:38 UTC. Right: RGB-image of Sentinel-2 over the same area acquired 5 April 2016 at 20:33 UTC. Sentinel-1 and Sentinel-2 data from European Space Agency - ESA.

4.3   Characterizing Sea Ice with Hybrid-Polarity SAR

The use of FP SAR data has been shown to enhance discrimination between various sea ice types as well as between open water and sea ice [Geldsetzer et al., 2015, Moen et al., 2015, Singha et al., 2018, Dierking et al., 2003]. This improvement comes at a cost of a limited swath width (25-50km) and is therefore unfit for most operational use cases. With the HP mode available, this compromise may no longer be necessary. The reason for the large interest in the HP mode for sea ice monitoring is the RCM (launched in 2019), which has HP capabilities. Understanding the benefit and limitations of the HP system can thus be granted some importance. Moreover, various polarimetric features retrieved from

simulated HP SAR have been the main focus in multiple studies [Dabboor and Geldsetzer, 2014b, Dabboor and Geldsetzer, 2014a, Geldsetzer et al., 2015, Xi et al., 2016]. All have shown good performance of the HP mode. Most sea ice studies (see, e.g., [Dabboor and Geldsetzer, 2014b, Dabboor and Geldsetzer, 2014a, Geldsetzer et al., 2015, Xi et al., 2016]) with a focus on a HP SAR system simulate HP data from FP data, resulting in synthesizing of a perfectly transmitted circularly polarized wave. Transmitting a perfectly circular polarized wave is not possible using current technology, and the transmitted pulse will rather be more elliptical [Touzi and Charbonneau, 2014]. This is referred to as "the non-circularly" property of a HP system [Touzi and Charbonneau, 2014]. Hence, when simulating HP from FP this should be considered when exploring the polarimetric signatures of e.g., sea ice.

Another way of exploring HP SAR data is reconstruction of a pseudo FP covariance matrix [Souyris et al., 2005]. Espeseth et al. [2016] investigated various reconstruction methods for C- and L-band SAR covering overlapping areas of Arctic sea ice. This study discovered higher reconstruction accuracy for L- than C-band SAR data, which might have been because L-band is more exposed to volume scattering due it is higher penetration depth than C-band. The papers presented in this thesis do not perform any reconstruction. This makes it possible to avoid the scattering symmetry assumptions introduced in a reconstruction approach.

4.3.1   Hybrid-Polarity Features for Sea Ice Observations

The HP SAR features are derived from the HP 2×2 sample covariance matrix or the Stokes vector (see Section 2.4.4). A large feature set has been investigated for sea ice studies, but the majority of these studies have considered simulated- and not real HP data. Polarimetric features have proven to be sensitive to various surface characteristics like dielectric property, surface roughness, and amount of brine pockets and air bubbles. Geldsetzer et al. [2015] categorized several HP features into groups based on their sensitivity to a given scattering mechanism. This framework is also adopted in Paper IV and Table 4.1 shows the categorizes. The first distinct groups isolate sensitivity to strong surface scattering, depolarization due

Group #	Scattering process
Group 1	Strong surface scattering
Group 2	Depolarization due volume scattering
Group 3	Depolarization due to multiscattering from rough surfaces
Group 4	Polarization differences in resonant Bragg scattering or in Fresnel coefficients
Independent	Complementary to other physical parameters

Table 4.1: Groups defined in [Geldsetzer et al., 2015] and their sensitivity to the scattering processes.

to volume scattering, depolarization due to multiscattering, and polarization differences in resonant Bragg scattering. The "independent" group corresponds to features that might

be sensitive to other characteristics that are not covered by Groups 1 - 4. Within each group, there exist several HP features. For example, most of the intensity features, like the first Stokes parameter and the single *RH* and *RV* intensities are found in Group 1, whereas, the degree of polarization (DoP) and the magnitude of the *RV* and *RH* cross-correlation are found in Group 3.

5

Data Collection

Lack of ground truth information of an oil spill or sea ice can lead to speculations and misinterpretations of the remote sensing data. This is a major challenge for the scientific community working with remote sensing data. Therefore, data collection during the exercises and campaigns are unique opportunities to understand the SAR signatures of different types of oil and sea ice.

This chapter describes the exercises and campaigns from which the data used for this work originates. Section 5.4 gives an overview of the SAR data used for the papers presented in this thesis.

5.1 Oil-On-Water Exercise in the North Sea

The organization NOFO has conducted several exercises outside the abandoned Frigg field in the North Sea (see Figure 5.1) for several years, where oil is released under controlled supervision. NOFO is an oil spill response organization with members from all the oil companies operating in the Norwegian continental shelf. The main vision of NOFO is "keeping the sea clean", and the exercise is conducted with the purpose to both implement and test new clean-up systems and to ensure their oil recovery preparedness [NOFO, nd]. Norway is one of a few countries that conducts such experiments. Because of this, the exercises have gained international attention both within the research communities and various industries.

A SAR image of an oil spill is much more valuable if in-situ information about the spill is available. This is rarely the case, and remote sensing images from these oil-on-water exercises, where in-situ information is available, are extremely important to obtain knowledge about the development and properties of an oil spill. In-situ data such as the type and amount of oil, as well as the oil/water fraction, and release time and position are collected during these exercises. Additionally, wind information is collected, and in some cases drift buoys are released to record information about the ocean drift currents. Remote sensing data from these exercises have lead to several publications with scientific contributions. This includes studies on the polarimetry in terms of detection and characterization of the oil slicks (see, e.g., [Brekke et al., 2017, Angelliaume et al., 2018, Skrunes et al., 2014, Skrunes et al., 2015, Skrunes et al., 2018, Skrunes et al., 2016]), and oil drift models (see, e.g., [Röhrs et al., 2018, Jones et al., 2016]).
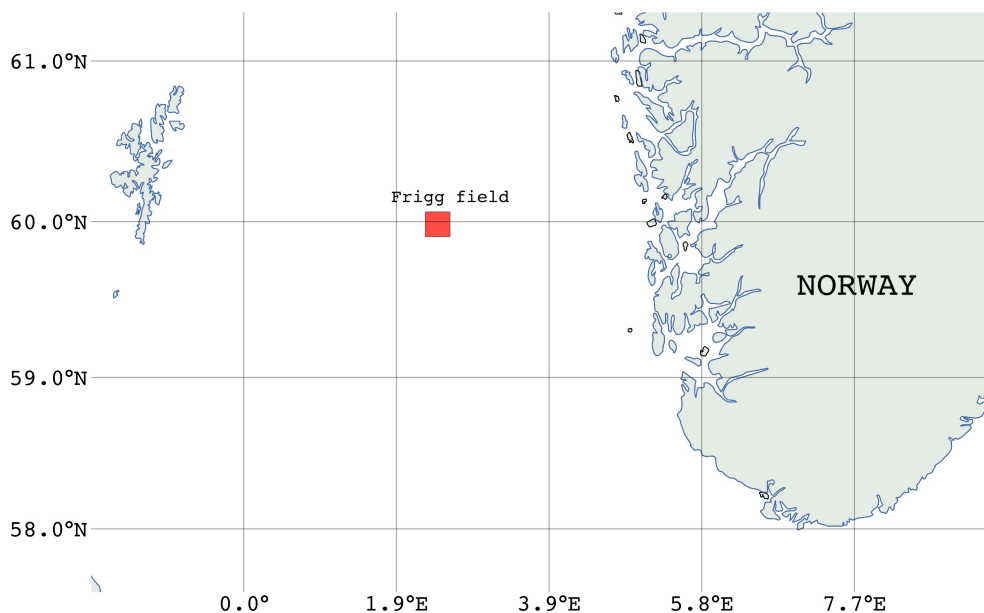
Figure 5.1: Map showing the location of the Frigg field where the oil-on-water exercise takes place.

Paper I and Paper II, presented in Chapter 6, used data that were collected during the oil-on-water exercises in the time period 2011-2018.

5.2 Seep in MC-20 block in the Gulf of Mexico

Oil seeps are a large source of oil entering the ocean. Oil seeps can be naturally occurring or a result of a leakage from oil and gas operations. The Gulf of Mexico is known to have a large number of seeps, and there have been numerous reports of oil slicks. One such event

in the Gulf of Mexico occurred in the aftermath of a hurricane that destroyed the Taylor Energy platform in the Mississippi Canyon Block 20 (MC-20) in September 2004 [Sun et al., 2018]. In the following years, oil films were detected in the same area where the oil platform was located before the hurricane.

Several extensive campaigns investigating and collecting data from this particular site, known as the MC-20 oil spill, have taken place over the last years. This site is well studied, and several publications are available (see, e.g., [Sun et al., 2018, Asl et al., 2016, Androulidakis et al., 2018, Nunziata et al., 2019, Herbst et al., 2016, Warren et al., 2014, Jones and Holt, 2018]).

Figure 5.2 shows the area and oil slick masks extracted from the UAVSAR images used in Paper III. The coverage of the joint oil slick masks are shown in three different tones of grey from three UAVSAR time series (from dark to light respectively).
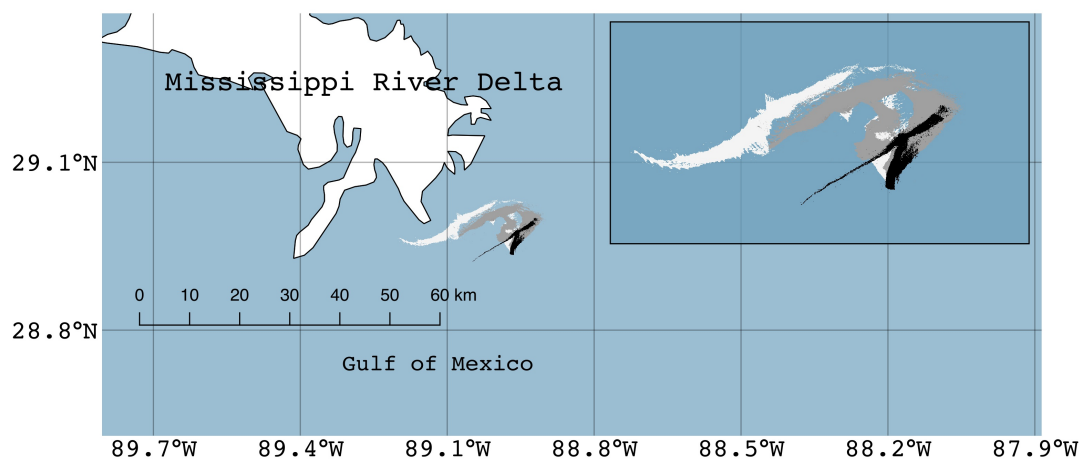
Figure 5.2: Map showing the location of the consistent seep in the MC-20 block in the Gulf of Mexico where the three UAVSAR time series (white, grey and black masks) were collected.

5.3 The Fram Strait Arctic Outflow Observatory

The Norwegian Polar Institute annually conducts a sea ice in-situ data collection in the Fram Strait. The main purpose of this campaign is to maintain an oceanographic mooring array that provides a time series of conditions, e.g., temperature, salinity, velocity, and sea ice thickness measurements in the Arctic Outflow. The ground truth information available in these remote areas allows for comparison of in-situ measurements with remote sensing data. During the 2015 Fram Strait campaign we had the opportunity to collect overlapping FP (Radarsat-2) and real HP (RISAT-1) C-band SAR data. A study (Paper IV) about the relationship between the two polarization modes using the overlapping SAR

scenes together with the sea ice observations was conducted. Sea ice types, snow-, and ice thickness were some of the in-situ information collected. Three overlapping RISAT-1 and Radarsat-2 scenes with less than 20 minutes time difference were collected (see Figure 5.3).
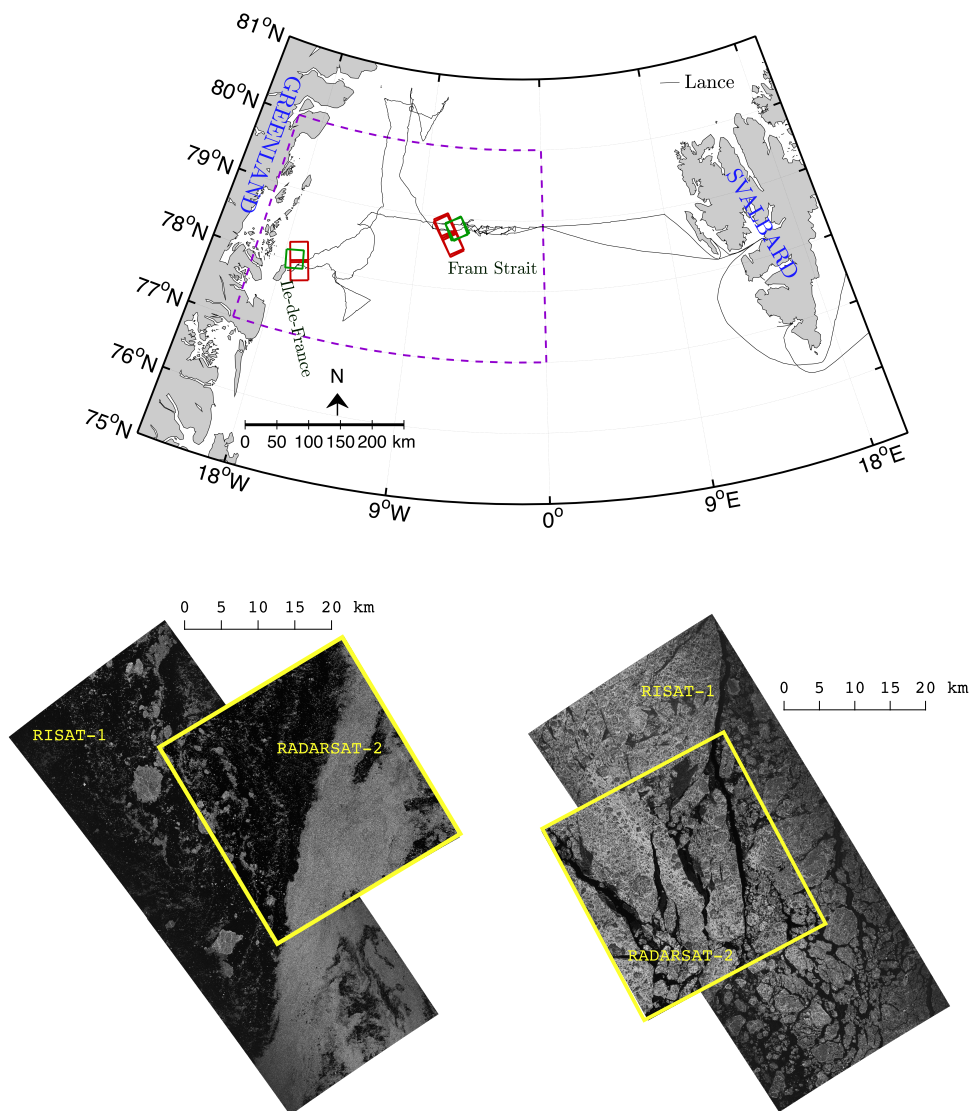
Figure 5.3: Top: Map with the locations of the overlapping scenes. The dashed square is the area of interest used in Paper IV. Bottom: Examples of two RISAT-1 and Radarsat-2 pairs used in Paper IV. The Radarsat-2 data and Products © MDA LTD. 2015 and RISAT-1 © 2015-Antrix-All rights reserved.

5.4 Remote Sensing Data Collection

Table 5.1 shows the different SAR sensors and imaging modes that are used in this thesis. UAVSAR (L-band sensor) and TerraSAR-X (X-band sensor) are only used for oil spill studies, whereas RISAT-1 (C-band sensor) is used only for the sea ice study presented in Paper IV. Radarsat-2 is used both for oil spill and sea ice studies. Note that RISAT-1 no longer is operational.

Table 5.1: Overview of the sensors used in this thesis and their properties [MDA, 2018] [Fritz and Eineder, 2010] [Fore et al., 2015] [Misra et al., 2013]. FRS-1 = Fine Resolution Stripmap. SSC = Single-look slant-range complex.

	TerraSAR-X	Radarsat-2	RISAT-1	UAVSAR
Frequency	X-band (9.65 GHz)	C-band (5.405 GHz)	C-band (5.35 GHz)	L-band (1.26 GHZ)
Mode	Stripmap SSC (Dual-pol)	Single Beam Fine Quad-pol	FRS-1 Dual-pol	Quad-pol
Polarization	HH,VV	HH,HV, VH,VV	RH, RV	HH,HV, VH,VV
Range swath[1]	15km	25km	25km	20km
Resolution[1] **(rg.**[2] **× az.)**	1.2×6.6m	5.2×7.6m	2×3m	2.5×1m
Incidence angle[1]	$15°\text{-}60°$	$30°\text{-}50°$	$12°\text{-}55°$	$25°\text{-}65°$
Paper #	II	I, II,IV	IV	I,II,III

[1]Nominal values.

[2]The range resolution is given in slant range.

/6

Overview of Publications

This chapter provides an executive summary of the four publications presented in Chapters 7-10.

6.1   Paper Summaries

Paper I

M. M. Espeseth, S. Skrunes, C. E. Jones, C. Brekke, B. Holt, and A. P. Doulgeris. "**Analysis of Evolving Oil Spills in Full-Polarimetric and Hybrid-Polarity SAR**", IEEE Transactions on Geoscience and Remote Sensing, vol. 55, no. 7, pp. 4190-4210, July 2017.

This paper presents, for the first time, an investigation of the difference between FP and HP SAR for a time series with short revisit time (20 minutes). One of the main objectives of this thesis is to explore the potential of HP SAR data, and how this mode performs in comparison with the well known FP SAR mode. This study investigates several polarimetric features extracted from FP and simulated HP data. The investigation involves identifying and comparing the features ability to separate various oil types from the surrounding clean sea. The two-scale Bragg models, namely the X-Bragg [Hajnsek et al., 2009] (referred to as the two-scale Bragg model in the paper) and the tilted Bragg [Valenzuela, 1978] are used when grouping the investigated FP and HP features into two categories that are either independent or dependent of the small-scale ocean surface roughness.

Short time series of the oil slick evolution is challenging to obtain using spaceborne SARs with and without full polarimetric capabilities. Since oil changes and evolves rapidly at the sea surface, short time difference between scenes is advantageous. Using airborne SAR, such as the UAVSAR, time series of SAR images can be gathered with high temporal resolution and full polarimetric capabilities. As a result of the low noise floor of the UAVSAR instrument, polarimetric features, and simulation of HP data can be used without too much noise contamination.

The overall conclusion is that the HP mode is comparable to the FP mode for oil versus sea separability. Furthermore, the features dependent on the small-scale roughness are the ones which exhibit highest separability between the various slick types and clean sea. It was not possible to separate the various types of oil using any of the investigated features. In general, the plant oil had higher detectability than the three emulsions across the time series. Furthermore, the features that contain the cross-polarization component are better for distinguishing the various oil slicks from clean sea. These cross-polarization features are not available in the HP mode, and alternative HP features are suggested in Paper I.

Errata

Some minor mistakes were discovered after publication of this paper, and these are listed here.

- Typo in the Bhattacharyya distance equation. The $\Sigma_i^{-1} + \Sigma_j^{-1}$ should have been $(\Sigma_i + \Sigma_j)^{-1}$.

- The calculation of the mean alpha angle was based on the coherency matrix, but the paper erroneously referred to this as the covariance matrix.

Paper II

M. M. Espeseth, C. Brekke, C. E. Jones, B. Holt, and A. Freeman "**Interpreting backscattering from oil spills in view of system noise in polarimetric SAR imagery**", IEEE Transactions on Geoscience and Remote Sensing, 2019, in review.

Several studies have argued that polarimetry can aid in understanding the scattering types within oil slicks, and use polarimetry for characterization. This can only be done if the signal is well above the noise floor. The limitation of polarimetric features and their behaviour with respect to system noise is evaluated in this paper. The motivation behind this study originates from several articles (see, e.g., [Alpers et al., 2017, Minchew et al., 2012, Skrunes et al., 2018]) showing their concerns on the influence of system

noise on several polarimetric features. Both multiplicative and additive system noise is investigated in this paper unlike several previous studies on SAR remote sensing of oil. The multiplicative system noise factors are quantization noise, ISLR effect, azimuth and range ambiguity and these are treated as another additive noise contribution in the measured signal. These sources are considered multiplicative since they depend on the mean signal level as opposed to the thermal noise.

This study shows a high correlation between the polarimetric feature values and system noise. The results demonstrate a significant reduction of the SNR when including the multiplicative system noise factors, which are usually not considered when estimating the SNR. Further, the authors recommend an SNR=10dB prior to any scattering analysis.

Several polarimetric features are investigated in this paper, and amongst these are the entropy and mean alpha angle commonly used in oil spill studies. This study confirms (also mentioned in e.g., [Minchew et al., 2012, Alpers et al., 2017]) that high entropy and high mean alpha angle for oil slicks are related to system noise and not a different scattering mechanism than the surrounding clean sea. In this study, we recommend not using H/α for oil spill scattering analysis. We also recommend a noise subtraction before any polarimetric analysis when characterizing the oil. However, the noise subtraction reduces the oil-sea contrast and should be avoided for oil slick detection purposes.

Paper III

M. M. Espeseth, C. E. Jones, B. Holt, C. Brekke, and S. Skrunes "**Oil Spill Response-Oriented Information Products Derived from a Rapid Repeat Time-Series of SAR Images**", IEEE Journal of Selected Topics in Applied Earth Observations and Remote Sensing, 2019, submitted.

This paper focuses on oil spill response-oriented information products derived from SAR data from an operational perspective. The study introduces two semi-automatable methods for investigating oil slick evolution using a time series of UAVSAR images. The methods show two ways of acquiring information about the changes and stability within an oil slick over a short time period using the damping ratio. The damping ratio is based on the VV-channel, and a single-polarization could therefore be used as input for the two methods. These methods are straightforward to implement and could potentially be used in an oil spill recovery process when time is of the essence. One method is used to identify locations within the slick that consistently exhibit a high damping ratio over a period of time, which might be categorized as actionable oil.

The other method provides an overview of the small-scale oil drift pattern using the mean difference between pairs of damping ratio images acquired with small time difference. Here, information about both oil movement and the change in backscatter within the oil slick can be obtained. The two methods are complementary in terms of identifying internal

variations within a slick, the oil drift pattern, and the weathering and accumulation of oil to form higher damping surface layers. These are important aspects in the planning and execution of a clean-up process.

Paper IV

M. M. Espeseth, C. Brekke, and M. Johansson, "**Assessment of RISAT-1 and Radarsat-2 for Sea Ice Observations from a Hybrid-Polarity Perspective**", Remote Sensing, vol. 9, no. 11, September 2017.

Paper I compares FP and simulated HP for oil spill detection. Similarly, Paper IV compares simulated HP with real HP for separating various sea ice types. Sea ice classification is important from a maritime perspective in ice infested waters to ensure safe and fuel-efficient passages. The heat and gas exchange is influenced by the sea ice types and their respective abundances. In this paper a unique data set of overlapping FP (Radarsat-2) and real HP (RISAT-1) are used. This data set provides the opportunity to test simulated HP with the real HP. The main objective of this study is to identify the dissimilarities and similarities between simulated and real HP data for different sea ice types. The analysis is based on 13 HP features that are sensitive to various scattering properties within the sea ice.

The results indicate a similar separability between the sea ice types using the real HP system in RISAT-1 and the simulated HP system from Radarsat-2. The HP features that are sensitive to surface scattering and depolarization due to volume scattering showed great potential for separating various sea ice types. A subset of features are affected, in terms of sea ice separability, by the non-circularity property of the transmitted wave in the simulated HP system across all the scene pairs. Overall, the best features, showing high separability between various sea ice types and which are invariant to the non-circularity property of the transmitted wave, are the RH- and RV-intensity coefficients and the first parameter in the Stokes vector.

6.2   Other Publications

As first author

1. M. Espeseth, C. Brekke, and S. N. Anfinsen, "**Hybrid-Polarity and Reconstruction Methods for Sea Ice With L- and C-Band SAR**", IEEE Geoscience and Remote Sensing Letters, vol. 13, no. 3, pp. 467-471, February, 2016.

2. M. Espeseth, S. Skrunes, C. Brekke, and A. B. Salberg, C. Jones, and B. Holt, "**Oil spill characterization in the hybrid-polarity SAR domain using log-cumulants**".

Proceedings of SPIE, the International Society for Optical Engineering, vol. 10004, 2016.

As co-author

3. A. Marinoni, M. Johansson, M. Espeseth, and C. Brekke, "**Multidi-mensional distance geometry analysis for classification of PolSAR images in Arctic scenarios.** Polarimetric Interferometric SAR (PolInSAR) conference, 2019.

4. S. Skrunes, C. Brekke, C. E. Jones, M. Espeseth, and B. Holt, "**Effect of Wind Direction and Incidence Angle on Polarimetric SAR Observations of Slicked and Unslicked Sea Surfaces**", Remote Sensing of Environment, vol. 213, pp. 73-91, 2018.

5. C. E. Jones, M. Espeseth, B. Holt, C. Brekke, "**Measurement of Oil Slick Transport and Evolution in the Gulf of Mexico using L-band Synthetic Aperture Radar**", 12th European Conference on Synthetic Aperture Radar (EUSAR), 2018.

6. S. Skrunes, C. Brekke, and M. Espeseth. "**Assessment of the RISAT-1 FRS-2 Mode for Oil Spill Observation.**" IEEE International Geoscience and Remote Sensing Symposium (IGARSS) proceedings, 2017.

7. C. Brekke, S. Skrunes, and M. Espeseth. "**Oil Spill Dispersion in Full-polarimetric and Hybrid-polarity SAR**". IEEE International Geoscience and Remote Sensing Symposium (IGARSS) Proceedings, 2017.

8. C. Brekke, C. E. Jones, S. Skrunes, B. Holt, M. Espeseth, and T. Eltoft, "**Cross-Correlation Between Polarization Channels in SAR Imagery Over Oceanographic Features.**" IEEE Geoscience and Remote Sensing Letters 2016, Volum 13 (7).

9. C. E. Jones, K.-F. Dagestad, Ø. Breivik, B. Holt, J. Röhrs, K. H. Christensen, M. Espeseth, C. Brekke, and S. Skrunes, "**Measurement and modeling of oil slick transport.**" Journal of Geophysical Research - Oceans, 2016, Volum 121 (10).

10. S. Skrunes, C. E. Jones, C. Brekke, B. Holt, and M. Espeseth, "**On the effect of imaging geometry on multipolarization SAR features for oil spill observation**". Proceedings of Living Planet Symposium, European Space Agency, 2016.

11. C. E. Jones, M. M. Espeseth, B. Holt, C. Brekke, and S. Skrunes, "**Characte-rization and discrimination of evolving mineral and plant oil slicks based on L-band synthetic aperture radar (SAR)**", Proceedings of SPIE, the International Society for Optical Engineering 2016; Volum 10003.

12. K. Blix, M. Espeseth, and E. Eltoft, "**Up-Scaling From Quad-polarimetric To Dual-polarimetric SAR Data Using Machine Learning Gaussian Process Regression**", IEEE International Geoscience and Remote Sensing Symposium (IGARSS) Proceedings, 2018.

13. K. Blix, M. Espeseth, and T. Eltoft, "**Machine Learning simulations of quad-polarimetric features from dual-polarimetric measurements over sea ice**", 12th European Conference on Synthetic Aperture Radar (EUSAR), 2018.

14. C. E. Jones, C. Brekke, Ø. Breivik, B. Holt, S. Skrunes, M. Espeseth, "**NORSE2015 - A Focused Experiment On Oil Emulsion Characterization Using PolSAR During the 2015 Norwegian Oil-On-Water Exercise**, AGU Oceans, 2016.

15. M. Johansson, M. Espeseth, C. Brekke, and S. Skrunes. "**Separation and characterisation of mineral oil slicks and newly formed sea ice in L-band synthetic aperture radar.**" IEEE International Geoscience and Remote Sensing Symposium (IGARSS) Proceedings, 2019.

16. A. Marinoni, M. Espeseth, P. Gamba, C. Brekke, and T. Eltoft. "**Assessment of Polarimetric Variability by Distance Geometry for Enhanced Classification of Oil Slicks Using SAR**". IEEE International Geoscience and Remote Sensing Symposium (IGARSS) Proceedings, 2019.

17. M. Espeseth, S. Skrunes, C. Brekke, and M. Johansson. "**The Impact of Additive Noise on Polarimetric RADARSAT-2 Data Covering Oil Slicks**". IEEE International Geoscience and Remote Sensing Symposium (IGARSS) Proceedings, 2019.

7

Paper I:

Analysis of Evolving Oil Spills in Full-Polarimetric and Hybrid-Polarity SAR

M. M. Espeseth, S. Skrunes, C. E. Jones, C. Brekke, B. Holt, and A. P. Doulgeris

8

Paper II:

Interpreting backscattering from oil spills in view of system noise in polarimetric SAR imagery

M. M. Espeseth, C. Brekke, C. E. Jones, B. Holt, and A. Freeman

9

Paper III:

Oil Spill Response-Oriented Information Products Derived from a Rapid Repeat Time-Series of SAR Images

M. M. Espeseth, C. E. Jones, B. Holt, C. Brekke, and S. Skrunes

10

Paper IV:

Assessment of RISAT-1 and Radarsat-2 for Sea Ice Observations from a Hybrid-Polarity Perspective

M. M. Espeseth, C. Brekke, and M. Johansson

11

Innovation

A key aspect of CIRFA is innovation that can aid the industry in utilizing remote sensing data to improve their monitoring and forecasting capabilities in the Arctic. Therefore, the innovation project conducted as part of this PhD work is presented in this thesis.

11.1 Objectives

The innovation project involves implementing an automatic algorithm that estimates the damping ratio of several SAR sensors and imaging modes. The future goal is to test and verify the relationship between the damping ratio (presented in Section 3.4.2) and the relative oil thickness for these products. This work was done in collaboration with KSAT located in Tromsø, in the time period February - June 2019. The main objectives were:

- To increase collaboration between the industry (KSAT) and CIRFA.

- To implement an algorithm that runs automatically on the SAR products.

- To test the algorithm on different sensors types/modes, oil types and oil slick areas provided by KSAT.

- To deliver the "damping ratio product" to NOFO during the oil-on-water exercise 2019, and to demonstrate its potential throughout and after the exercise.

11.2   Background Theory

Recall from Section 3.4.2 that the damping ratio (DR) is calculated as

$$DR_{x,y} = \frac{\sigma_y^{0,clean\ sea}}{\sigma_{x,y}^0}, \tag{11.1}$$

where $\sigma_y^{0,clean\ sea}$ represents a clean sea value at range position y, whereas $\sigma_{x,y}^0$ represents an intensity value at pixel location (x,y) (azimuth, range). $\sigma^{0,clean\ sea}$ is a clean sea profile of length equal to total number of pixels in range direction, and the same pixel value applies across azimuth direction for each range position.

To reduce the execution time of the algorithm, the estimation of the damping ratio can be done using the digital numbers (DN), and not on the radiometric calibrated sigma-nought values. This can be approximated by

$$DR_{x,y} = \frac{|DN_y^{clean\ sea}|^2 \sin(\theta_y)k_s}{k_s|DN_{x,y}|^2 \sin(\theta_y)} = \frac{|DN_y^{clean\ sea}|^2}{|DN_{x,y}|^2}, \tag{11.2}$$

where k_s is the calibration and processor scaling factor for SAR signals, and θ_y is the incident angle at range position y.

11.3   Product Overview

The algorithm was implemented at KSAT, primarily intended to run on scanSAR products from Radarsat-2, Sentinel-1, and COSMO-SKYMED. The drawback of the damping ratio is the need for a clean sea region, i.e., $\sigma^{0,clean\ sea}$. For the customers, the numerical values of the damping ratio are not relevant, and only the information about high or low damping is important (indicating relatively thick or thin oil). Hence, the damping ratio images strictly show the relative damping within oil slicks using different colors that reflects high or low damping ratio values. Currently, the color-scheme cannot be compared across different slicks within a scene, due to incident angle variations between the location of the slicks and the scaling that is performed on the damping ratio for each slick. It is well known that the VV polarization channel has the highest sea-oil contrast. Therefore, the VV-channel is used from all scanSAR DP (VV-VH) and FP SAR products.

During the project period at KSAT, the algorithm was tested on several oil types, such as produced water, mineral oil, and natural seep in various imaging modes and for different sensor types. One clear challenge of the damping ratio algorithm is low-wind areas, as these might influence the clean sea profile.

11.4   Implementation

The upcoming list describes the steps of the algorithm.

Trim land areas: The backscatter from land is high compared to the ocean, and could influence the clean sea profile. The land areas are therefore removed (set to NaN) using a SNAP graph[1].

Find clean sea profile: For homogeneous images, the clean sea profile decreases with increasing incidence angle. This profile is an array with length equal to the range of the image scene and is estimated by applying the median along the azimuth direction. The median is used since it is less affected by outliers (e.g., ships and low-wind areas).

Smooth clean sea profile: In the next step, a 3rd order polynomial function is fit to the median profile, to achieve a smoother profile. The fitted profile represents the $|DN^{clean\ sea}|^2$ in Equation 11.2.

Calculate the damping ratio: The fitted clean sea profile is divided by the DN image, according to Equation 11.2.

Extract oil slicks areas: Another input to the algorithm is the location of the oil slicks, which are provided by KSAT very shortly after the SAR image is acquired and downlinked. The oil slicks masks are segmented from SAR images by KSAT's operators daily. The oil slicks masks are used to create several damping ratio sub-images, where each sub-image covers one slick.

Outlier removal: The damping ratio values in each sub-image are scaled based on a lower and an upper percentile for each detected slick to remove outliers and for better visibility, and converted to uint-8. The damping ratio integer values are then linearly mapped to 11 colors representing low to high damping ratio. 11 colors were selected to visualise variations within the oil slick and were inspired by Figure 9 in [Fingas and Brown, 2014].

The fitted profile represents the $|DN^{clean\ sea}|^2$ in Equation 11.2. Figure 11.1 shows an example of the DN image (in VV) from Sentinel-1, and the bottom panel of Figure 11.1 shows the median profile along range direction and the fitted profile. There are several ships and platforms in the Sentinel-1 image, which can be seen as bright pixels. The effect of these bright spots cannot be observed in the median or fitted profiles of Figure 11.1.

The outputs of the algorithm are GeoTIFF-files and a PDF report. Figures 11.2-11.4 show

---

1. European Space Agency (ESA) provides free open-source toolboxes, known as SNAP, for scientific exploitation (see `http://step.esa.int/main/`)

two examples of the damping ratio PDF-report that is generated automatically from the algorithm.
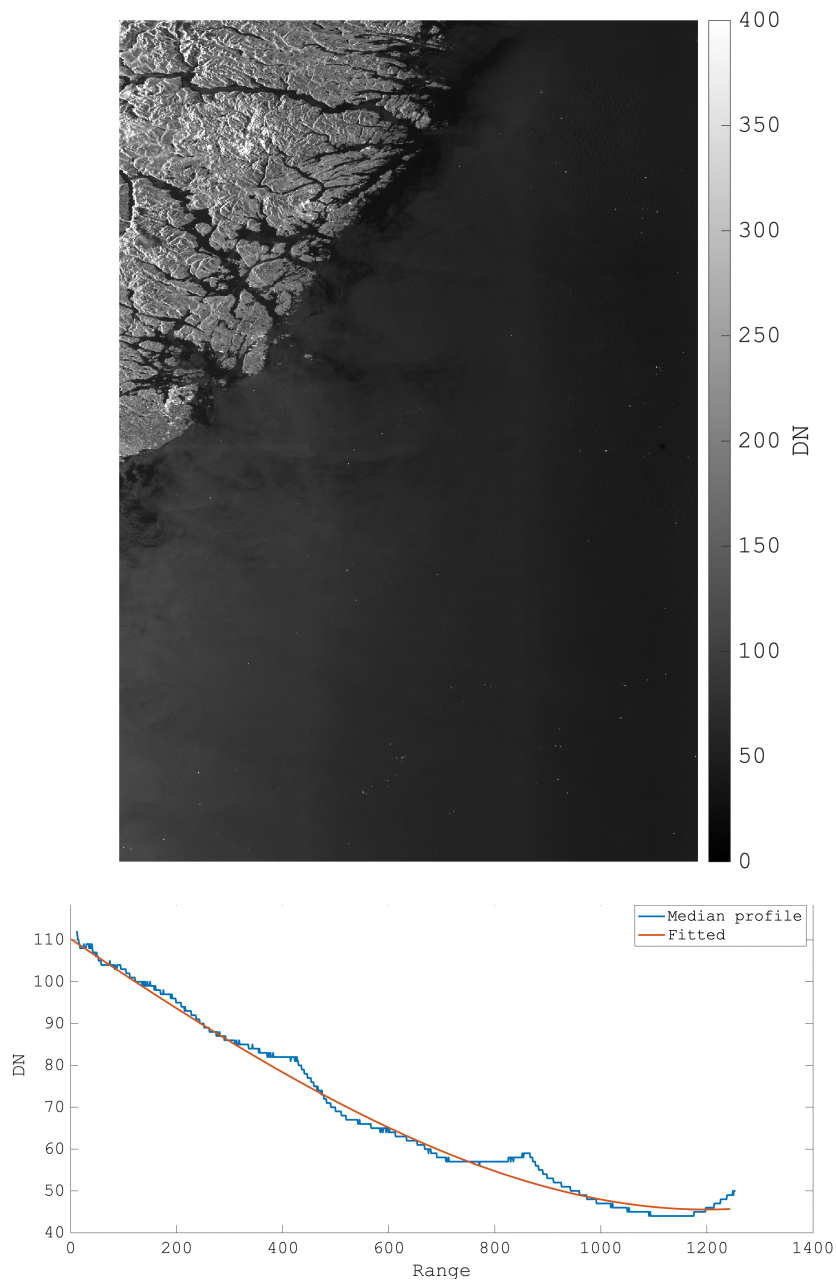
Figure 11.1: Top: Digital number image of the VV-channel from Sentinel-1 acquired 11 July 2018. Sentinel-1 from European Space Agency - ESA. Bottom: Median profile and the fitted profile along range direction of the DN image.

Figure 11.2: Example of one SAR damping ratio report of an archived Sentinel-1 acquisition (page 1). See Figure 11.3 for the second page.
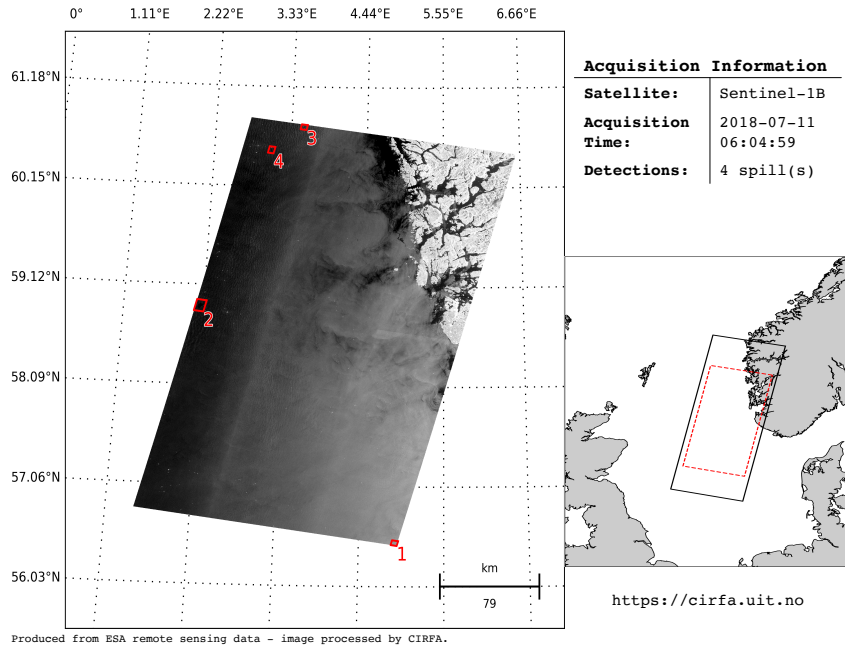
Slick #2
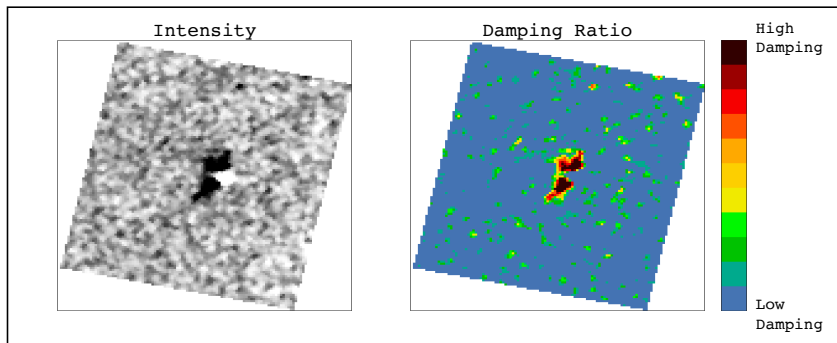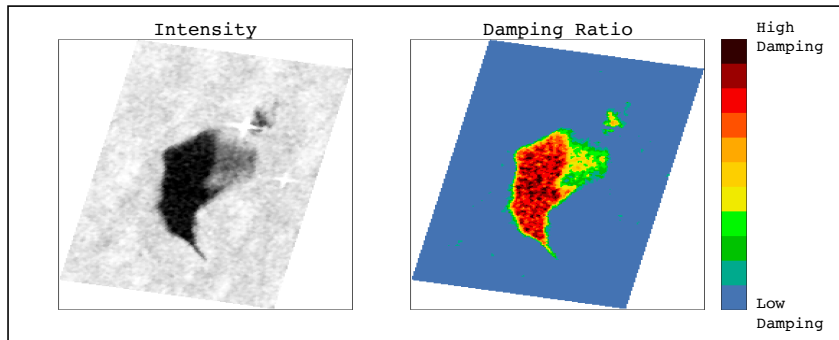
Slick #3
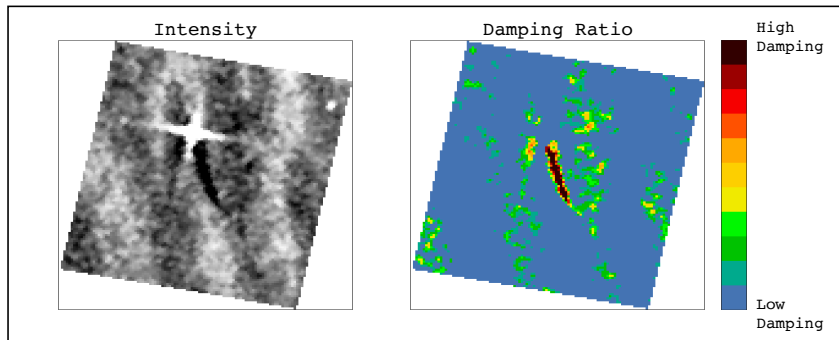
Slick #4
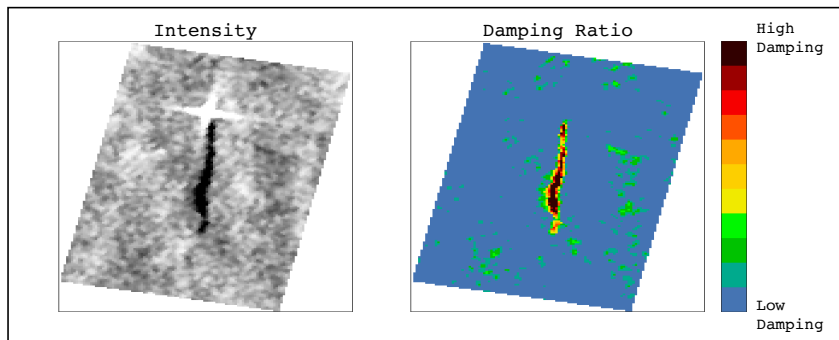
This product is provided as part of an innovation project in collaboration with KSAT.

Page 2

Figure 11.3: Example of one SAR damping ratio report of an archived Sentinel-1 acquisition (page 2).

Figure 11.4: Example of one SAR damping ratio report of an archived Radarsat-2 acquisition.

11.5 Demo during the Oil-On-Water 2019

One of the objectives of the innovation project was to test the work-flow of the algorithm during oil-on-water 2019. Figure 11.5 illustrates the workflow of the demonstration. First,
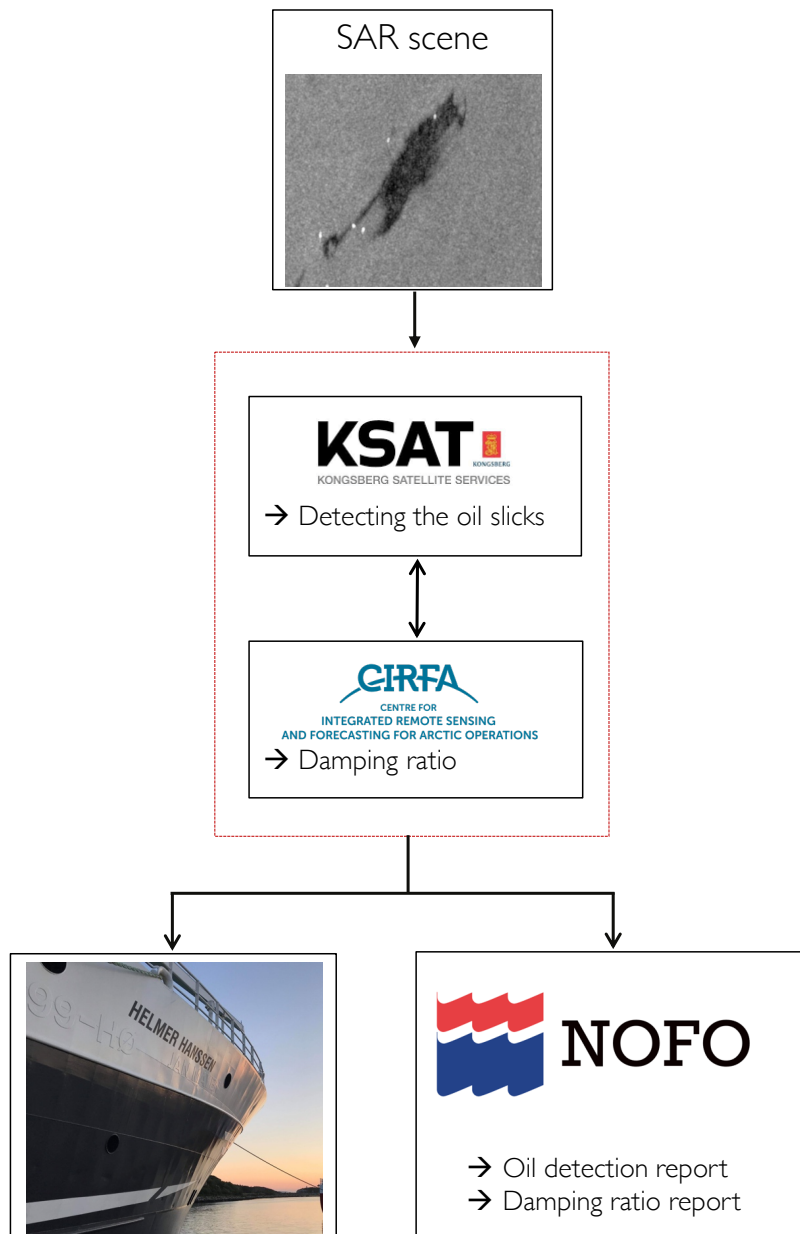
Figure 11.5: Work flow of the product delivery from KSAT to NOFO during the oil-on-water exercise 2019. The lower-left photo was taken by A. Malin Johansson (UiT).

KSAT's operators manually detected potential oil slicks from the SAR images. Following

this, the oil spill detection reports were delivered to the relevant customers. Once the operators were done, the damping ratio algorithm was triggered by files being uploaded to a server. After approximately 2 minutes the damping ratio algorithm had run to completion, and NOFO (responsible for the oil-on-water exercise) could download a Web Map Service (WMS)-layer into their system to inspect the relative damping ratio values within oil slicks in and around the exercise area. FF Helmer Hanssen (the research vessel in the exercise area) also received the product onboard. The damping ratio maps were then loaded into a system that was connected to the drones on-board the ship. The full system could then be used by the drone pilots to navigate the drone to the areas with relatively high damping ratio values within the oil slick. Unfortunately, during the oil-on-water exercise, the drone could not fly close to the SAR acquisition times due to strong winds and high waves. This system was therefore not used, but the damping ratio images were loaded into the system successfully. Additionally, there were some delays to the oil releases, which resulted in young slicks with little spreading in the early SAR acquisitions. Figure 11.6 shows two damping ratio images from Sentinel-1 and TerraSAR-X acquired shortly after the oil release. As observed in the top images of Figure 11.6 the slick is small compared to the spatial resolution of Sentinel-1. The rough sea can also be seen in the bottom images of Figure 11.6, where a clear wave pattern across the scene is visible. As a result of rough sea and a you slick, little internal variation can be seen. Despite the poor weather conditions, the entire workflow of the algorithm and the product delivery was successful.
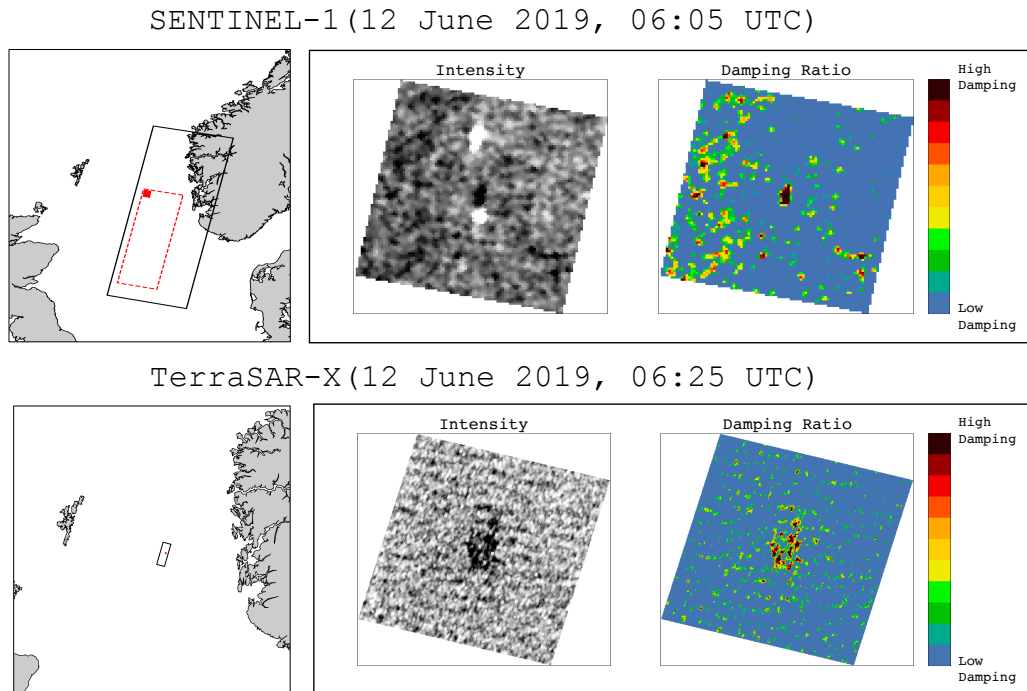
Figure 11.6: Damping ratio images from oil-on-water 2019 from Sentinel-1 and TerraSAR-X. Sentinel-1 from European Space Agency. TerraSAR-X © DLR

11.6   Future Scope

The innovation project is still in its infancy, and more work is necessary to identify the limitations and potential for the damping ratio algorithm. Different oil types must be considered, and preferably, the SAR image should overlap with in-situ measurements and/or optical data to test the relationship between the damping ratio and oil thickness. A more thorough investigation of how many classes to expect within an oil slick should be carried out. Maybe three classes could be sufficient; clean sea (zero damping), thin oil (low-medium damping) and thick actionable oil (high damping).

The minimum spatial resolution needed to capture internal variations through the damping ratio should also be identified. In Norwegian waters, the time difference between Sentinel-1 and Sentinel-2 (also Landsat-8) is long, and a complete overlap in time is impossible with Sentinel-1 and Sentinel-2, not even when using Radarsat-2 or TerraSAR-X. Therefore, optical data from airplanes is optimal. Further work is necessary both for this innovation project and in order to confirm the underlying theory of the damping ratio. It is therefore recommended that the project continue developing and testing of the damping ratio algorithm.

12

Conclusion

The papers presented in Chapter 7-10 cover topics related to the potential of the HP mode for oil spill and sea ice observations, the negative impact of system noise on the polarimetric data, and oil spill response-oriented information products derived from SAR data from an operational perspective. Section 12.1 briefly summarizes the four papers. Section 12.2 discusses and presents some future work and ideas.

12.1 Research Conclusions

FP SAR data for oil spill monitoring has been investigated for years, and several multi-polarization features have been suggested for detection and characterization purposes. The FP SAR comes at a cost of narrow swath width, making it challenging to utilize for operational purposes where coverage is essential. This is the main reason why the HP mode has been suggested as an alternative with more polarimetric information than the conventional DP modes and larger swath width (or finer resolution) than FP SAR. In order to understand the potential and limitations of the HP mode for any application, rigorous testing is necessary. Paper I confirms that the HP mode is almost as good as the FP mode when detecting various types of oil from clean sea under high wind conditions. The two-scale Bragg models are used for grouping the investigated FP and HP features into two categories, either dependent or independent of the small-scale ocean surface roughness. The features dependent on the small-scale ocean surface roughness had highest oil-sea contrast for the investigated oil types for both FP and HP SAR. Paper I recommends the HV- and VV-intensities as the optimal features for separating the various oil types from clean

sea. This recommendation is based on a data set (from the UAVSAR) with very low noise floor. The HV- and VV-intensities are not possible to isolate using the HP mode, and the right-hand circular-circular (RR) and right-hand circular-linear (vertical) intensities are recommended for the HP mode. Paper I also demonstrated the importance of performing an incidence angle correction before segmenting the oil slicks.

FP SAR data has been used to improve the interpretability of various sea ice types compared to SP and the conventional DP modes. Unfortunately, the FP mode comes at a cost of narrow swath width, and since sea ice covers large areas, a wide coverage is preferred. The HP mode therefore has a great potential for sea ice monitoring with increased coverage without losing too much polarimetric information compared to FP SAR. Previous studies have concluded that HP data has a great potential for separating various sea ice types. Most studies have simulated HP data and compared it with FP data, and this was also done in Paper I. Paper IV was amongst the first studies to compare real versus simulated HP data for sea ice. Both real HP and simulated HP showed great potential for separating different sea ice types, such as first-year ice from grease ice and flooded first-year ice. Paper IV confirms that real HP mode is sufficient (for the investigated sea ice types in Paper IV) for sea ice characterization, as previous research has concluded based on the simulation of HP mode. Although Paper IV is based on only three overlapping Radarsat-2 and RISAT-1 SAR scenes, it is a good starting point for validating real HP data for sea ice monitoring.

FP SAR data provides a unique capability of measuring the complete scattering matrix and allow identification and extraction of the scattering processes for a given target. Polarimetry has been used to separate different types of oil and for estimation of physical properties (e.g., volumetric oil fraction) from the oil using physical models. Unfortunately, utilizing polarimetry for oil spill analysis might be risky, since system noise could contaminate the measured signal from these low-backscattering areas. For spaceborne SAR systems the noise floor is high compared to airborne SAR systems, and noise must be carefully considered. Paper II shows the impact of noise on different polarimetric features by identifying trends as a function of both multiplicative and additive system noise and validating against real and simulated noise. The majority of the features show a clear trend with system noise independent of the scene-to-scene variations such as the incidence angle and environmental conditions. Paper II is the first study that includes other noise sources than the known additive system noise, namely multiplicative system noise for oil slicks. The majority of all the satellite SAR signals from oil slicks falls close to or even below the noise floor, when both additive and multiplicative system noise sources are included. This study also recommends avoiding the use of the well known H/α decomposition for oil studies. A noise subtraction should be done before any polarimetric analysis when characterizing the oil. The noise subtraction reduces the oil-sea contrast for some features and should be avoided for oil slick detection purposes.

A single spaceborne SAR scene is valuable when identifying location, extent, and, possibly the source of the spill. Tracking the evolution of a slick requires several images of the

same slick with short time difference between scenes. An oil spill drift model can also track the evolution, but these rely on accurate tuning, model design, and accurate wind and current information. An airborne SAR sensor could provide rapid repeat images to monitor how the slick drifts and weathers on the sea surface. Paper III introduces complementary information products that could be valuable in the recovery process, where timely knowledge of the spill is important. The methodologies presented in Paper III are aimed at creating maps that combine several SAR images to compose products that quantify and visually depict the temporal evolution of the slick in an easily understandable representation.

12.2   Future Outlook

Raney [2007] and Souyris et al. [2005] re-introduced the HP mode as a promising polarization mode that limits the trade-off between coverage and polarimetric information. Simulation of HP data has demonstrated its potential for separating, detecting, and classifying various surfaces. Testing of real HP data became possible with the availability of RISAT-1 data. Unfortunately, RISAT-1 is no longer active, but active satellites such as the RCM and ALOS-2 do offer the HP mode. More extensive testing and verification of the real HP mode should be pursued further when data from these sensors become available.

The damping ratio has been reported to increase with increasing oil thickness (see, e.g., [Gade et al., 1998, Wismann et al., 1998]), which is assumed in Paper III. Further investigations of this should be carried out to validate the relationship between the damping ratio and relative thickness under various environmental conditions and for different oil types. Relative thickness can be extracted from infrared images (see, e.g., [Fingas and Brown, 2014, Fingas and Brown, 2011]). In the visual part of the EM spectrum, the oil thickness can be classified based on its visual appearance on water, known as the Bonn Agreement Oil Appearance Code [BAO, 2017]. One way of investigating the potential of damping ratio is to compare coincident SAR images and optical data (infrared, ultraviolet, and visual). This requires extensive planning since the various instruments need to overlap in time and space. CIRFA participates in the oil-on-water exercises conducted by NOFO almost annually, which is a unique opportunity to collect such a data set. In June 2019, CIRFA together with NOFO and other collaborators collected data from both SAR and various optical instruments. The data set could aid in verifying the potential of the damping ratio and also other parameters alike.

Machine learning are interesting and popular tools when working with SAR data. Several machine learning algorithms, such as support vector machines, naive Bayes, k-means, and Gaussian mixture models, have been investigated for oil slicks and sea ice classifications over the years. More recently, deep learning-based machine learning approaches have also received increased attention for oil slick and ice studies using SAR. Three important areas within the field of oil spill remote sensing are: (1) detection, (2) separating mineral

oil from look-alikes, and (3) extracting physical properties from the oil. There exist many studies on detecting and classifying oil slicks from the surrounding clean sea and look-alikes using machine learning algorithms (see, e.g., [Salberg and Larsen, 2018, Guo et al., 2017, Skrunes et al., 2015, Zhang et al., 2017, Girard-Ardhuin et al., 2005, Tong et al., 2019]). Most studies are based on few SAR images acquired with the same sensor. SAR monitoring of oil slicks at sea is complex, since it depends on several factors such as weather conditions, sensors properties, oil types, and weathering processes. More work is needed on collecting a data set with confirmed oil spills using several sensors, imaging modes, incidence angles, and a wide range of wind conditions in order to fully test whether oil slick detection and characterization could benefit from deep learning or machine learning algorithms. Published studies have already demonstrated some potential using deep learning algorithms in separating look-alikes from mineral oil spills (see, e.g., [Guo et al., 2017]), but can deep learning algorithms be useful to separate low-wind areas from mineral oil slicks using any imaging mode and sensor? With the large number of satellites available and the high frequency of oil spills, it might be possible to obtain a data set suitable for designing a reliable system that could be used operationally. One unexplored territory is using deep learning to estimated physical properties from the SAR data, such as the oil fraction in the oil-sea mixture or oil thickness. Studies (see, e.g., [Boisot et al., 2019, Li et al., 2019, Minchew, 2012]) have estimated the volumetric oil fraction from physical models. Could deep learning methods be more accurate and a more robust tool for such estimation? Additionally, deep learning methods could also be used to find a threshold in SAR images (maybe from the damping ratio) to identify thick (actionable oil) versus thin oil. Using deep learning for these tasks require a good training set with known properties, which is often challenging to collect for oil slicks.

The temporal resolution of spaceborne satellites is poor. A time series of SAR images can be obtained by combining several satellites, but it is challenging to find spaceborne SAR images that cover the same area every hour throughout one day. Oil spill drift modelling could be a useful tool to predict the drift direction and velocity of oil spills. Several interesting studies combining SAR images and oil drift models can be conducted. How can information from SAR improve the oil models? For example, how can SAR images can be used to improve and verify the oil predictions and the oil-covered area from the models? It has been shown that including drifters in the model improved the oil spill prediction. Drifters are not always available on site. Oil slick masks derived from SAR data could be used to initialize the model simulations, which has already been done in some studies (see, e.g., [Jones et al., 2016, Röhrs et al., 2018]). Further work could involve integrating several SAR images with short time difference to improve the initialization of the model. Additionally, since oil slicks have internal variations with regards to thickness, it could be very interesting to integrate this information into oil spill drift models. At last, it has been demonstrated that ocean surface wind can be extracted from SAR. The spreading and drift of oil spills depend strongly on the wind conditions. An interesting study could involve incorporating the SAR wind into the model to improve the predictions.

Over the years, several polarimetric features have been used to describe the scattering

properties of oil slicks. As demonstrated in Paper II, various noise sources significantly impact the scattering properties measured using polarimetry. Some studies have claimed that mineral oil slicks have non-Bragg scattering, but other studies using data from low noise sensors have shown that Bragg scattering is predominant within oil slicks. Paper II quantitatively showed that the non-Bragg scattering is system noise in disguise. Surface scattering is considered the main scattering type for ocean features. Bragg scattering is often used to describe the scattering processes for the ocean and oil slicks, but other scattering processes, in the surface scattering category, could be non-resonant surface scattering within oil slicks and clean sea given the wide range of ocean wave components. Hence, Bragg scattering is not necessarily the complete description of the scattering mechanisms occurring at sea, and a study investigating non-resonant Bragg should be carried out to find an appropriate and more complete model of the ocean and oil backscatter.

Analysis of scattering properties for sea ice has also been done to separate different sea ice types. A similar study to Paper II should be performed to investigate how system noise influences the scattering properties of various sea ice types using polarimetry. Since system noise varies from sensor to sensor and also within imaging modes, it is crucial to understand the impact of different system noise sources to compare be able to across several sensors and imaging modes.

Multi-frequency SAR might contain more physical information about oil slicks and its properties such as thickness than multi-polarization SAR. L-band waves penetrate deeper into the surface compared to X-band waves. Hence, thick oil might be visible in all frequencies, whereas thin oil is better detected with X- and C-band radars [Gade et al., 1998]. Some studies have demonstrated this (see, e.g., [Gade et al., 1998]), but additional studies are encouraged to investigate whether oil slick characterization could benefit from using multi-frequency SAR sensors. In the oil-on-water exercise this summer, CIRFA together with DLR collected simultaneously multi-frequency (X-, S-, and L-band) and FP data from the airborne F-SAR instrument. Current analysis of this data might provide some recommendations on the potential of multi-frequency SAR.

There is often a gap between the industry and academia. CIRFA, which is an SFI with both research and industry partners involved, aims to fill the gap between the two worlds by collaborating and delivering ideas and products that can help the industry. Many industries have a drive towards innovation and want to transfer knowledge from academia to their use cases. The industry often contributes to data collection, which is an important foundation for advances within research. There is a strong connection between CIRFA and the industry partners, but more work is needed to communicate and feed results back to the industry in a form that is understood and appreciated by the industry partners.

A

Separability Measures

Measures of class separability through distance metrics is a useful tool when analyzing various targets in SAR data. There exists several separability metrics that can be used to measure and express the similarities or dissimilarities between two (or more) classes. Separability metrics can be based on the mean and/or variance or probability distributions. Several polarimetric features can be derived from SAR data. Identifying the appropriate separability measure for evaluating the feature's performance in separating/detecting various surfaces will always be a challenge. If the separability measure is unbounded, a comparison across different features becomes difficult. Therefore, bounded separability measures are used in this thesis. The bounded separability measures used in the presented papers are the Jeffries-Matusita (JM) distance (Paper I), the two-sample Kolmogorov–Smirnov (KS) statistical coefficient (Paper IV), and the Spearman's correlation coefficient (Paper IV). These are therefore presented in the upcoming subsections.

A.1   The Jeffries-Matusita Distance

JM distance is often used as a separability criterion for the optimal feature selection and also when evaluating classification results (see, e.g., [Dabboor and Geldsetzer, 2014b, Wang et al., 2018, Wei et al., 2019, Dabboor et al., 2014, Song et al., 2017, Tong et al., 2019]). The JM distance is bounded between $[0, 2]$ and is based on the mean and variance of two classes [Richards and Jia, 2006].

The JM distance between two classes i and j for normally distributed data is defined

as [Richards and Jia, 2006]:

$$JM_{ij} = 2(1 - e^{-d_{ij}}) \qquad (A.1)$$

where d_{ij} is the Bhattacharyya distance defined as:

$$d_{ij} = \frac{1}{8}(\boldsymbol{m}_j - \boldsymbol{m}_i)^T \left[\frac{\Sigma_i + \Sigma_j}{2} \right]^{-1} + \frac{1}{2}\ln\frac{\left[\frac{\Sigma_i + \Sigma_j}{2} \right]}{\sqrt{|\Sigma_i \Sigma_j|}}, \qquad (A.2)$$

where $\boldsymbol{m}_j$ and $\boldsymbol{m}_i$ are the mean values of the two samples, and Σ_j and Σ_i are the covariances (or the standard deviations for one-dimensional case) of the two classes [Richards and Jia, 2006]. This distance measure can only be used for normally distributed data.

All features derived from SAR data are to some extent influenced by the incidence angle. The same incidence angle range should therefore be used when comparing two classes. Figure A.1 illustrates this, where two regions of interests (ROIs) (oil and clean sea) cover the same incidence angle range. Figure A.2 shows the corresponding histograms and the high JM distance (from equation A.1) between the two classes. The one-dimensional case is used in Paper I for oil versus sea separation.

The JM distance with the Bhattacharyya distance as input assumes Gaussian distribution of the input data, which may not always be the case for features derived from SAR data.
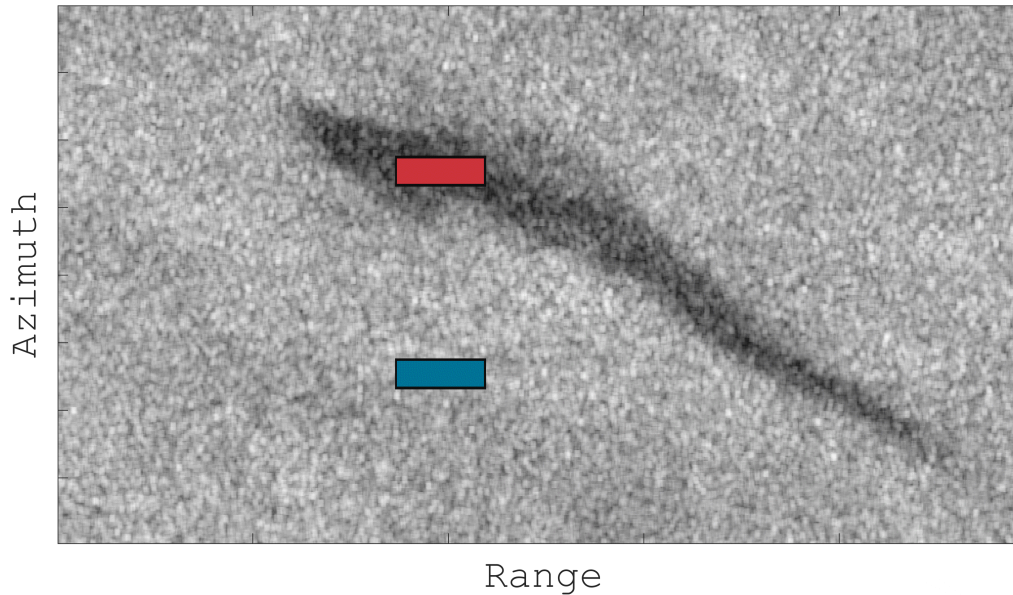

Figure A.1: The VV-intensity (in dB) and region of interests covering the oil slick (red box) and a clean sea area (blue box). Radarsat-2 data and Products © MDA LTD. 2015 - All Rights Reserved.
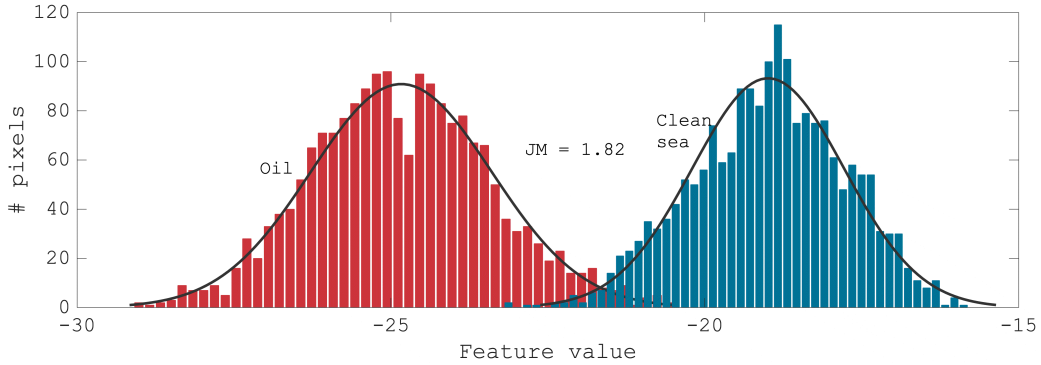
Figure A.2: Histograms of the VV-intensity (in dB) from pixels covering oil and clean sea (see Figure A.1). The Jeffries-Matusita distance between the two classes are also displayed in the plot.

A.2 Two-sample Kolmogorov–Smirnov Test

The two-sample KS test determines whether or not there is a statistically significant difference between two classes. The KS test is a non-parametric or distribution-free test [Massey, 1951], where the null hypothesis is that two classes are drawn from the same population distribution. The KS test outputs the KS statistic, which is used as a separability measure. The KS test is most sensitive around the median value and less sensitive at the extremes of the sample cumulative distribution functions (CDF) [Casey et al., 2016]. The KS test is therefore useful for identifying shifts in the probability distribution functions between two classes [Press et al., 2007].

The sample CDF is estimated from the probability density function, and since we are dealing with discrete random variables the sample cumulative distribution functions ($F_X(x)$) are estimated with a sum, i.e., [Stark and Woods, 2011]

$$F_X(x) = P(X \leq x) = \sum_{x_i \leq x} P(X = x_i) = \sum_{x_i \leq x} f(x_i), \tag{A.3}$$

where $P(X \leq x)$ represents the probability that the random variable X has a value less than or equal to x, and $f(x_i)$ is the probability density function (pdf). The two-sample KS test inputs two sample CDFs and test whenever their statistical distribution are the same (the null hypothesis is accepted), and is based on the maximum distance between the two sample CDFs ($F_{X_1}(x)$ and $F_{X_2}(x)$) [Press et al., 2007], i.e.,:

$$KS = \max\left(F_{X_1}(x) - F_{X_2}(x)\right). \tag{A.4}$$

The KS statistic is only used in Paper IV, and the top panel of Figure A.3 shows the VV-intensity image from Radarsat-2 with two regions of interest of grease/frazil ice and first

year ice (see Paper IV for more detailed descriptions of these sea ice types). The bottom panel of Figure A.3 shows their corresponding histograms, the CDFs, and the KS statistics between the two CDFs. The KS statistics, bounded between $[0, 1]$, are used to estimate the p-value. The p-value is the evidence against a null hypothesis. If the p-value is less than the significance level (for example 5%), then the null hypothesis is rejected. If the KS statistics is close to 1, then the two samples are considered different (their underlying distributions are different), whereas a value close to 0 indicates equal distribution and acceptance of the null hypothesis.

The two-sample KS takes the sample CDFs as input, whereas the JM distance uses the mean and variance of two classes as input. These measures are based on the similarity between two classes based on their statistical properties. However, to investigate the correlation and the degree of association between two classes, the Spearman and Pearson correlation coefficients are useful. The Spearman correlation coefficient (used in Paper IV) is discussed in the upcoming section.

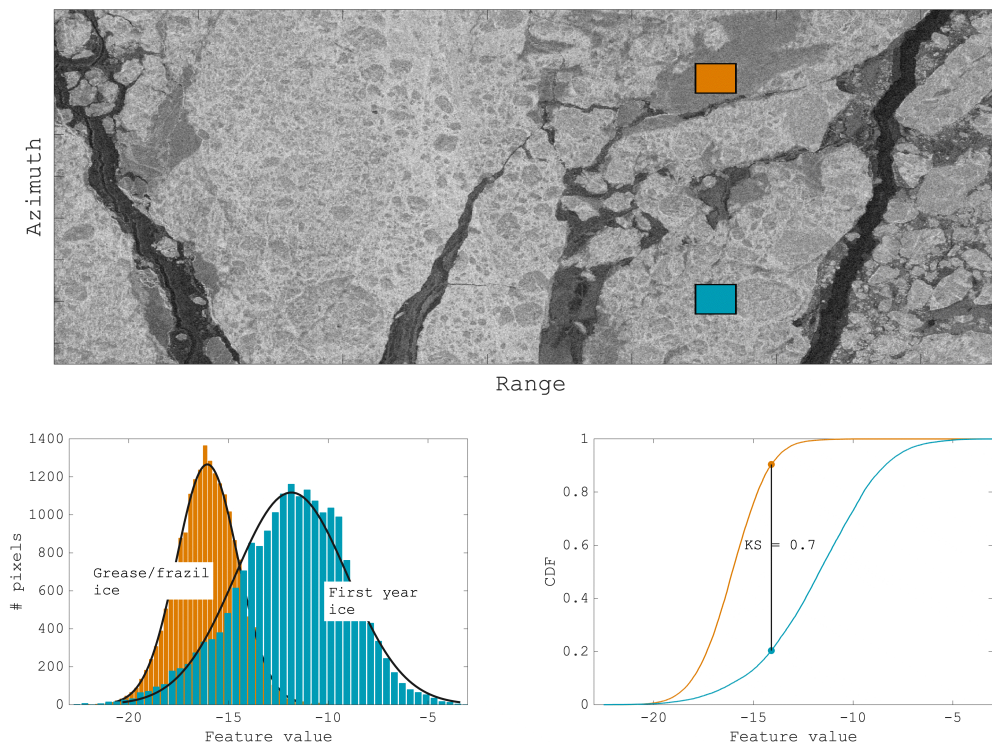**Figure A.3:** Top: The VV-intensity (in dB) and region of interests covering grease/frazil ice (red box) and a first year ice (orange box). Radarsat-2 data and Products $^{©}$ MDA LTD. 2015 - All Rights Reserved. Bottom: Histograms (left panel) and CDF (right panel) of the VV-intensity (in dB) from pixels covering grease/frazil ice and first year ice. The two-sample KS statistic between the two classes is displayed in the right panel.

A.3 The Spearman Correlation Coefficient

The Spearman correlation coefficient considers the degree of association between two variables (X and Y) of the same size, and the parametric equivalent is the Pearson product-moment correlation [Corder and Foreman, 2009]. The Spearman correlation coefficient is defined as [Corder and Foreman, 2009]:

$$\rho_S = 1 - \frac{6\sum_i^N d_R^2}{n(n^2-1)} \tag{A.5}$$

where d_R is the difference between ranked pairs (rg(X)-rg(Y)) and n is number of data points [Corder and Foreman, 2009]. A vector is constructed by sorting the values in ascending order, and the rank corresponds to the value's position in the vector. If any values in the vector are tied then the rank is based on their average rank, named tied rank. For example, if $X = [1, 3, 4, 1, 3]$, then the ranked vector is $[1, 3, 5, 2, 4]$, and the tied rank vector is $rg(X) = [1.5, 3.5, 5, 1.5, 3.5]$.

If the Spearman correlation coefficient is close to 1 or −1 then the two variables have a nearly perfect positive or negative relationship, whereas a correlation close to 0 indicates a week or trivial relationship [Corder and Foreman, 2009]. The benefit of using Spearman's instead of Pearson's correlation coefficient is that the Spearman correlation coefficient is less sensitive to outliers. Figure A.4 shows an example of two scatter plots of the regions displayed in Figure A.3, where the Spearman correlation coefficients are calculated between two features (VV-intensity and the copolarization ratio (HH/VV)). The left panel shows a strong correlation, whereas the right panel shows none/trivial relationship between the two features [Corder and Foreman, 2009].

The Spearman correlation coefficient [Spearman, 1904] (also known as the Spearman rank correlation) is used in Paper IV to evaluate the correlation between features derived from Radarsat-2 and RISAT-1 overlaps.
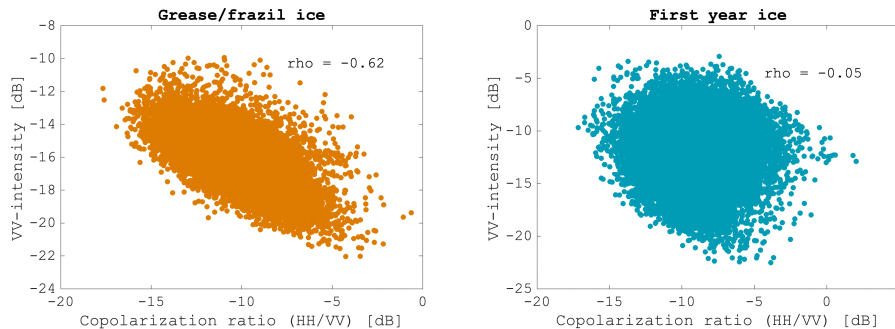

Figure A.4: Scatter plots of two sea ice regions (Grease/frazil ice and first year ice) shown in Figure A.3 with their corresponding Spearman correlation coefficients between two features (VV-intensity and the copolarization ratio).

Bibliography

[BAO, 2017] (2017). Bonn Agreement Oil Appearance Code. Bonn Agreement Aerial Operations Handbook, version 2017. (`www.bonnagreement.org/publications`, last accessed 1 September 2019).

[Ainsworth et al., 2006] Ainsworth, T. L., Ferro-Famil, L., and Lee, J.-S. (2006). Orientation angle preserving a posteriori polarimetric SAR calibration. *IEEE Trans. Geosci. Remote Sens.*, 44(4):994–1003.

[Alpers et al., 2017] Alpers, W., Holt, B., and Zeng, K. (2017). Oil spill detection by imaging radars: Challenges and pitfalls. *Remote Sens. Environ.*, 201:133–147.

[Alpers and Hühnerfuss, 1989] Alpers, W. and Hühnerfuss, H. (1989). The damping of ocean waves by surface films: A new look at an old problem. *J. Geophys. Res.*, 94(C5):6251–6265.

[Androulidakis et al., 2018] Androulidakis, Y., Kourafalou, V., Özgökmen, T., Garcia-Pineda, O., Lund, B., Hénaff, M. L., Hu, C., Haus, B. K., Novelli, G., Guigand, C., Kang, H., Hole, L., and Horstmann, J. (2018). Influence of River-Induced Fronts on Hydrocarbon Transport: A Multiplatform Observational Study. *J. Geophys. Res. Oceans*, 123(5):3259–3285.

[Angelliaume et al., 2018] Angelliaume, S., Dubois-Fernandez, P. C., Jones, C. E., Holt, B., Minchew, B., Amri, E., and Miegebielle, V. (2018). SAR imagery for detecting sea surface slicks: Performance assessment of polarization-dependent parameters. *IEEE Trans. Geosci. Remote Sens.*, 56(8):1–21.

[Asl et al., 2016] Asl, S. D., Amos, J., Woods, P., Garcia-Pineda, O., and MacDonald, I. R. (2016). Chronic, anthropogenic hydrocarbon discharges in the gulf of mexico. *Deep Sea Research Part II: Topical Studies in Oceanography*, 129:187 – 195. The Gulf of Mexico Ecosystem - before, during and after the Macondo Blowout.

[Atteia and Collins, 2013] Atteia, G. and Collins, M. J. (2013). On the use of Compact Polarimetry SAR for Ship Detection. *ISPRS Journal of Photogrammetry and Remote Sensing*, 80:1–9.

[Boisot et al., 2019] Boisot, O., Angelliaume, S., and Guérin, C. (2019). Marine Oil Slicks Quantification From L-band Dual-Polarization SAR Imagery. *IEEE Trans. Geosci. Remote Sens.*, 57(4):2187–2197.

[Brekke et al., 2014] Brekke, C., Holt, B., Jones, C. E., and Skrunes, S. (2014). Discrimination of oil spills from newly formed sea ice by synthetic aperture radar. *Remote Sens. Environ.*, 145:1–14.

[Brekke et al., 2017] Brekke, C., Skrunes, S., and Espeseth, M. M. (2017). Oil spill dispersion in full-polarimetric and hybrid-polarity SAR. In *IEEE Int. Geosci. Remote Sens. Symp. (IGARSS) Proceedings*, pages 1020–1023.

[Brekke and Solberg, 2005] Brekke, C. and Solberg, A. H. S. (2005). Oil Spill Detection by Satellite Remote Sensing. *Remote Sens. Environ.*, 95(1):1–13.

[Buono et al., 2019] Buono, A., Nunziata, F., de Macedo, C. R., Velotto, D., and Migliaccio, M. (2019). A Sensitivity Analysis of the Standard Deviation of the Copolarized Phase Difference for Sea Oil Slick Observation. *IEEE Trans. Geosci. Remote Sens.*, 57(4):2022–2030.

[Buono et al., 2016a] Buono, A., Nunziata, F., and Migliaccio, M. (2016a). Analysis of Full and Compact Polarimetric SAR Features Over the Sea Surface. *IEEE Geosci. Remote Sens. Lett.*, 13(10):1527–1531.

[Buono et al., 2016b] Buono, A., Nunziata, F., Migliaccio, M., and Li, X. (2016b). Polarimetric analysis of compact-polarimetry SAR architectures for sea oil slick observation. *IEEE Trans. Geosci. Remote Sens.*, 54(10):5862–5874.

[Canadian Space Agency, nd] Canadian Space Agency (n.d.). `http://www.asc-csa.gc.ca/eng/satellites/radarsat2/Default.asp` (last accessed 1 April 2019).

[Casey et al., 2016] Casey, J. A., Howell, S. E., Tivy, A., and Haas, C. (2016). Separability of sea ice types from wide swath C- and L-band synthetic aperture radar imagery acquired during the melt season. *Remote Sens. Environ.*, 174:314 – 328.

[Chuvieco and Huete, 2010] Chuvieco, E. and Huete, A. (2010). *Fundamentals of Satellite Remote Sensing*. CRC Press Taylor and Francis Group.

[Clemente-Colón and Yan, 2000] Clemente-Colón, P. and Yan, X.-H. (2000). Low-Backscatter Ocean Features in Synthetic Aperture Radar Imagery. *JOHNS HOPKINS APL TECHNICAL DIGEST*, 21(1):112–123.

[Cloude, 2010] Cloude, S. R. (2010). *Polarisation Applications in Remote Sensing. First edition*. Oxford University Press Inc., New York, pp. 125-129.

[Cloude et al., 2012] Cloude, S. R., Goodenough, D., and Chen, H. (2012). Compact Decomposition Theory. *IEEE Trans. Geosci. Remote Sens.*, 9(1):28–32.

[Coleman, 2003] Coleman, J. (2003). *Oil in the Sea III*. National Academy Press, Washington DC, USA.

[Collins et al., 2013] Collins, M. J., Denbina, M., and Atteia, G. (2013). On the Reconstruction of Quad-Pol SAR Data From Compact Polarimetry Data For Ocean Target Detection. *IEEE Trans. Geosci. Remote Sens.*, 51(1):591–600.

[Corder and Foreman, 2009] Corder, G. W. and Foreman, D. I. (2009). *Nonparametric Statistics for Non-Statisticians: A Step-by-Step Approach*. John Wiley & Sons.

[Cumming and Wong, 2005] Cumming, I. G. and Wong, F. H. (2005). *Digital Processing of Synthetic Aperture Radar data*. Artech House.

[Curlander and McDonough, 1991] Curlander, J. C. and McDonough, R. N. (1991). *Synthetic Aperture Radar, Systems & Signal Processing*. John Wiley & Sons, INC., Wiley Series in Remote Sensing.

[Dabboor and Geldsetzer, 2014a] Dabboor, M. and Geldsetzer, T. (2014a). On the Classification of Sea Ice Types using Simulated Radarsat Constellation Mission (RCM) Compact Polarimetric SAR Parameters. *ASPRS 2014 Annual Conference, Louisville, Kentucky*.

[Dabboor and Geldsetzer, 2014b] Dabboor, M. and Geldsetzer, T. (2014b). Towards sea ice classification using simulated RADARSAT Constellation Mission compact polarimetric SAR imagery. *Remote Sens. Environ.*, 140:189–195.

[Dabboor et al., 2014] Dabboor, M., Howell, S., Shokr, M., and Yackel, J. (2014). The Jeffries-Matusita distance for the case of complex Wishart distribution as a separability criterion for fully polarimetric SAR data. *Int. J. Remote Sens.*, 35(19):6859–6873.

[Denbina, 2014] Denbina, M. (2014). Iceberg Detection Using Polarimetric Synthetic Aperture Radar. *P.h.D. Dissertation, University of Calgary*.

[Dierking and Busche, 2006] Dierking, W. and Busche, T. (2006). Sea ice monitoring by L-band SAR: an assessment based on literature and comparisons of JERS-1 and ERS-1 imagery. *IEEE Trans. Geosci. Remote Sens.*, 44(4):957–970.

[Dierking et al., 2003] Dierking, W., Skriver, H., and Gudmandsen, P. (2003). SAR polarimetry for sea ice classification. *Proceedings of the Workshop on POLinSAR - Applications of SAR Polarimetry and Polarimetric Interferometry (ESA SP-529). 14-16 January 2003, Frascati, Italy*.

[Elachi and van Zyl, 2006] Elachi, C. and van Zyl, J. (2006). *Introduction to the Physics and Techniques of Remote Sensing*. John Wiley and Sons, Inc., Publication, second edition.

[Eriksson et al., 2010] Eriksson, L. E. B., Borenäs, K., Dierking, W., Berg, A., Santoro, M., Pemberton, P., Lindh, H., and Karlson, B. (2010). Evaluation of new spaceborne SAR sensors for sea-ice monitoring in the Baltic Sea. *Can. J. Remote Sens.*, 36(1):56–73.

[Espeseth et al., 2016] Espeseth, M. M., Brekke, C., and Anfinsen, S. N. (2016). Hybrid-polarity and reconstruction methods for sea ice with L- and C-band SAR. *IEEE Geosci. Remote Sens. Lett.*, 13(3):467–471.

[Espeseth et al., 2017] Espeseth, M. M., Skrunes, S., Jones, C. E., Brekke, C., Holt, B., and Doulgeris, A. P. (2017). Analysis of evolving oil spills in full-polarimetric and hybrid-polarity SAR. *IEEE Trans. Geosci. Remote Sens.*, 55(7):4190–4210.

[Ferraro et al., 2010] Ferraro, G., Baschek, B., de Montpellier, G., Njoten, O., Perkovic, M., and Vespe, M. (2010). On the SAR derived alert in the detection of oil spills according to the analysis of the EGEMP. *Mar. Pollut. Bull.*, 60(1):91 – 102.

[Fingas, 2011] Fingas, M. (2011). Introduction to oil chemistry and properties. *Oil Spill Science and Technology*.

[Fingas and Brown, 2014] Fingas, M. and Brown, C. (2014). Review of oil spill remote sensing. *Mar. Pollut. Bull.*, 83(1):9 – 23.

[Fingas and Brown, 2011] Fingas, M. and Brown, C. E. (2011). Chapter 6 - oil spill remote sensing: A review. In Fingas, M., editor, *Oil Spill Science and Technology*, pages 111 – 169. Gulf Professional Publishing, Boston.

[Fingas and Brown, 1997] Fingas, M. F. and Brown, C. E. (1997). Review of oil spill remote sensing. *Spill Science & Technology Bulletin*, 4(4):199 – 208. The Second International Symposium on Oil Spills.

[Fore et al., 2015] Fore, A. G., Chapman, B. D., Hawkins, B. P., Hensley, S., Jones, C. E., Michel, T. R., and Muellerschoen, R. J. (2015). UAVSAR Polarimetric Calibration. *IEEE Trans. Geosci. Remote Sens.*, 53(6):3481–3491.

[Freeman et al., 1992] Freeman, A., van Zyl, J. J., Klein, J. D., Zebker, H. A., and Shen, Y. (1992). Calibration of Stokes and scattering matrix format polarimetric SAR data. *IEEE Trans. Geosci. Remote Sens.*, 30(3):531–539.

[Fritz and Eineder, 2010] Fritz, T. and Eineder, M. (2010). TerraSAR-X ground segment basic product specification document.

[Gade et al., 1998] Gade, M., Alpers, W., Hühnerfuss, H., Masuko, H., and Kobayashi, T. (1998). Imaging of biogenic and anthropogenic ocean surface films by the multifrequency/multipolarization SIR-C/X-SAR. *J. Geophys. Res.*, 103(C9):18851–18866.

[Geldsetzer et al., 2015] Geldsetzer, T., Arkett, M., Zagon, T., Charbonneau, F., Yackel, J. J., and Scharien, T. K. (2015). All-season compact-polarimetry C-band SAR observations of sea ice. *Can. J. Remote Sens.*, 41(5):485–504.

[Gill et al., 2015] Gill, J. P. S., Geldsetzer, T., and Fuller, M. C. (2015). Sensitivity of C-band synthetic aperture radar polarimetric parameters to snow thickness over landfast smooth first-year sea ice. *Remote Sens. Environ.*, 166:34 – 49.

[Girard-Ardhuin et al., 2005] Girard-Ardhuin, F., Mercier, G., Collard, F., and Garello, R. (2005). Operational oil-slick characterization by SAR imagery and synergistic data. *IEEE J. Ocean. Eng.*, 30(3):487–495.

[Guo et al., 2017] Guo, H., Wu, D., and An, J. (2017). Discrimination of Oil Slicks and Lookalikes in Polarimetric SAR Images Using CNN. *Sensors*, 17(8).

[Hajnsek et al., 2009] Hajnsek, I., Jagdhuber, T., Schon, H., and Papathanassiou, K. P. (2009). Potential of Estimating Soil Moisture Under Vegetation Cover by Means of PolSAR. *IEEE Trans. Geosci. Remote Sens.*, 47(2):442–454.

[Hajnsek et al., 2003] Hajnsek, I., Pottier, E., and Cloude, S. R. (2003). Inversion of surface parameters from polarimetric SAR. *IEEE Trans. Geosci. Remote Sens.*, 41(4):727–744.

[Hensley et al., 2014] Hensley, S., Oveisgharan, S., Saatchi, S., Simard, M., Ahmed, R., and Haddad, Z. (2014). An error model for biomass estimates derived from polarimetric radar backscatter. *IEEE Trans. Geosci. Remote Sens.*, 52(7):4065–4082.

[Herbst et al., 2016] Herbst, L., DeCola, E., and Kennedy, K. (2016). New pathways for developing and testing oil spill response equipment in real world conditions. *OCEANS 2016 MTS/IEEE Monterey*, pages 1–6.

[Hollinger and Mennella, 1973] Hollinger, J. P. and Mennella, R. A. (1973). Oil spills: Measurements of their distributions and volumes by multifrequency microwave radiometry. *Science*, 181(4094):54–56.

[Holt, 2004] Holt, B. (2004). Chapter 2: SAR imaging of the ocean surface. *Synthetic Aperture Radar Marine User's Manual (NOAA/NESDIS), C.R. Jackson and J. R. Apel*, (25-80).

[Hühnerfuss, 2006] Hühnerfuss, H. (2006). Basic physicochemical principles of monomolecular sea slicks and crude oil spills. *Gade M., Hühnerfuss H., Korenowski*

G.M. (eds) Marine Surface Films. Springer, Berlin, Heidelberg, pages 21–35.

[Huynen, 1970] Huynen, J. R. (1970). Phenomenological theory of radar targets. *Ph.D. dissertation, Rotterdam: Drukkerij Bronder-Offset N.V.,*.

[Iodice et al., 2011] Iodice, A., Natale, A., and Riccio, D. (2011). Retrieval of soil surface parameters via a polarimetric two-scale model. *IEEE Trans. Geosci. Remote Sens.*, 49(7):2531–2547.

[ITOPF, 2002] ITOPF (2002). Fate of marine oil spills. *The International Tanker Owners Pollution Federation Limited, Technical report*.

[Jenkins and Jacobs, 1997] Jenkins, A. D. and Jacobs, S. J. (1997). Wave damping by a thin layer of viscous fluid. *Physics of Fluids*, 9(5):1256–1264.

[Jensen, 2000] Jensen, J. R. (2000). *Remote Sensing of the Environment, An Earth Resource Perspective*. Pearson, Prentice Hall.

[Johansson et al., 2017] Johansson, A. M., King, J. A., Doulgeris, A. P., Gerland, S., Singha, S., Spreen, G., and Busche, T. (2017). Combined observations of Arctic sea ice with near-coincident colocated X-band, C-band, and L-band SAR satellite remote sensing and helicopter-borne measurements. *J. Geophys. Res. Oceans*, 122(1):669–691.

[Jones et al., 2016] Jones, C. E., Dagestad, K.-F., Breivik, Ø., Holt, B., Röhrs, J., Christensen, K. H., Espeseth, M., Brekke, C., and Skrunes, S. (2016). Measurement and Modeling of Oil Slick Transport. *J. Geophys. Res.: Oceans*, 121(10):7759–7775.

[Jones et al., 2018] Jones, C. E., Espeseth, M. M., Holt, B., and Brekke, C. (2018). Measurement of oil slick transport and evolution in the gulf of mexico using L-band Synthetic Aperture Radar. *12th European Conference on Synthetic Aperture Radar (EUSAR)*.

[Jones and Holt, 2018] Jones, C. E. and Holt, B. (2018). Experimental L-band airborne SAR for oil spill response at sea and in coastal waters. *Sensors*, 18(2).

[Kennaugh, 1952] Kennaugh, E. M. (1952). Effects of type of polarization on echo characteristics. *The Ohio State University, Antennas Laboratory, Columbus, OH, Reports 381-1 to 394-24, 1949-1954 and Report 389-12 (M.Sc.thesis)*.

[Lee and Pottier, 2009] Lee, J.-S. and Pottier, E. (2009). *Polarimetric Radar Imaging: from basic to applications*. Optical Science and Engineering. CRC Press Taylor and Francis Group.

[Lee et al., 2000] Lee, J.-S., Schuler, D. L., and Ainsworth, T. L. (2000). Polarimetric SAR Data Compensation for Terrain Azimuth Slope Variation. *IEEE Trans. Geosci. Remote*

Sens., 38(5):2153–2163.

[Li and Perrie, 2016] Li, H. and Perrie, W. (2016). Sea Ice Characterization and Classification Using Hybrid Polarimetry SAR. *IEEE J. Sel. Topics Appl. Earth Observ. Remote Sens.*, 9(11):4998–5010.

[Li et al., 2019] Li, H., Perrie, W., and Wu, J. (2019). Retrieval of oil–water mixture ratio at ocean surface using compact polarimetry Synthetic Aperture Radar. *Remote Sens.*, 11(7).

[Li et al., 2016] Li, H., Perrie, W., Zhou, Y., and He, Y. (2016). Oil spill detection on the ocean surface using hybrid polarimetric SAR imagery. *Science China*, 59(2):249–257.

[Massey, 1951] Massey, J. F. J. (1951). The kolmogorov-smirnov test for goodness of fit. *Taylor & Francis, Ltd. on behalf of the Journal of the American Statistical Association*, 46(253):68–78.

[MDA, 2018] MDA (2018). Radarsat-2 product description. *MacDonald, Dettwiler and Associates Ltd., Rickmond, BC, USA, RN-SP-52-1238,Issue 1/14.*

[Migliaccio et al., 2009a] Migliaccio, M., Gambardella, A., Nunziata, F., Shimada, M., and Isoguchi, O. (2009a). The PALSAR polarimetric mode for sea oil slick observation. *IEEE Trans. Geosci. Remote Sens.*, 47(12):4032 – 4041.

[Migliaccio et al., 2009b] Migliaccio, M., Nunziata, F., and Gambardella, A. (2009b). On the co-polarized phase difference for oil spill observation. *Int. J. Remote Sens.*, 30(6):1589–1602.

[Migliaccio et al., 2005] Migliaccio, M., Tranfaglia, M., and Ermakov, S. A. (2005). A Physical Approach for the Observation of Oil Spills in SAR images. *IEEE J. Ocean. Eng.*, 30(3):496–507.

[Minchew, 2012] Minchew, B. (2012). Determining the mixing of oil and sea water using polarimetric synthetic aperture radar. *Geophys. Res. Lett.*, 39(16).

[Minchew et al., 2012] Minchew, B., Jones, C. E., and Holt, B. (2012). Polarimetric Analysis of Backscatter From the Deepwater Horizon Oil Spill Using L-Band Synthetic Aperture Radar. *IEEE Trans. Geosci. Remote Sens.*, 50(10):3812–3830.

[Misra et al., 2013] Misra, T., Rana, S. S., Desai, N. M., Dave, D. B., Rajeevjyoti, Arora, R. K., Rao, C. V. N., Bakori, B. V., Neelakantan, R., and Vachchani, J. G. (2013). Synthetic Aperture Radar payload on-board RISAT-1: configuration, technology and performance. *Current science*, 104(4).

[Moen et al., 2015] Moen, M.-A. N., Anfinsen, S. N., Doulgeris, A. P., Renner, A. H. H., and Gerland, S. (2015). Assessing polarimetric SAR sea-ice classifications using consecutive day images. *Annals of Glaciology*, 56(69):285–294.

[NOAA, nd] NOAA (n.d.). National Oceanic and Atmospheric Administration (NOAA): What is an oil seep? (`https://oceanservice.noaa.gov/facts/oilseep.html`, last accessed 4 September 2019).

[NOFO, nd] NOFO (n.d.). The Norwegian Clean Seas Association for Operating Companies (`https://www.nofo.no`, last accessed 18 June 2019).

[Nunziata et al., 2019] Nunziata, F., de Macedo, C. R., Buono, A., Velotto, D., and Migliaccio, M. (2019). On the analysis of a time series of X–band TerraSAR–X SAR imagery over oil seepages. *Int. J. Remote Sens.*, 40(9):3623–3646.

[Nunziata et al., 2013] Nunziata, F., Gambardella, A., and Migliaccio, M. (2013). On the degree of polarization for SAR sea oil slick observation. *ISPRS Journal of Photogrammetry and Remote Sensing*, 78:41 – 49.

[Nunziata et al., 2015] Nunziata, F., Migliaccio, M., and Li, X. (2015). Sea Oil Slick Observaion Using Hybrid-Polarity SAR Architecture. *IEEE J. Ocean. Eng.*, 40(2):426–440.

[Onstott and Shuchman, 2004] Onstott, R. G. and Shuchman, R. A. (2004). Chapter 3. SAR Measurements of Sea Ice. *Synthetic Aperture Radar Marine User's Manual (NOAA/NESDIS), C.R. Jackson and J. R. Apel*, `http://www.SARusersmanual.com/`, last accessed 24 May 2019.

[Panigraphi and Mishra, 2012] Panigraphi, R. and Mishra, A. (2012). Comparison of hybrid-pol with quad-pol scheme based on polarimetric information content. *International Journal of Remote Sensing*, 33(11):3531–3541.

[Pinel et al., 2014] Pinel, N., Bourlier, C., and Sergievskaya, I. (2014). Two-dimensional radar backscattering modeling of oil slicks at sea based on the model of local balance: Validation of two asymptotic techniques for thick films. *IEEE Trans. Geosci. Remote Sens.*, 52(5):2326–2338.

[Press et al., 2007] Press, W. H., Teukolsky, S. A., Vetterling, W. T., and Flannery, B. P. (2007). *Numerical recipes : the art of scientific computing*. Cambridge University Press, New York, NY, USA.

[Quegan, 1994] Quegan, S. (1994). A unified algorithm for phase and cross-talk calibration of polarimetric data-theory and observations. *IEEE Trans. Geosci. Remote Sens.*, 32(1):89–99.

[Raney et al., 2012] Raney, K., Cahill, J. T. S., Patterson, G. W., and Bussey, D. B. J. (2012). The m-chi Decomposition of Hybrid Dual-Polarimetric Radar Data with Application to Lunar Craters. *J. Geophys. Res. Planets*, 117(E12).

[Raney, 2007] Raney, R. K. (2007). Hybrid-Polarity SAR Architecture. *IEEE Trans. Geosci. Remote Sens.*, 45(11):3397–3404.

[Richards and Jia, 2006] Richards, J. A. and Jia, X. (2006). *Remote Sensing Digital Image Analysis. An Introduction. Fourth Edition*. Springer-Verlag Berlin Heidelberg.

[Röhrs et al., 2018] Röhrs, J., Dagestad, K.-F., Asbjørnsen, H., Nordam, T., Skancke, J., Jones, C. E., and Brekke, C. (2018). The effect of vertical mixing on the horizontal drift of oil spills. *Ocean Science*, 14(6):1581–1601.

[Sabry and Vachon, 2014] Sabry, R. and Vachon, P. W. (2014). A Unified Framework for general Compact and Quad Polarimetric SAR Data and Imagery Analysis. *IEEE Trans. Geosci. Remote Sens.*, 52(1):582–602.

[Salberg and Larsen, 2018] Salberg, A. and Larsen, S. O. (2018). Classification of ocean surface slicks in simulated hybrid-polarimetric SAR data. *IEEE Trans. Geosci. Remote Sens.*, 56(12):7062–7073.

[Salberg et al., 2014] Salberg, A.-B., Rudjord, O., and Solberg, A. H. S. (2014). Oil spill detection in hybrid-polarimetric SAR images. *IEEE Trans. Geosci. Remote Sens.*, 52(10):6521–6533.

[Schwartzberg, 1971] Schwartzberg, H. G. (1971). The movement of oil spills. *International Oil Spill Conference Proceedings*, 1971(1):489–494.

[Sergievskaya et al., 2019] Sergievskaya, I., Ermakov, S., Lazareva, T., and Guo, J. (2019). Damping of surface waves due to crude oil/oil emulsion films on water. *Mar. Pollut. Bull.*, 146:206 – 214.

[Shirvany et al., 2012] Shirvany, R., Chabert, M., and Tourneret, J.-Y. (2012). Ship and Oil-Spill Detection using the Degree of Polarization in Linear and Hybrid/Compact Dual-Pol SAR. *IEEE J. Sel. Topics Appl. Earth Observ. Remote Sens.*, 5(3).

[Shokr and Sinha, 1985] Shokr, M. and Sinha, N. (1985). *Methods of Satellite Oceanography*. University of California.

[Singh et al., 1986] Singh, K. P., Gray, A. L., Hawkins, R. K., and O'Neil, R. A. (1986). The Influence of Surface Oil on C-and Ku-Band Ocean Backscatter. *IEEE Trans. Geosci. Remote Sens.*, GE-24(5):738 – 744.

[Singha et al., 2013] Singha, S., Bellerby, T. J., and Trieschmann, O. (2013). Satellite oil spill detection using artificial neural networks. *IEEE J. Sel. Topics Appl. Earth Observ. Remote Sens.*, 6(6):2355–2363.

[Singha et al., 2018] Singha, S., Johansson, M., Hughes, N., Hvidegaard, S. M., and Skourup, H. (2018). Arctic sea ice characterization using spaceborne fully polarimetric L-, C-, and X-band SAR with validation by airborne measurements. *IEEE Trans. Geosci. Remote Sens.*, 56(7):3715–3734.

[Singha et al., 2016] Singha, S., Ressel, R., Velotto, D., and Lehner, S. (2016). A combination of traditional and polarimetric features for oil spill detection using TerraSAR-X. *IEEE J. Sel. Topics Appl. Earth Observ. Remote Sens.*, 9(11):4979–4990.

[Skrunes, 2014] Skrunes, S. (2014). Characterization of Low Backscatter Regions in the Marine Environment by Multipolarization C- and X-band Synthetic Aperture Radar Data. *PhD thesis, Faculty of Science and Technology, Department of Physics and Technology, UiT The Arctic University of Norway*.

[Skrunes et al., 2014] Skrunes, S., Brekke, C., and Eltoft, T. (2014). Characterization of Marine Surface Slicks by Radarsat-2 Multipolarization Features. *IEEE Trans. Geosci. Remote Sens.*, 52(9):5302–5319.

[Skrunes et al., 2015] Skrunes, S., Brekke, C., Eltoft, T., and Kudryavtsev, V. (2015). Comparing near-coincident C- and X-band SAR acquisitions of marine oil spill. *IEEE Trans. Geosci. Remote Sens.*, 53(4):1958 – 1975.

[Skrunes et al., 2017] Skrunes, S., Brekke, C., and Espeseth, M. M. (2017). Assessment of the RISAT-1 FRS-2 mode for oil spill observation. *IEEE Int. Geosci. Remote Sens. Symp. (IGARSS) Proceedings*, pages 1024–1027.

[Skrunes et al., 2018] Skrunes, S., Brekke, C., Jones, C. E., Espeseth, M. M., and Holt, B. (2018). Effect of wind direction and incidence angle on polarimetric SAR observations of slicked and unslicked sea surfaces. *Remote Sens. Environ.*, 213:73 – 91.

[Skrunes et al., 2016] Skrunes, S., Jones, C. E., Brekke, C., Holt, B., and Espeseth, M. M. (2016). On the Effect of Imaging Geometry on Multipolarization SAR Features for Oil Spill Observation. *Living Planet Symposium*.

[Solberg et al., 2004] Solberg, A. H. S., Brekke, C., Solberg, R., and Husoy, P. O. (2004). Algorithms for oil spill detection in Radarsat and ENVISAT SAR images. *IEEE Int. Geosci. Remote Sens. Symp. (IGARSS) Proceedings*, 7.

[Song et al., 2017] Song, D., Ding, Y., Li, X., Zhang, B., and Xu, M. (2017). Ocean Oil Spill Classification with RADARSAT-2 SAR Based on an Optimized Wavelet Neural Network.

Remote Sens., 9(8).

[Souyris et al., 2005] Souyris, J.-C., Imboa, P., Fjørtoft, R., Mingot, S., and Lee, J.-S. (2005). Compact Polarimetry Based on Symmetry Properties of Geophysical Media: The $\pi/4$ Mode. *IEEE Trans. Geosci. Remote Sens.*, 43(3):634–646.

[Spearman, 1904] Spearman, C. (1904). The proof and measurement of association between two things. *The American Journal of Psychology*, 100(3/4):441–471.

[Spreen and Kern, 2016] Spreen, G. and Kern, S. (2016). *Front Matter. Chapter 9: Methods of satellite remote sensing of sea ice*, pages 239–260. John Wiley & Sons, Ltd.

[Stark and Woods, 2011] Stark, H. and Woods, J. (2011). *Probability, Statistics, and Random Processes for Engineers (4th Edition)*. Pearson.

[Sun et al., 2018] Sun, S., Hu, C., Garcia-Pineda, O., Kourafalou, V., Hénaff, M. L., and Androulidakis, Y. (2018). Remote sensing assessment of oil spills near a damaged platform in the Gulf of Mexico. *Mar. Pollut. Bull.*, 136:141 – 151.

[Theodoridis and Koutroumbas, 2009] Theodoridis, S. and Koutroumbas, K. (2009). *Pattern Recognition Fourth Edition*. Elsevier.

[Tong et al., 2019] Tong, S., Liu, X., Chen, Q., Zhang, Z., and Xie, G. (2019). Multi-feature based ocean oil spill detection for polarimetric SAR data using random forest and the self-similarity parameter. *Remote Sens.*, 11(4).

[Touzi and Charbonneau, 2014] Touzi, R. and Charbonneau, F. (2014). Requirements on the calibration of Hybrid-Compact SAR. *IEEE Int. Geosci. Remote Sens. Symp. (IGARSS) Proceedings*, pages 1109–1112.

[Touzi et al., 2010] Touzi, R., Vachon, P. W., and Wolfe, J. (2010). Requirement on Antenna Cross-Polarization Isolation for the Operational Use of C-Band SAR Constellations in Maritime Surveillance. *IEEE Geosci. Remote Sens. Lett.*, 7(4):861–865.

[Tucker III et al., 2013] Tucker III, W. B., Perovich, D. K., Gow, A. J., Weeks, W. F., and Drinkwater, M. R. (2013). *Physical Properties of Sea Ice Relevant to Remote Sensing*, chapter 2, pages 9–28. American Geophysical Union (AGU).

[Vachon et al., 2004] Vachon, P. W., Monaldo, F. M., Holt, B., and Lehner, S. (2004). Chapter 5: Ocean surface waves and spectra. *Synthetic Aperture Radar Marine User's Manual (NOAA/NESDIS), C.R. Jackson and J. R. Apel*, pages 139–167.

[Valenzuela, 1978] Valenzuela, G. R. (1978). Theories for the interaction of electromagnetic and oceanic waves - a review. *Boundary-Layer Meteorology*, 13(1-4):61–85.

[van Zyl and Kim, 2010] van Zyl, J. and Kim, Y. (2010). *Synthetic Aperture Radar Polarimetry*. WILEY.

[van Zyl, 1990] van Zyl, J. J. (1990). Calibration of polarimetric radar images using only image parameters and trihedral corner reflector responses. *IEEE Trans. Geosci. Remote Sens.*, 28(3):337–348.

[Vespe and Greidanus, 2012] Vespe, M. and Greidanus, H. (2012). SAR image quality assessment and indicators for vessel and oil spill detection. *IEEE Trans. Geosci. Remote Sens.*, 50(11):4726–4734.

[Wang et al., 2018] Wang, Y., Qi, Q., and Liu, Y. (2018). Unsupervised Segmentation Evaluation Using Area-Weighted Variance and Jeffries-Matusita Distance for Remote Sensing Images. *Remote Sens.*, 10(8).

[Warren et al., 2014] Warren, C. J., MacFadyen, A., and Henry, C. (2014). Mapping Oil for the Destroyed Taylor Energy Site in the Gulf of Mexico. *International Oil Spill Conference Proceedings*, (1).

[Wei et al., 2019] Wei, S., Zhang, H., Wang, C., Wang, Y., and Xu, L. (2019). Multi-temporal SAR data large-scale crop mapping based on U-Net model. *Remote Sens.*, 11(1).

[Winebrenner et al., 1989] Winebrenner, D. P., Tsang, L., Wen, B., and West, R. (1989). Sea-ice Characterization Measurements needed for Testing of Microwave Remote Sensing Models. *IEEE J. Ocean. Eng.*, 14(2):149–158.

[Wismann et al., 1998] Wismann, V., Gade, M., Alpers, W., and Hühnerfuss, H. (1998). Radar signatures of marine mineral oil spills measured by an airborne multi-frequency radar. *Int. J. Remote Sens.*, 19(18):3607–3623.

[WMO-No.574, 2010] WMO-No.574 (2010). Sea-ice Information Services in The World. *Technical Report 574, World Meteorological Organization*.

[Wright, 1968] Wright, J. (1968). A new model for sea clutter. *IEEE Trans. Antennas Propag.*, 16(2):217–223.

[Xi et al., 2016] Xi, Z., Jie, Z., Meijie, L., and Junmin, M. (2016). Assessment of C-band compact polarimetry SAR for sea ice classification. *Acta Oceanol. Sin.*, 35(5):79–88.

[Yin et al., 2015] Yin, J., Yang, J., Zhou, Z., and Song, J. (2015). The Extended Bragg Scattering Model-Based Method for Ship and Oil-Spill Observation Using Compact Polarimetric SAR. *IEEE J. Sel. Topics Appl. Earth Observ. Remote Sens.*, 8(8):3760–3772.

[Zhang et al., 2011] Zhang, B., Perrie, W., Li, X., and Pichel, W. G. (2011). Mapping sea

surface oil slicks using RADARSAT-2 quad-polarization SAR image. *Geophys. Res. Lett.*, 38(10).

[Zhang et al., 2016] Zhang, X., Zhang, J., Liu, M., and Meng, J. (2016). Assessment of C-band compact polarimetry SAR for sea ice classification. *Acta Oceanologica Sinica*, 35(5):79–88.

[Zhang et al., 2017] Zhang, Y., Li, Y., Liang, X. S., and Tsou, J. (2017). Comparison of oil spill classifications using fully and compact polarimetric SAR images. *Applied Sciences*, 7(2).